Chapter 2
Waste Mechanical Energy Harvesting (I): Piezoelectric Effect

2.1 Introduction

Mechanical energy is one of the most ubiquitous energies that can be reused in our surroundings. The sources of mechanical energy can be a vibrating structure, a moving object, and vibration induced by flowing air or water. The energies related to induced vibrations or movement by flow of air and water at large-scale are wind energy and hydroelectric energy, respectively, which are not within the scope of this book. Instead, the mechanical energies here can be classified as so-called "low-level" vibrations and movements. Such potential "low-level" vibrations and movements are summarized in Table 2.1 [1] and Table 2.2 [2].

Mechanical waste energies usually can be harvested by using vibration-to-electricity conversion [2–4]. The most distinguished characteristic of this kind of waste energy harvesting is initially identified for low power generations. Therefore, one of the targeted applications is to power small electronic devices. However, recent development indicates that it can also be used for large-scale applications [5].Vibration-to-electricity conversion can be realized through three basic mechanisms, including electromagnetic [6–8], electrostatic [9], and piezoelectric [10, 11] transductions.

Among the three mechanisms, piezoelectric transduction has received the greatest attention. This is because piezoelectric materials have larger power densities and higher feasibility for practical applications than the materials used in the other two mechanisms [3]. For example, voltage outputs in electromagnetic energy harvesting are typically very low and thus must be amplified to a level sufficiently high to charge storage devices. In contrast, however, piezoelectric energy harvesters output voltages that can be used directly. In electrostatic energy harvesting, the materials should be subject to an external applied voltage to trigger the relative vibratory motion of the capacitor elements, which outputs alternative electrical currents [9]. Such external applied voltages are required in piezoelectric energy harvesting. Another advantage over electromagnetic devices is that piezoelectric harvesting devices can be fabricated at both macro-scale and micro-scale, due to the well-established deposition techniques for thick-films and thin-films piezoelectric

L. B. Kong et al., *Waste Energy Harvesting*, Lecture Notes in Energy 24,
DOI: 10.1007/978-3-642-54634-1_2,

Table 2.1 Sources of mechanical energy around us each and every day that can be harvested for electricity [1]

Human body/motion	Transportation	Infrastructure	Industry	Environment
Breathing, blood flow/pressure, exhalation, walking, arm motion, finger motion, jogging, talking	Aircraft, automobile, train, tires, tracks, peddles, brakes, turbine engine, vibration, noises	Bridges, roads, tunnels, farm, house structure, control-switch, water/gas pipes, AC system	Motors, compressor, chillers, pumps, fans, vibrations, cutting and dicing, noise	Wing, ocean current/ wave, acoustic wave

Table 2.2 Acceleration (m s^{-2}) magnitude and frequency of vibration mode of potential vibration sources

Vibration source	A (m s^{-2})	f_{peak} (Hz)
Car engine compartment	12.0	200
Base of 3-axis machine tool	10.0	70
Blender casing	6.4	121
Clothes dryer	3.5	121
Person nervously tapping their heel	3.0	1
Car instrument panel	3.0	13
Door frame just after door closes	3.0	125
Small microwave oven	2.5	121
HVAC vents in office building	0.2–1.5	60
Windows next to a busy road	0.7	100
CD on notebook computer	0.6	75
Second story floor of busy office	0.2	100

materials [10, 12]. Comparatively, it is hard to fabricate electromagnetic energy harvesters at micro-scale, due to the poor properties of planar magnets and the limited number of turns that can be realized when using planar coils [3].

In this chapter, harvesting mechanical waste energy with piezoelectric effect will be systematically presented. The main content will be started with a detailed description of piezoelectrics, including history of piezoelectric materials, principle of piezoelectric effect, and types and preparation of piezoelectric materials. After that, the progress in the development of mechanical waste energy harvesters based on piezoelectric effect will be summarized. Potential mechanical waste energy sources, including vehicle suspensions, civil structures, rail way tracks, roads, ocean waves, streams, and human motions, have been explored for respective potential applications. The chapter will wound up with some concluding remarks.

2.2 Piezoelectricity and Piezoelectric Materials

2.2.1 Piezoelectricity

The word "piezoelectricity" is derived from the Greek "*piezein*", which means to "squeeze" or "press" [13–16]. There are two piezoelectric effects: direct effect and converse effect. The direct effect (designated as a generator) is identified with the phenomenon whereby electrical charge (polarization) is generated from a mechanical stress, whereas the converse effect (designated as a motor) is associated with the mechanical movement generated by the application of an electrical field. Therefore, piezoelectric energy harvesting is to use the direct effect (generator). Properties of piezoelectric materials are generally characterized by k_p, k_{33}, d_{33}, d_{31}, and g_{33}.

The k factors (e.g., k_{33}, k_{31}, and k_p), which are also called piezoelectric coupling factors, are convenient and direct measurements of the overall strength of the electromechanical effects, i.e., the ability of the ceramic transducer to convert one form of energy to another. They are defined as the square root of the ratio of energy output in electrical form to the total mechanical energy input (direct effect), or the square root of the ratio of the energy available in mechanical form to the total electrical energy input (converse effect). Because the conversion of electrical to mechanical energy (or vice versa) is always incomplete, k is always less than unity. Commonly used as a figure-of-merit for piezoelectrics, the higher k values are most desirable and constantly sought after in new materials. For ceramics, k_p is a typical measure used to compare piezoelectric properties of ferroelectric materials-values ranging from 0.35 for $BaTiO_3$ to as high as 0.72 for PLZT [13].

The d coefficients are called piezoelectric coefficients, having magnitudes of $\times 10^{12}$ C N^{-1} (or pC N^{-1}) for the direct effect and $\times 10^{-12}$ m V^{-1} (or pm V^{-1}) for the converse effect, respectively. Subscript is used to describe the relative direction of inputs and outputs. For example, d_{31} means that this piezoelectric coefficient relates to the generation of polarization (direct effect) in the electrodes perpendicular to the vertical direction (3) and to the stress mechanically applied in the lateral direction (1), while d_{33} indicates the polarization generated in the vertical direction (3) when the stress is applied in the same direction. There are also other similar symbols [13].

g factors are called open-circuit coefficients, another parameters used to evaluate piezoelectric ceramics for their ability to generate large amounts of voltage per unit of input stress. The g constant is related to d constant: $g = d/K\varepsilon_0$ (K is relative dielectric constant and ε_0 is the dielectric constant of free space that equals to unit). High-g-constant piezoelectric ceramics are usually ferroelectrically hard materials whose polarizations are not readily switched and thus they possess lower K values.

Piezoelectricity is usually discussed together with ferroelectricity and pyroelectricity, because they have interesting inter-relationships in terms of crystal structures. All crystals can be categorized into 32 different classes. In the theory of

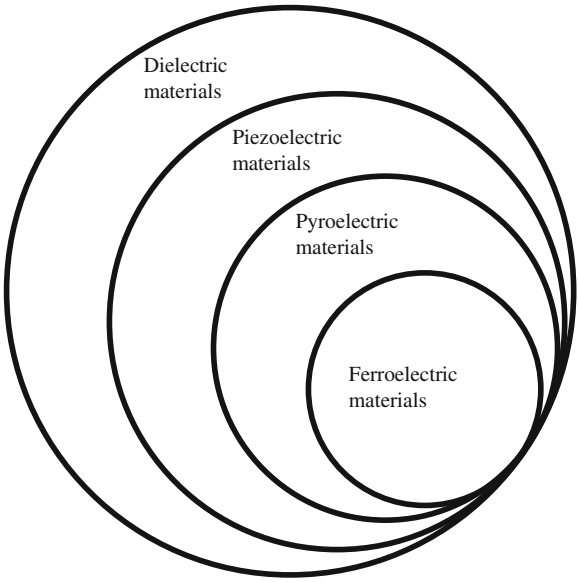

Fig. 2.1 Inter-relationship among piezoelectric, ferroelectric, pyroelectric and dielectric materials. Ferroelectric materials have superior pyroelectric, piezoelectric and dielectric properties than nonferroelectric materials

point groups, these classes are determined by using several symmetry elements: (i) center of symmetry, (ii) axis of rotation, (iii) mirror planes, and (iv) several combinations of them. The 32 point groups are subdivisions of seven basic crystal systems that are, in order of ascending symmetry, triclinic, monoclinic, orthorhombic, tetragonal, rhombohedral (trigonal), hexagonal, and cubic. 21 classes out of the 32 point groups are noncentrosymmetric, which is a necessary condition for piezoelectricity to exist. 20 of them are piezoelectric. Of the 20 piezoelectric crystal classes, 10 crystals are of pyroelectric properties. Within a given temperature range, this group of materials is permanently polarized. Compared to the general piezoelectric polarization produced under stress, the pyroelectric polarization is developed spontaneously and kept as permanent dipoles in the structure. Because this polarization varies with temperature, the response is termed as pyroelectricity. Within the pyroelectric group, there is a subgroup that has spontaneous polarization, which is called ferroelectric materials. On one hand, the polarization in a ferroelectric material is similar to the polarization in a pyroelectric one. On the other hand, there is difference between the two polarizations because the ferroelectric polarization is reversible by an external applied electric field, provided that the applied field is less than the dielectric breakdown of the materials. Therefore, materials that can be defined as ferroelectrics must have two characteristics: the presence of spontaneous polarization and reversibility of the polarization under electric field [13, 14]. Figure 2.1 shows their inter-relationship, together with general dielectrics. This inter-relationship is important because ferroelectric materials have best piezoelectric properties than nonferroelectric materials.

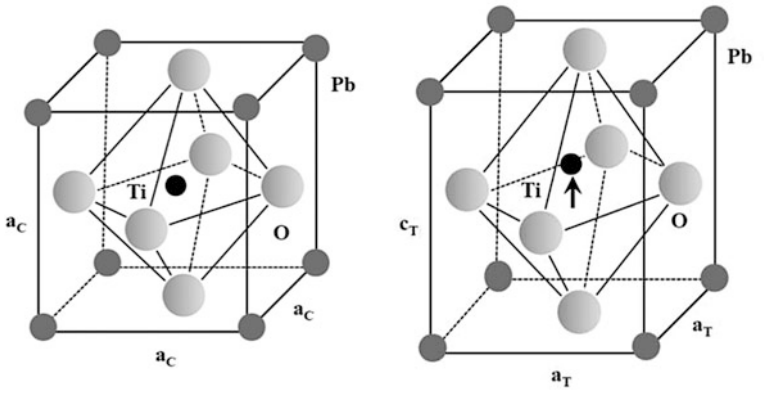

Fig. 2.2 Schematic perovskite structure of $PbTiO_3$, with cubic (*C*) structure in the paraelectric state ($P_s = 0$) and tetragonal (*T*) structure in the ferroelectric state ($P_s \neq 0$)

Ferroelectric materials can be grouped into four subcategories according to their crystal structures: perovskite group, pyrochlore group, tungsten-bronze group, and bismuth layer structure group, among which the perovskite group is the most important and thus the most widely studied. Perovskite is usually expressed as ABO_3. A typical ABO_3 unit-cell structure is shown in Fig. 2.2, taking $PbTiO_3$ as an example [13, 14, 16]. It consists of a corner-linked network of oxygen octahedra, creating an octahedral cage (B-site) and the interstices (A-sites). Ti^{4+} ions occupy the B-site while Pb^{2+} ions occupy the A-site. Figure 2.2 also shows the paraelectric and ferroelectric states of $PbTiO_3$. Most ferroelectric materials undergo a structural phase transition from a high temperature paraelectric phase into a low temperature ferroelectric phase. The paraelectric phase always has a higher symmetry than the ferroelectric phase. The temperature of the phase transition is called as the Curie temperature (T_C). Different ferroelectric materials have different values of T_C, which can be either lower than liquid nitrogen (LN) temperature or higher than 1,000 °C. For a given material (composition), the T_C is closely related to microstructure (grain size and distribution, density, porosity, and pore size and distribution, and impurity, and so on). Generally, the T_C of a given material decreases with decreasing grain size [54].

In the ferroelectric state, the ability of displacement of the central Ti^{4+} ion is the cause for the reversibility of polarization. The switch of many adjacent unit cells is referred to as domain reorientation or switching. The homogeneous areas of the material with the same polarization orientation are referred to as domains, with domain walls existing between areas of unlike polarization orientation [1, 2]. For as-prepared piezoelectric ceramics, the domains are randomly oriented and thus the net polarization of materials is zero because of their cancellation effect. Therefore, the as-prepared piezoelectric ceramics have no piezoelectric effect. To show piezoelectric properties, the newly obtained polycrystalline piezoelectric ceramics must be poled at strong external DC electric fields (10–100 kV cm^{-1}).

Poling is to electrically align the orientation of the randomly distributed domains within the grains and to make ferroelectric ceramics act like a single crystal possessing both ferroelectric and piezoelectric properties. Poling is usually conducted at elevated temperatures, because polarization would be more compliant at high temperatures [13, 14]. After poling during cooling, the applied voltages should be remained until the temperature is sufficiently low.

2.2.2 Brief History of Modern Piezoelectric Ceramics

The history of modern piezoelectricity and piezoelectric ceramics is close related to the history of ferroelectricity and ferroelectric ceramics. The history of ferroelectrics can be tracked back to Rochelle salt (sodium potassium tartrate tetrahydrate, $KNa(C_4H_4O_6)\cdot 4H_2O$), which was synthesized more than 400 years ago, initially for medicinal purposes [13, 14, 16, 17]. It is in this same crystalline material that pyroelectric (thermal-polar), piezoelectric (stress-polar), and ferroelectric were discovered subsequently. Before this discovery, ferroelectricity was only a hypothetical property of solid materials at the turn of the twentieth century. However, the practical application of this material is largely limited due to its water solubility. It was after the discovery of ferroelectric ceramics (barium titanate, $BaTiO_3$), this class of materials became extremely useful for a variety applications.

The first ferroelectric ceramic material is barium titanate ($BaTiO_3$ or BT), which was discovered in the mid-1940s [13, 14, 16, 17]. Before the discovery of $BaTiO_3$, the most widely used materials for capacitors were steatite, mica, TiO_2, $MgTiO_3$, and $CaTiO_3$, with dielectric constant of not higher than 100. During the World War II, there was pressing needs for high dielectric constant materials to fabricate high capacitance capacitors. Before publication was available in the literature, $BaTiO_3$ had already been studied as a high dielectric constant material concurrently. In the later open publications, it was concluded that the source of the high dielectric constant in $BaTiO_3$ is due to its ferroelectric properties [13].

The history of ferroelectric ceramics also includes the report of lead zirconatetitanate ($PbZr_{1-x}Ti_xO_3$, or PZT) piezoelectric ceramics, the development of transparent electro-optical lead lanthanum zirconate titanate ($Pb_{1-x}La_xZr_{1-y}Ti_yO_3$, or PLZT), the research on lead magnesium niobate ($PbMg_{1/3}Nb_{2/3}O_3$, or PMN) relaxor ferroelectric ceramics and the discovery of many other nonperovskite ferroelectric ceramics [13, 16]. Among these, PZT has been demonstrated to possess best performances as piezoelectric ceramics.

Recently, there has been a concern with PZT, due to the toxicity of Pb. Regulations and legislations have been established globally to restrict the use of lead-containing materials. For example, according to the directive for the Restriction of the use of certain Hazardous Substances in electrical and electronic equipment (RoHS) adopted by the European Parliament in the year 2006, the maximum allowed concentration of lead is established to be 0.1 wt% in homogeneous

materials for electrical and electronic equipment used in households as well as industry. Therefore, lead-containing piezoeletric materials will be prohibited eventually. Similar regulations have been established worldwide. As a consequence, there is significantly increasing interest in developing lead-free piezoelectric ceramics all around the world. Although major progress has been made in materials research [18, 19], there are still obstacles blocking the successful industrial implementation of lead-free piezoelectric ceramics. One key problem is their poor piezoelectric properties and fatigue degradation problem. Therefore, PZT will still be dominant materials for piezoelectric applications at least in the near future.

2.2.3 Microstructures of Piezoelectric Ceramics

Fully dense piezoelectric ceramics (>95 % of theoretical density) are required by most applications for several reasons. Firstly, a full densification ensures the ceramics to have their maximum performance. For example, the piezoelectric constant of piezoceramics usually decreases with decreasing density. This is because the pores or vacuum have no piezoelectric effect. Secondly, the presence of pores is generally a cause of high loss tangent, since porosity could provide a conduction path for electricity and thus could be a main contribution to dielectric loss tangent, as conduction loss. In this case, external electric fields cannot be applied to the materials effectively. Moreover, electrical conduction caused by porosity is also responsible for degraded electrical breakdown strength. Finally, mechanical strength, sometimes a critical requirement for some specific applications, especially as actuators, is directly related to density of the materials used.

Generally, the densities of piezoelectric ceramics increase with increasing sintering temperature. However, very high temperature is not suitable for lead- and bismuth-containing piezoelectric materials, which is due to the volatility characteristic of lead and bismuth. High temperature sintering also leads to abnormal grain growth (secondary grain growth). The presence of exaggeratedly grown grains is harmful to the performance for most piezoelectric ceramics. To effectively enhance the densification of piezoelectric ceramics at relatively low temperatures, various attempts have been made and have been widely reported in the literature. The main strategies that have been employed to reduce the sintering temperature of piezoelectric ceramics are the use of fine/ultrafine powders and the addition of sintering aids. If sintering aids are used, they must have relatively low melting points and no reaction with the piezoelectric phases during sintering process. Grain size is another important factor that determines piezoelectric properties of piezoceramics [20, 21]. The variation in grain size with sintering temperature is similar to that of density, i.e., grain size increases with increasing sintering temperature. There is a critical grain size for most piezoelectric ceramics. These properties can be optimized by adjusting materials processing parameters.

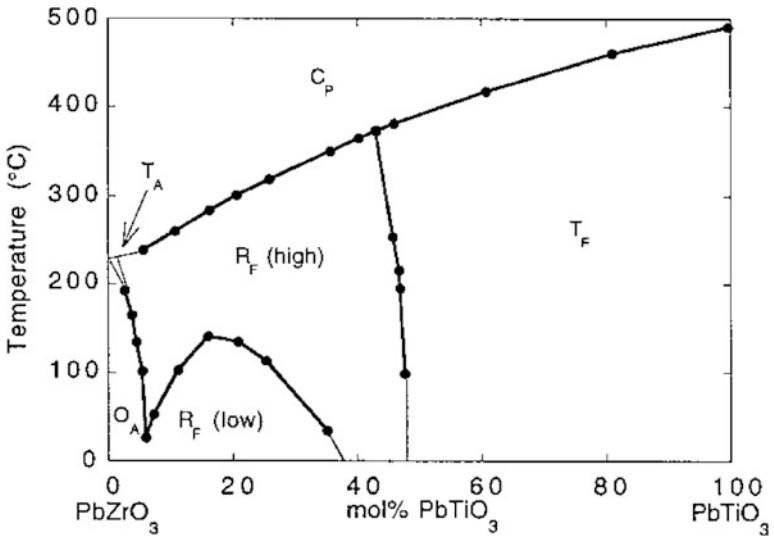

Fig. 2.3 Phase diagram of $PbZr_{1-x}Ti_xO_3$ [23]. There is a morphotropic phase boundary (MPB) at $x = 0.52$–0.53, with highest electrical properties

2.2.4 Typical Piezoceramics

As mentioned above, lead zirconate titanate ($Pb(Zr_xTi_{1-x})O_3$ or PZT, $x = 0$–1) is the most widely used to fabricate piezoelectric ceramics. PZT is a solid solution of $PbTiO_3$ (PT) and $PbZrO_3$ (PZ). PT and PZ can form solid solution over composition range. Figure 2.3 shows a phase diagram of PZT. There exists an almost temperature-independent phase boundary at $x = 0.52$–0.53, which separates a rhombohedral Zr-rich phase from a tetragonal Ti-rich phase. Dielectric constant, piezoelectric constant, and electromechanical coupling coefficient all exhibit a pronounced maximum value for the composition corresponding to this phase boundary, which is generally referred to as the morphotropic phase boundary (MPB) [22, 23]. This is mainly attributed to the existence of a mixture of phases at the boundary and the presence of a larger number of reorientable polarization directions existing in the MPB mixed-phase region. This is reason why PZT is usually meant to be $PbZr_{0.52}Ti_{0.48}O_3$ or $PbZr_{0.53}Ti_{0.47}O_3$ used as piezoceramics in the open literature.

2.2.5 PZT Ceramics

Conventionally, PZT powder is synthesized by using solid-state reaction method, with PbO (Pb_3O_4), ZrO_2, and TiO_2 oxide powders as starting materials. Mixtures of the three oxide powders with nominated compositions of PZT are ball milled

and then calcined at a suitable temperature to form the desired perovskite phase. PZT piezoelectric ceramics are obtained by sintering the calcined powders at higher temperatures to achieve full densification.

Based on this basic composition, a large number of modifications have been adapted to cater for the requirements of different applications. According to international convention, piezoceramics are divided into two groups: soft and hard PZT ceramics. Soft and hard PZT ceramics refer to their mobility of the dipoles or domains and hence also to the polarization and depolarization behavior. Soft piezoceramics have high domain mobility and thus are easy to be poled. They usually have large piezoelectric charge coefficient, moderate values of permittivity, and high coupling factors. Hard PZT materials can be subjected to high electrical and mechanical stresses. Their properties change only little under these conditions, which makes them more suitable for high-power applications. They possess large piezoelectric coupling factors, high qualities, and very good stability at high mechanical loads and operating fields.

Commercially available oxide powders have relatively large grain/particle sizes. The synthesis of PZT with these powders requiring a high calcination temperature form the perovskite phase [24]. Figure 2.4 shows representative microstructural properties of a set of PZT ceramics synthesized by using the conventional solid-state reaction method [24]. PZT powders thus have rough particles that lead to high sintering temperature, which is not favorite owing to the volatility of Pb. Therefore, special carefulness should be taken when sintering these rough PZT powders to avoid the loss of Pb during the sintering process. One of the ways to address this problem is the use of fine PZT powders, which can be synthesized by using wet-chemical synthesis methods, such as chemical co-precipitation [25] and sol-gel [26]. Due to the high chemical homogeneity provided by these wet-chemical processing routes, PZT powders have ultrafine or nanosized grain/particles and thus can be sintered at significantly low temperatures. However, these chemical methods are relatively less cost-effective, because they require the use expensive starting chemicals and they also involve a multistep processing.

More recently, a novel technique, mechanochemical synthesis with high-energy ball milling, was employed to synthesize PZT powders [16]. In this method, the formation of designed compounds is due to the reactions of oxide precursors which are activated by mechanical energy, instead of the heat energy required in the conventional solid-state reaction process. The mechanical technique is superior to both the conventional solid-state reaction and the wet-chemistry-based processing routes for several reasons. Firstly, it uses cost-effective and widely available oxides as the starting materials. Secondly, it skips the intermediate temperature calcination step, leading to a simpler process. Thirdly, it takes place at room temperature in closely sealed containers, thus effectively alleviating the loss of Pb. Furthermore, due to their nanometer scale size and very high homogeneity, the mechanochemically derived PZT powders demonstrate much better sintering behavior than those synthesized by the conventional solid-state reaction and wet-chemical processes.

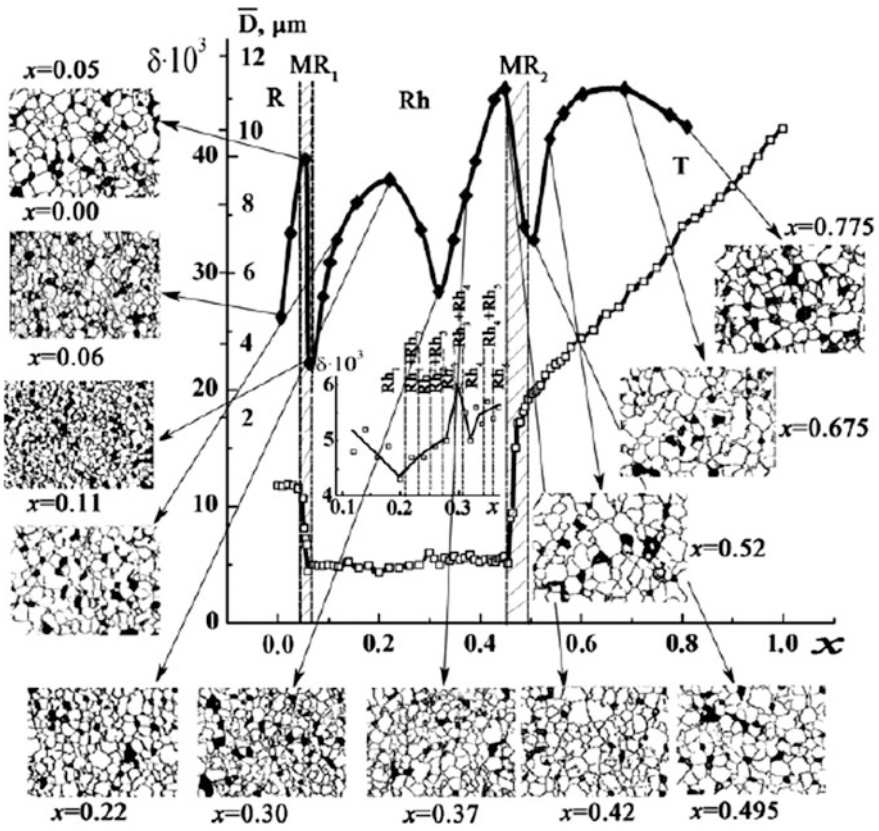

Fig. 2.4 Variation in mean grain size, D, and homogeneous deformation parameter, d, as a function of the content of $PbTiO_3$ in the PZT system. The symmetries are designated as *R* rhombic, *Rh* rhombohedral, *T* tetragonal, and *MR1* and *MR2* denote morphotropic regions. Reproduced with permission from [24]. Copyright @ 2013, Elsevier

As an example, Fig. 2.5 shows XRD patterns of the mixtures (PbO, ZrO_2, and TiO_2) for the composition of $PbZr_{0.52}Ti_{0.48}O_3$, milled for different time durations, using a Fritsch Pulverisette five planetary high-energy ball milling system, with tungsten carbide (WC) vials and balls as the milling media [27]. After milling for 4 h, no PZT is formed, but the diffraction peaks from PbO are greatly broadened and weakened, indicating that the starting oxides have been significantly refined as a result of the high-energy ball milling. The diffraction peaks of PbO are further widened and reduced in the 8-h milled sample. At the same time, a trace of PZT can be observed. PZT with perovskite structure comes to the predominant phase in the samples milled for 15 and 24 h. It is worth mentioning that all the fours samples can be used to make PZT ceramics, which means that complete reaction of the precursor oxides is not necessary. This is because the reaction can be completed during the sintering processing. In this case, the milling time can be significantly reduced to save energy and time.

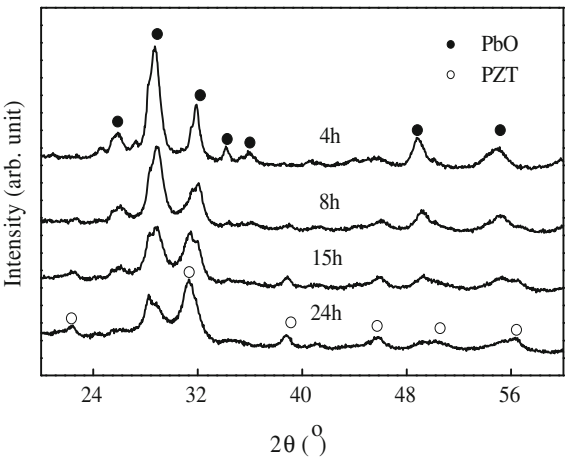

Fig. 2.5 XRD patterns of the mixtures for $PbZr_{0.52}Ti_{0.48}O_3$ milled for different times, using a planetary high-energy ball mill and tungsten carbide (WC) media. Reproduced with permission from [27]. Copyright @ 2001, Materials Research Society

2.2.6 PZT Films

For applications in microelectromechanical system (MEMS), PZT thin films or thick films should be used [28]. Although there is no restricted definition, thin films usually have thicknesses of <1 μm and thick films are those with thickness of >1 μm. In practice, the thickness of a thick film can be up to hundreds of μm. PZT films can be deposited by using physical or chemical methods. Physical deposition includes sputtering, physical vapor deposition (PVD), and pulsed laser deposition (PLD), while chemical method includes solution, sol-gel, hydrothermal, and chemical vapor deposition (CVD). Among these physical and chemical methods, sol-gel has been most widely used to deposit PZT films, due to its effectiveness and efficiency.

Figure 2.6 shows a flow chart for deposition of PZT films by using a sol-gel technique [29]. $Pb(CH_3COO)_2{\cdot}5H_2O$ is dissolved in CH_3COOH at 120 °C, while $Zr[CH_3(CH_2)_2CO]_4$ and $Ti[(CH_2)_2CHO]_4$ are stabilized with acetylaceton. They are then mixed to form 5 M solution with a composition of PZT, which is used to deposit PZT films by using spin-coating. After every coating, the samples are pyrolyzed at 350 °C for 10 min, followed by annealing at 650 °C for 30 min. A final annealing at 700 °C for 30 min is conducted. PZT films with desired thickness can be obtained by repeating the pyrolysis-annealing step.

Figure 2.7 shows XRD patterns of the PZT films deposited for 1–6 times [29]. Pervoskite phase has been well formed in all films, which means that the annealing temperature of 700 °C is sufficient. There is no pyrochlore phase in all samples. The sample coated for just one time has a random orientation. However, with increasing thickness, it becomes (100) orientated gradually. Cross-sectional SEM images of selected films are shown in Fig. 2.8 [29]. The thickness of the sample deposited for one time is ~0.5 μm. The total thickness of the films increases almost linearly with the number of deposition layers, which provides a very

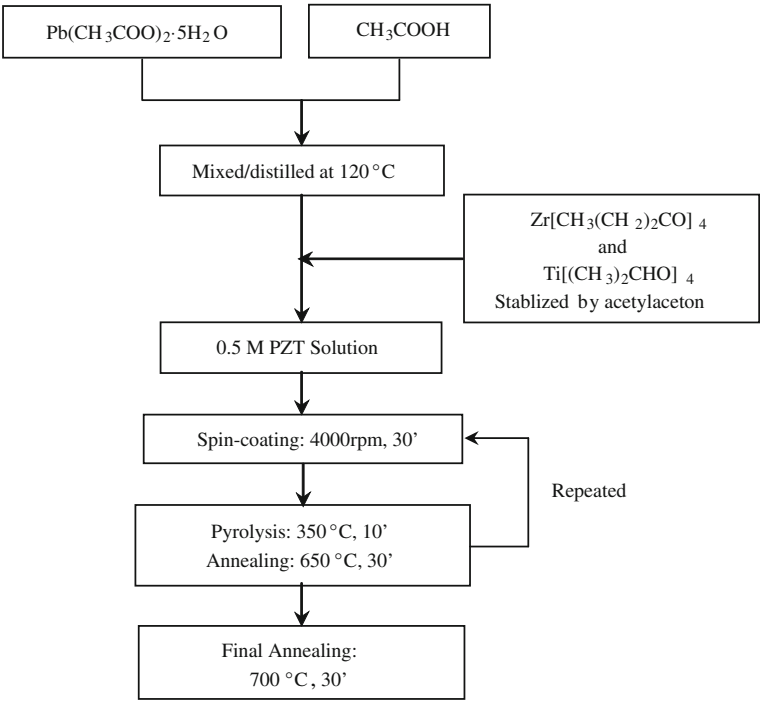

Fig. 2.6 Flow chart for deposition of PZT films with a modified sol-gel technique to produce single layer of PZT with sufficient thickness for thick film fabrication [29]

effective way to deposit thick PZT films. Comparatively, a single layer of PZT film deposited by using normal sol-gel process is much less than 0.1 μm. The use of acetic acid is the key to deposit thicker single layer of Pb containing films [30–32]. By the way, the films have a columnar microstructure, indicating their good crystallinity. Nevertheless, deposition of PZT thick films is still a challenge.

Figure 2.9 shows surface SEM images of selected PZT films [29]. All films have dense and crack-free microstructure. The average grain size slightly increases with increasing thickness, which can be readily attributed to increasing number of annealing times.

More recently, a new approach, called nanocomposite processing route, has been proposed to incorporated high-energy ball milling technique with sol-gel process to deposit thick films, which cannot be realized using the typical sol-gel with solution precursors [33–37]. This approach has combined the advantages of both high-energy milling and the sol-gel process. In this processing, commercial PZT powder is milled using a high-energy mill to produce nano-sized PZT powder. The nano-sized PZT powder is then milled for one more time with appropriate dispersants, which are used to modify its surficial characteristics. The modified PZT nano-sized powder can be readily mixed with sol-gel solutions

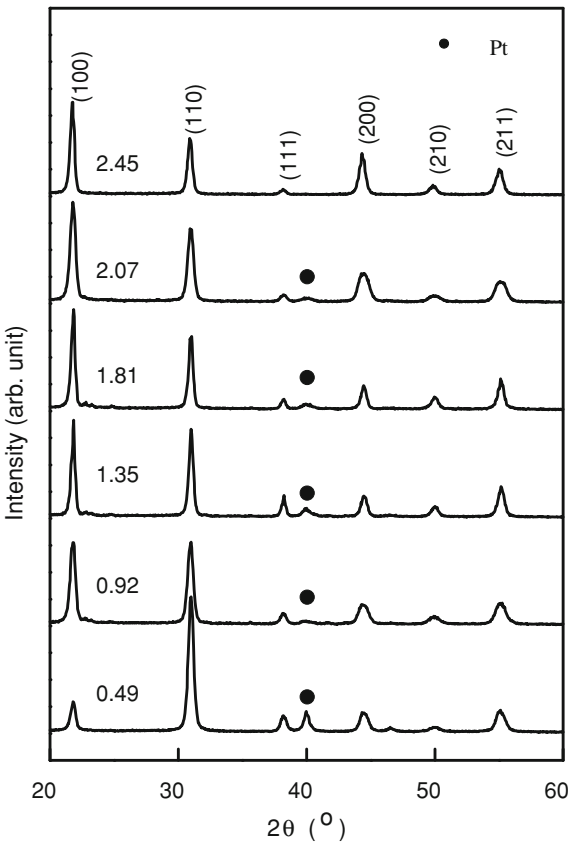

Fig. 2.7 XRD patterns of the PZT films deposited for 1–6 times (layers) with film thickness indicated [29]. There is a gradual increase in (100) orientation

without the presence of agglomerations or precipitations. This kind of mixture can be used as same as the normal sol-gel solutions to deposit thick films on various substrates. The slurries may also directly be used to other processing, such as tape casing, screen printing, and molding [34] (Fig. 2.10).

Thick films with thickness of up to 25 μm have been prepared through multi-layer deposition with one layer being ~2 μm, which is nearly 50–100 times the normal sol-gel solution process. Figure 2.11 shows an example of such thick films [35]. The film is very uniform in thickness, with a dense microstructure and narrow distribution of grain sizes (~100 nm). Compared with the thick films prepared by using a precursor made of micro-sized PZT powder, the nanocomposite film has electrical properties, which has been attributed to the factor that the latter has a dense microstructure than the former. Such kind of composite thick films have been successfully combined with silicon technology to fabricate MEMS piezoelectric devices, so that they are suitable for applications in mechanical energy harvesting devices.

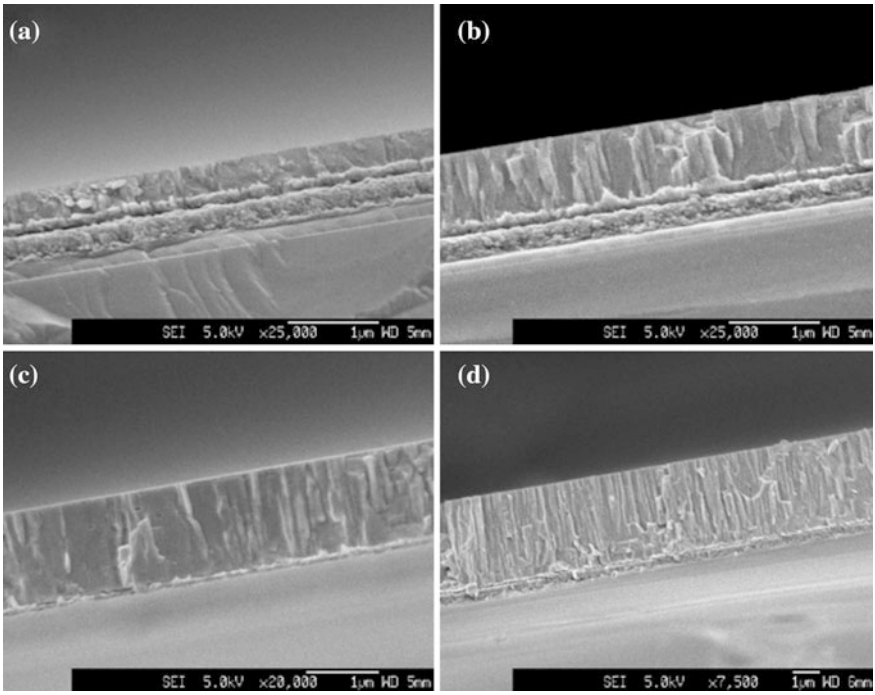

Fig. 2.8 Cross-sectional SEM images of the PZT films deposited for different times (layers): **a** 1, **b** 2, **c** 3, and **d** 6 [29]. All the films have a columnar structure

PZT ceramics have been prepared from the nanocomposite precursors at much lower temperature than that required by the conventional ceramic process [34]. Fully dense PZT ceramics can be achieved after sintering at a temperature as low as 800 °C. Interestingly, no obvious grain growth is observed in the samples sintered at temperatures from 850 to 1,000 °C, which means that the grain growth is stopped at $\sim$850 °C. The absence of grain growth at high temperatures has been attributed to the uniform size distribution and nonagglomeration of the nanocomposite precursors. This feature is particularly of importance when this kind of precursor is used to fabricate multilayer structured devices in which small thickness of single layer is required.

2.2.7 Piezoelectric Polymers

Polyvinylidene fluoride or polyvinylidene difluoride (PVDF) has been found to show piezoelectric (ferroelectric) effect, due to the presence of a non-centrosymmetric unit cell and a net polarization in the material [38–40]. The common characteristics of piezoelectric polymeric materials are: a large dipole moment in

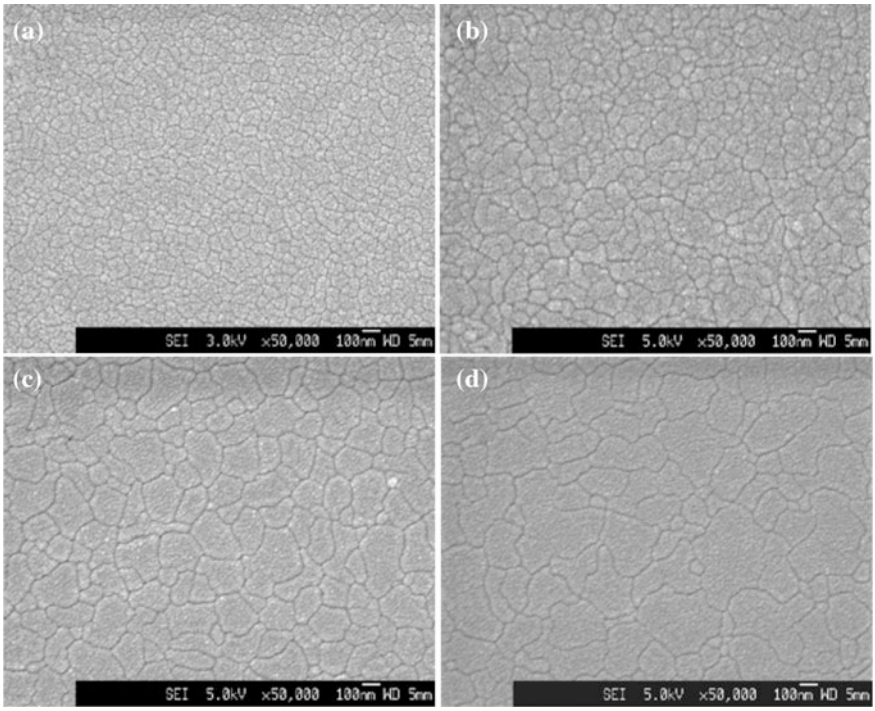

Fig. 2.9 Surface SEM images of the PZT films deposited for different times (layers): **a** 1, **b** 2, **c** 3 and **d** 5 [29]. Grain size of the films gradually increases with increasing thickness

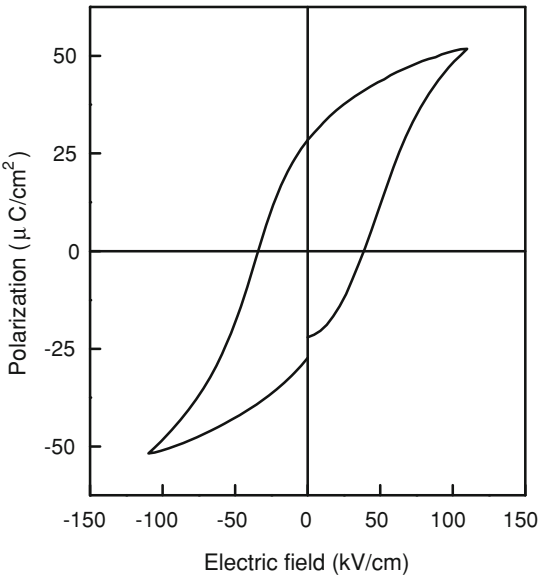

Fig. 2.10 Representative polarization-field (P-E) hysteresis curve of the PZT films showing their high quality [29]

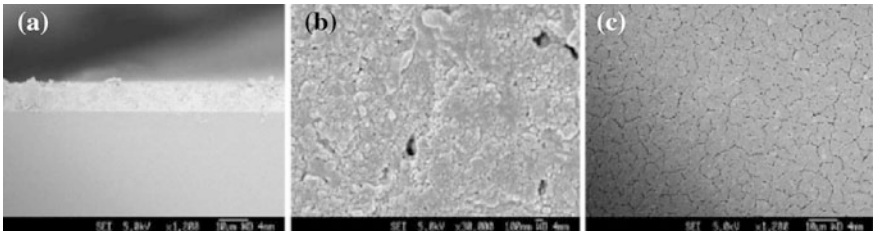

Fig. 2.11 SEM images of the thick film prepared with nanocomposite precursors: **a** and **b** cross-section and **c** surface. Reproduced with permission from [35]. Copyright @ 2003 Elsevier

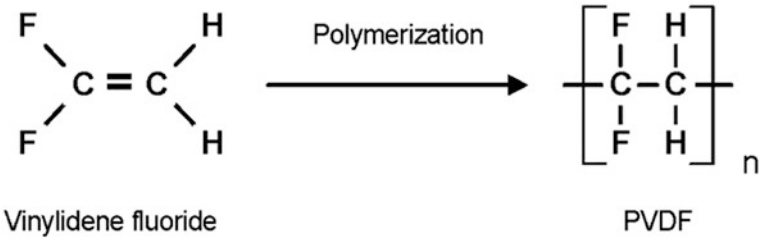

Fig. 2.12 Polymerization of vinylidene fluoride to form PVDF

the repeating unit, feasibility of crystallization in a noncentrosymmetric unit cell, and alignment of molecular dipoles. A dipole moment arises from a charge separation between adjacent atoms. In polymers, this can occur between covalently bonded atoms along the polymer chain or between adjacent chains.

PVDF has chains of CH_2CF_2 and is a semi crystalline polymer. Figure 2.12 shows the formation of PVDF polymer through the polymerization of monomer vinylidene fluoride. The hydrogen atoms having net positive charge and the fluorine atoms with net negative charge end up on opposite sides, as shown in Fig. 2.13. This develops a pole direction (indicated by the small ***p*** in Fig. 2.13). If the external applied electric field is in the opposite direction of the poled direction of the PVDF sheet, it will be stretched in the length direction. If the electric field is in the direction of the poled direction of the PVDF sheet, there will be a contraction in the length direction of the sheet. These two responses are shown in Figs. 2.14 and 2.15, respectively, which is the mechanism of piezoelectric effect of PVDF.

It was later found that copolymers of PVDF with trifluoroethylene (TrFE) are new polymer materials with stronger piezoelectric effect. The copolymers have advantages over pure PVDF. The P(VDF-co-TrFE) copolymers can be modified by adjusting the compositions of the two components. The random copolymers P(VDF-co-TrFE)s are usually synthesized by copolymerization of VDF and TrFE monomers.

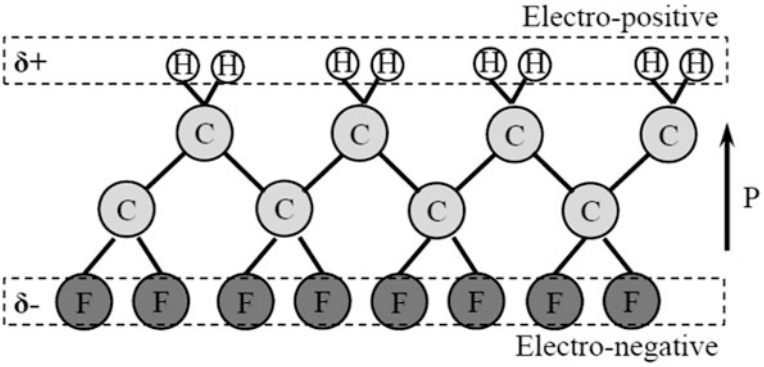

Fig. 2.13 Schematic diagram of atom arrangement in PVDF molecule

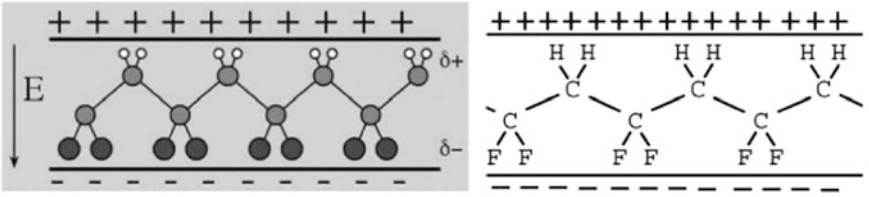

Fig. 2.14 Stretch in length direction occurred if the applied electric field is in the opposite direction of the poled direction of the PVDF sheet

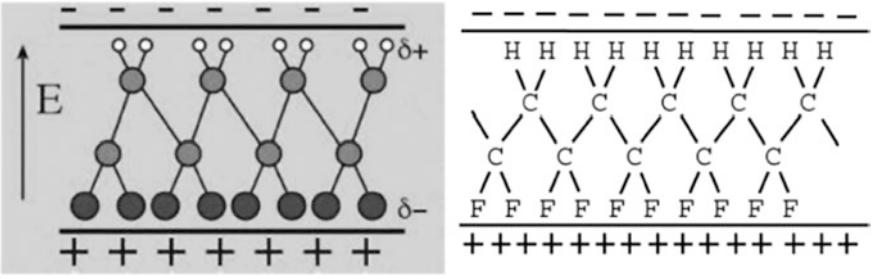

Fig. 2.15 Contraction in length direction occurred if the electric field is in the direction of the poled direction of the PVDF sheet

2.2.8 Composites

Piezoelectric ceramics have high piezoelectric performances, but are hard and rigid for some applications that require flexibility and complicated shapes. To address this problem, composite materials are proposed, which consist of

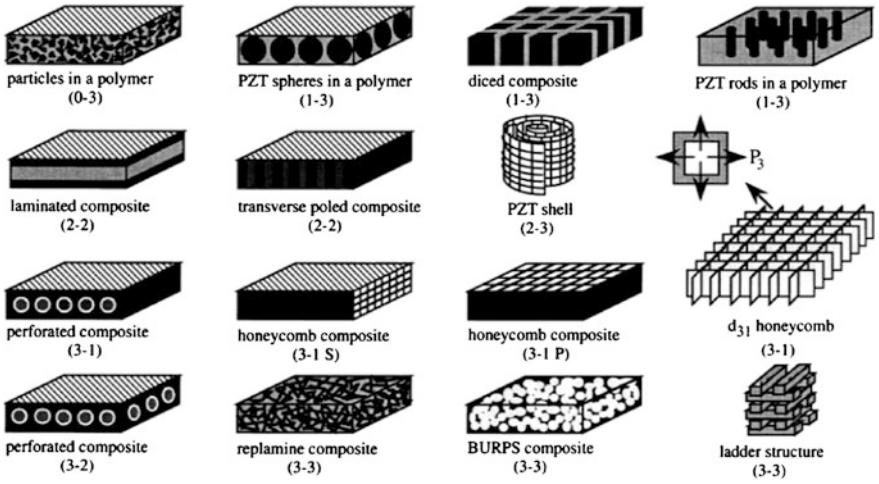

Fig. 2.16 Connectivity of constituent phases in piezoelectric ceramic-polymer composites. Reproduced with permission from [41]. Copyright @ 1999, Elsevier

piezoelectric ceramic particles and polymer matrix. The presence of polymer matrix makes the composites to have mechanical flexibility. Composites are usually described by using a notation-connectivity. Figure 2.16 shows schematics of possible connectivity of composites with PZT and a polymer [41]. 0, 1, 2, and 3 are used to represent spherical particles, 1D wires, rods or fibers, 2D sheets and 3D matrix, respectively. To date, eight types of two-phase piezoelectric composites (piezocomposites) have been studied: 0–3, 1–3, 2–2, 2–3, 3–0, 3–1, 3–2, and 3–3. In these piezocomposites, the first number in the notation denotes the physical connectivity of the active phase (PZT) and the second number refers to the physical connectivity of the passive phase (polymer). There have been increasing reports on piezocomposites based on PZT and PVDF [42].

2.3 Principle of Piezoelectric Effect for Energy Harvesting

2.3.1 General Theory of Mechanical Energy Conversion

Harvesting of mechanical energy is to convert it into electrical energy, which requires a mechanical system that couples motion or vibration to a transduction mechanism. The mechanical system should be designed to be able to maximize the coupling between the mechanical energy sources and the transduction mechanism, depending on the characteristics of the environmental motions. For example, energy due to vibration can be converted by using inertial generators, with the mechanical component attached to an inertial frame that acts as a fixed reference.

The inertial frame transmits the vibrations to a suspended inertial mass to produce a relative displacement between them. System like this usually has a resonant frequency, which can be designed to match the characteristic frequency of the environmental motions. Detailed analysis on mechanisms of mechanical energy harvesting can be found in Refs. [43, 44]. A brief description is presented as follows.

These inertial-based generators can be well described as second-order spring-mass systems. For a system with a seismic mass of m on a spring with a stiffness of k, its energy loss, consisting of parasitic loss, c_p and electric energy generated by the transduction mechanism, c_e, can be represented by damping coefficient, c_T. The system is excited by an external sinusoidal vibration, $y(t) = Y\sin(\omega t)$. At resonant frequency, there is a net displacement, $z(t)$, between the mass and the frame. If the mass of the vibration source is greatly larger than that of the seismic mass, the latter can be ignored. If the external excitation is harmonic, the differential equation of the motion is given by:

$$m\ddot{z}(t) + c\ddot{z}(t) + kz(t) = -m\ddot{y}(t). \tag{2.1}$$

Standard solution for the mass displacement will be:

$$z(t) = \frac{\omega^2}{\sqrt{\left(\frac{k}{m} - \omega^2\right)^2 + \left(\frac{c_T\omega}{m}\right)^2}} y \ \sin(\omega t - \phi), \tag{2.2}$$

where ϕ is phase angle, given by:

$$\phi = \tan^{-1}\left(\frac{c_T\omega}{k - \omega^2 m}\right). \tag{2.3}$$

Energy conversion can be maximized when the excitation frequency matches the natural frequency of the system, ω_n, given by:

$$\omega_n = \sqrt{k/m}. \tag{2.4}$$

The powder dissipated with the system is:

$$P_d = \frac{m\zeta_T Y^2 \left(\frac{\omega}{\omega_n}\right)^3 \omega^3}{\left[1 - \left(\frac{\omega}{\omega_n}\right)^2\right]^2 + \left[2\zeta_T\left(\frac{\omega}{\omega_n}\right)\right]^2}, \tag{2.5}$$

where ς_T is the total damping ration, which is $\varsigma_T = c_T/2m\omega_n$. Maximum powder is achieved when the system is operated at ω_n, while P_d can be expressed as:

$$P_d = \frac{mY^2\omega_n^3}{4\zeta_T}, \tag{2.6}$$

$$P_d = \frac{mA^2}{4\omega_n\zeta_T}, \tag{2.7}$$

where A is the excitation acceleration level, with $A = \omega_n^2 Y$. Noting that these are steady-state solutions, powder will not tend to be infinity when the damping ratio approaches zero. The maximum powder generation can be evaluated by considering the parasitic and system damping ratio, which is given by:

$$P_e = \frac{m\zeta_e A^2}{4\omega_n(\zeta_p + \zeta_e)^2}, \tag{2.8}$$

P_e is maximized at $\varsigma_p = \varsigma_e$. When there is sufficient acceleration, increased damping effects will lead to a response with broadened bandwidth, so that the generator will be less sensitive to frequency. An excessive device amplitude can lead to nonlinear behavior of the generator, which will make it difficult in keeping the generator working at resonance frequency. For specific applications, both the frequency of the generator and the level of damping should be specifically designed to maximize the power output. The power generation can also be maximized by maximizing the mass of the mechanical structure.

The piezoelectric damping coefficient can be estimated by using the following equation:

$$c_e = \frac{2m\omega_n^2 k^2}{2\sqrt{\omega_n^2 + (1/(R_{\text{load}}C_{\text{load}})^2)}}. \tag{2.9}$$

where k is the piezoelectric coupling factor of the materials, while R_{load} and C_{load} are load resistance and capacitance. At maximum powder generation, there is optimal load, given by:

$$R_{\text{opt}} = \frac{1}{\omega_n C}\frac{2m\omega_n^2 k^2}{\sqrt{4\zeta_p^2 + k^4}}. \tag{2.10}$$

Specifically, for piezoelectric materials, the mechanical and electrical behaviors can be described by using the following linear constitutive equations:

$$S_{ij} = s_{ijkl}^E T_{kl} + d_{kij} E_k, \tag{2.11}$$

$$D_i = d_{ikl}^E T_{kl} + \varepsilon_{ik}^T E_k. \tag{2.12}$$

The subscripts i, j, k and l can be values of 1, 2, and 3. S and T are strain and stress tensors, respectively. The stresses, represented by T with a unit of N m^{-2}, are induced by the mechanical and electrical effects. D and E are the electric displacement and electric field vectors, with a unit of C m^{-2} and V m^{-1}, respectively. Also, s^E is the elastic compliance matrix evaluated at a constant electric field with a unit of m^2 N^{-1}, d is a matrix of piezoelectric strain coefficients with a unit of m V^{-1} and ε^T is a matrix of permittivity values that are evaluated at a constant stress with a unit of N V^{-2}. In Eqs. (2.11) and (2.12), d represents the charge created by an external force in the absence of an electric field (short circuit

electrical condition) or the displacement caused by an applied voltage in the absence of an applied force (stress free mechanical condition).

For piezoelectric composite materials, effective electromechanical coupling factor is used, which is given by:

$$k_{\text{eff}} = \sqrt{1 - \left(\frac{F_r}{F_a}\right)^2} \tag{2.13}$$

where F_r is the resonance frequency (Hz) and F_a is the antiresonace frequency (Hz) of a piezoelectric cantilever beam. The voltage coefficient, g (V m N^{-1}) is given by [45]:

$$g = {}^{d}/_{\varepsilon_T}. \tag{2.14}$$

Mechanical quality factor, Q_M, is defined as [45]:

$$Q_M = 2\pi \frac{\text{energy stored/cycle}}{\text{energy dissipated/cycle}}. \tag{2.15}$$

The amount of energy stored in a piezoelectric device, E_C is given by:

$$E_C = \frac{1}{2}CV^2, \tag{2.16}$$

where C is capacitance of the piezoelectric element and V is the voltage produced.

The maximum efficiency of the piezoelectric devices can also be estimated by the following equation:

$$\eta = \frac{\frac{1}{2}\left(\frac{k^2}{1-k^2}\right)}{\frac{1}{Q_M} + \frac{1}{2}\left(\frac{k^2}{1-k^2}\right)}. \tag{2.17}$$

This equation indicates that the efficiency can be increased by increasing k and Q_M, which are properties of the piezoelectric materials. Therefore, selection of materials is a very important step toward energy harvesters with high efficiencies. This is also the reason why PZT has been the most promising piezoelectric materials for mechanical energy harvesting applications.

2.3.2 Piezoelectric Energy Harvesting Devices

Piezoelectric materials can produce electrical charges when they are subject to external mechanical loads. Figure 2.17 shows working principle of a piece of piezoelectric material. The magnitude and direction of the electrical current are determined by the magnitude and direction of the external mechanical stress/strain applied to the materials. There have been various modes of vibration that can be used to construct piezoelectric harvesting devices. The common modes of vibration are summarized in Fig. 2.18 [43]. With given modes of vibration, there are

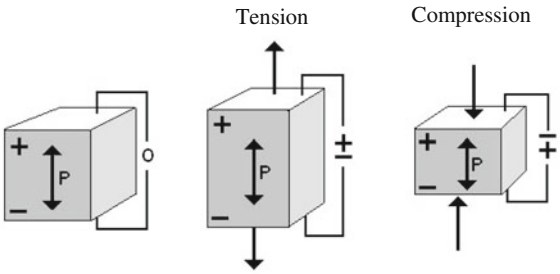

Fig. 2.17 Schematic showing the response of a piece of piezoelectric ceramics to external mechanical stimulation

different piezoelectric structures. Figure 2.19 shows typical piezoelectric structures that can be found in open literature [43].

Among the various piezoelectric structures for energy harvesters, the cantilevered beams with one or two piezoelectric ceramic thin sheets, which are named unimorph and bimorph (Fig. 2.19a), respectively, are the simplest ones. As discussed above, the harvester beam is positioned onto a vibrating host, where the dynamic strain induced in the piezoceramic layer(s) results in an alternating voltage output across their electrodes. Figure 2.20 shows a schematic of a cantilever tested under base excitation [46]. When a harmonic base motion is applied to the structure, an alternating voltage output is produced.

Cantilevered piezoelectric energy harvesters can work in two modes: d_{33} mode and d_{31} mode, as shown in Fig. 2.21 [47]. In d_{31} mode, a lateral force is applied in the direction perpendicular to the polarization direction. In this case, the bending beam has electrodes on its top and bottom surfaces, as in Fig. 2.21a. In d_{33} mode, forces are applied in the same direction as the polarization direction, where the bending beam has all electrodes on its top surface, as in Fig. 2.21b. Although piezoelectric materials working in d_{31} mode normally have lower coupling coefficients than in d_{33} mode, d_{31} mode is more commonly used. This is because when a single-layer cantilever or a double-clamped beam bends, more lateral stress is produced than vertical stress, which makes it easier to couple in d_{31} mode [47]. Similar principle can be applied to the harvesters with other structures.

Beam structures are usually used for low stress levels, whereas at high stress levels, another type of device, ceramic–metal composites, is preferred. Ceramic–metal composites generally have a simple design with a metal faceplate, called shell or cap, which couples to both the ceramic and the surrounding medium. The metal component transfers the incident stress to the ceramic or the displacement to the medium. Flextensional transducers are good examples of ceramic–metal composites. In flextensional transducers, the flexural vibration of the metal shell causes an extensional (or contractional) vibration of the piezoelectric element. The miniaturized versions of flextensionals, the moonie (Fig. 2.19c), and cymbal (Fig. 2.19e) transducers possess 2-(0)-2 connectivity. These transducers, shown in Fig. 2.20, consist of a poled piezoelectric disk (fully electroded on both faces) which is sandwiched between two metal endcaps, each containing a shallow

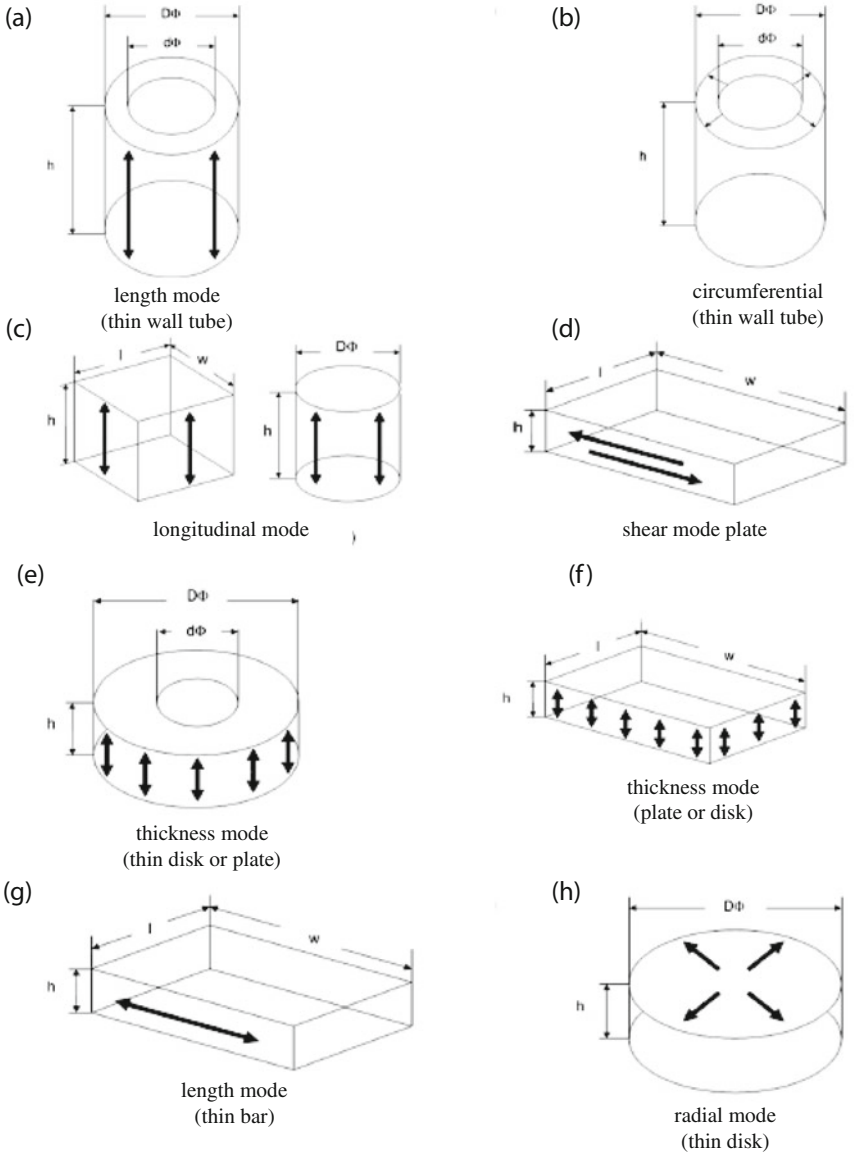

Fig. 2.18 Common modes of vibration. Reproduced with permission from [43]. Copyright @ 2008, IoP Publishing

air-filled cavity on their inner surface [41, 43]. In the case of the moonie, the cavities are in the shape of a half moon, whereas the cymbal has a truncated cone-shaped cavity. The presence of these cavities allows the metal caps to serve as mechanical transformers for transforming and amplifying a portion of the incident

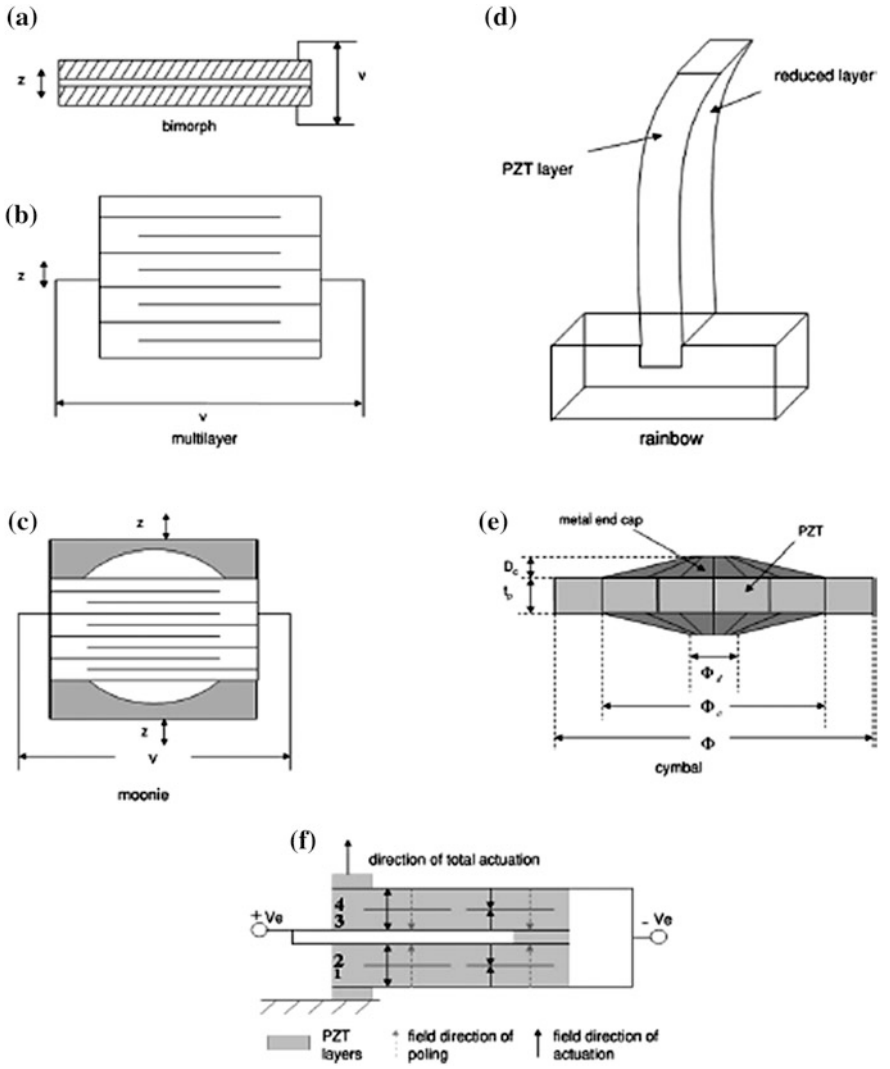

Fig. 2.19 Piezoelectric structures: **a** bimorph, **b** multilayer, **c** Moonie, **d** RAINBOW, **e** cymbal and **f** S-morph. Reproduced with permission from [43]. Copyright @ 2008, IoP Publishing

axial-direction stress into tangential and radial stresses of opposite sign. Thus, the d_{33} and d_{31} contributions of the PZT now add together (rather than subtracting) in the effective d_h of the device.

To theoretically study the mechanics of piezoelectric energy harvesting and experimentally evaluate the performances of alternative current (AC) power generation, the devices are usually considered to be subject to a resistive load in the electrical domain [48–50]. To use the electricity produced by a piezoelectric

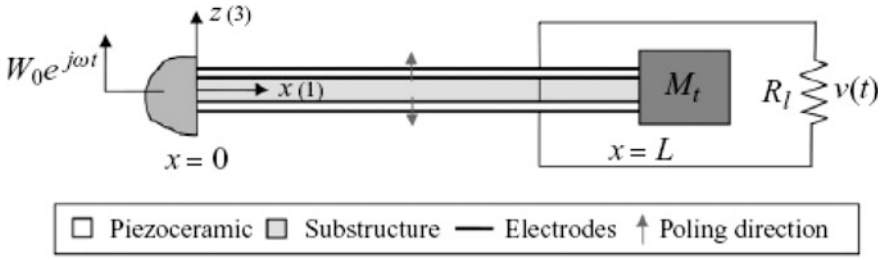

Fig. 2.20 Schematic cantilevered piezoelectric energy harvester tested under base excitation. Reproduced with permission from [46]. Copyright @ 2011, John Wiley & Sons

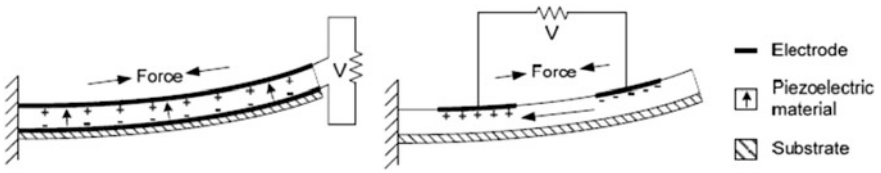

Fig. 2.21 Two types of piezoelectric energy harvesters: **a** d_{31} mode and **b** d_{33} mode. Reproduced with permission from [47], Courtesy of Dr. D. Zhu, University of Southampton

energy harvester, the alternating voltage output should be converted to a stable rectified voltage. This can be realized by using a rectifier bridge and a smoothing capacitor to form an AC–DC converter. The energy can be used to charge small batteries or stored in capacitors. To maximize the power transfer to the energy storage devices, it is also necessary to use a DC–DC converter to regulate the voltage outputs of the rectifier. These electrical circuit and power electronics are very important for practical applications of the energies harvested [51–53].

2.3.3 Modeling of Piezoelectric Energy Harvesting Devices

Modeling is an important approach to predict the performances of a piezoelectric energy harvesting device, which in turn can be used to optimize the design parameters to achieve further improvement. Therefore, tremendous efforts have been made to develop models of piezoelectric devices. In the early stage of mathematical modeling, [54, 55] lumped parameter solutions with a single mechanical degree of freedom were used to predict the coupled system dynamics of piezoelectric energy harvesters. Lumped parameter modeling is a convenient modeling approach, because the electrical domain already comprised of lumped parameters: a capacitor due to the internal (or inherent) capacitance of the piezoelectric materials and a resistor due to an external load resistance. Hence, the only prerequisite is to obtain the lumped parameters representing the mechanical

domain so that the mechanical equilibrium and the electrical loop equations can be coupled through the piezoelectric constitutive equations [45] and thus a transformer relation can be built up. One of the advantages of the lumped-parameter modeling is its use of simple expressions. However, it is limited only to a single vibration mode due to its approximation characteristics. It also misses several important aspects of a coupled physical system, such as the dynamic mode shapes and accurate strain distributions, as well as their effects on the electrical response.

Cantilevered energy harvesters are basically excited under base motion. The lumped-parameter harmonic base excitation relation for elementary vibration can be used directly [56, 57]. It has been used widely for both theoretical modeling [55] and experimental studying to maximize power generation and optimize parameter [58]. In lumped-parameter models, the contribution of the distributed mass to the forcing amplitude in the base excitation is usually neglected [54, 55]. The inertial contribution of the distributed mass to the excitation amplitude should be considered, especially when a harvester has not a large proof mass [59].

As an improved modeling approach was later developed to model cantilevered piezoelectric energy harvesters [60, 61]. Also, the vibration mode shapes obtained from the Euler–Bernoulli beam theory, along with the piezoelectric constitutive equation that gives the electric displacement to relate the electrical outputs to the vibration mode shape, have been used to obtain analytical expressions [62–64]. However, these approaches have several shortcomings, including the missing of the resonance phenomenon, misrepresentation of the forcing due to the base excitation, oversimplified modeling of the piezoelectric coupling in the beam equation by taking it as viscous damping and use of static sensing/actuation equations to describe the fundamentally dynamic problems [65].

Further developments in modeling of piezoelectric energy harvesters include analytical solutions based on distributed-parameter electromechanical modeling, which have been experimentally validated [66, 67], and others [68–71]. The linear electromechanical models have later been modified to cater for the mechanical nonlinearities in vibration-based energy harvesting devices [72–74]. A more recent modeling problem of interest is the stochastic excitation of vibration-based energy harvesters because some types of waste energy due to vibration often appear in nondeterministic forms [75].

2.4 Energy from Human Activity

2.4.1 Shoe-Mounted Harvesters

2.4.1.1 Examples of Shoe-Mounted Piezoelectric Harvesters

Several examples have been reported that use piezoelectric harvesters mounted in shoe to harvest mechanical energy due to human walk or running [76–82]. A representative photograph of shoe-mounted piezoelectric energy harvesters is

Fig. 2.22 Prototype of the piezoelectric film energy harvesting device inserted in a shoe. There are two DT4-028 K/L piezoelectric films from MSIUSA in parallel inside the shoe. Reproduced with permission from [82]. Copyright @ 2006, Elsevier

shown in Fig. 2.22 [82]. One of the earlier examples is described in. In Ref. [76], where two main methods are explored, with 31-mode bending operation. One method is to harness the energy dissipated in bending the ball of the foot, using a flexible, multilaminar polyvinylidene fluoride (PVDF) bimorph stave mounted under the insole. The second method is to harness foot strike energy by flattening curved, pre-stressed spring metal strips laminated with a semiflexible form of piezoelectric lead zirconate titanate (PZT) under the heel. This device is called dimorph, consisting of two back-to-back single-sided unimorphs.

The multilaminate piezoelectric foil stave has an elongated hexagonal shape. It consists of two eight-layer stacks of 28 μm PVDF sandwiching a 2 mm flexible plastic substrate bounded with epoxy. The hexagonal design is to maximize the integrated stress across the bending distribution of a typical insole with a shape of shoe. Bending the stave elongates its outside surface and compresses its inside surface with respect to its plastic core due to the difference in curvature radii. The PVDF sheets on both sides of the core are connected with silver electrodes in parallel. The charges in the 16 layers add up and a voltage drop builds up across the two electrodes. Bending and restoring the stave create energy due to the deformation of the piezoelectric PVDF layers.

The PZT device is to harvest the energy due to heel strikes. A simple unimorph is used first and nonbending compressive dimorph is developed. Two commercially available PZT transducers, a heel-shaped 0.025 in. beryllium-copper midplate and two aluminum rivets are used to assemble the device. The transducers consists of a 5 cm × 5 cm, 0.015 in. PZT strip bonded to a prestressed neutrally curved sheet of spring steel with a size of 5 cm × 8.5 cm. The whole structure is trimmed to fit the beryllium-copper midplate and then mounted under the heel-strike force center with two rivets. It is thus ready to be connected with electrodes with electric parallel. When the dimorph is compressed first and then released, charges are accumulated across the surfaces of the PZT strips.

The PVDF stave has been tested under the insole of a standard athletic sneaker and the PZT dimorph is in an orthopedic insole in work boot. The athletic shoe's

insole is flexible to accommodate the flexible stave, while the rigid heel cup of work boot is suitable to the rigid dimorph. Energy harvesting efficiency can be measured by terminating the transducers with matched resistive load and measuring the voltage output during a brisk walk of a wearer.

The PVDF stave has an average power of 1.3 mW in a 250 kΩ load at 0.9 Hz walking pace, whereas the PZT dimorph offers an average power of 8.4 mW in a 500 kΩ load under the same mechanical excitation. The footfall has evident characteristics, with a large spike followed by a smaller one. The larger power spike corresponds to the rapid initial bending or compression of the devices, while the following smaller spike is caused by the restoration of the transducer when the wearer shifts weight from one foot to the other. Power efficiencies of the PVDF and PZT harvesters are 0.5 and 20 %, respectively.

The energy harvested by using the PVDF and PZT shoe-mounted harvesters has been used to power a radio frequency (RF) tag system to demonstrate the feasibility for potential self-powering applications. An active RF tag, which can transmit a short range 12-bit wireless identification (ID) code while the bearer walks, is used in the demonstration. Such a system can be used in a smart environment, in which multiple users transmit their identities to the local surrounding. Because the RF-based design does not require line of sight to the reader, it can be mounted in a shoe. The piezoelectric harvesters provide energy to power the system, without the use of batteries.

Low frequency mechanical energy sources, like walking of human, are purely capacitive, which usually produce high voltage, low energy density and low level of current at about one cycle per second. The excitation corresponds to an extremely high source impedance, with voltage outputs of hundreds of volts and currents on the order of 10^{-7} A. Therefore, linear regulation is not sufficient to make the energy for real applications during a brisk walk. To further make use of the energy harvested by using the shoe-mounted piezoelectric harvesters, various switching conversion strategies have been developed, including switched-capacitor converters, direct DC–DC down converters and forward-switching converters. The forward-switching converter is comprised of a small number of inexpensive widely available components and materials.

Another example of shoe-mounted piezoelectric energy harvester is made with PVDF unimorph [77]. The unimorph strips are constructed with one 0.5 in. tall, 52 μm thick silver laminated PVDF films, bonded with cyanoacrylate to the side of a slightly wider and longer 4 mil thick PET plastic film substrate. The strips vary in length with the changing space available in the cutout from 1 to 2.25 in. The substrate has suitable stiffness and spring-like qualities for the harvester applications. During a heel strike, the polycarbonate plates are compressed together, in which all the PET strips aligned between them are bent. A strain is thus applied to the bonded PVDF film, due to the bending of the plastic strips. After optimization, the shoe-mounted harvester can have a power of 4 mW and energy efficiency of 8 %.

The last example of shoe-mounted piezoelectric harvester is also made of PVDF [78]. PVDF with β phase is dissolved in N,N-dimethyl formamide or

dimethyl acetamide at temperature at temperatures of <70 °C, to make thin films of 20–60 μm. PVDF thin films with oriented crystal structure can be obtained by stretching. The films are then poled to have improved piezoelectric performance. Metallic films (such as Au) are deposited on both sides of the PVDF thin films as electrodes by magnetron sputtering or thermal evaporation. Piezoelectric harvester made with the PVDF thin film is then mounted at bottom of a shoe. A shaker is used to apply mechanical excitation similar to that of human walking. A maximum output voltage of about 6 V is produced by a harvester made with 28 μm thick PVDF films. The signal can be rectified so that the harvested energy can be stored for real applications, which has been demonstrated by using a rechargeable lithium battery. The lithium battery is a thin film all-solid-state storage device, having a capacity of 35 μAh cm^{-2}, with current densities of above 200 μA cm^{-2} and less than 10 μm in thickness. The batter consists of $LiCoO_2$ as cathode, Li_3PO_4 as electrolyte and Li as anode. Although the energy generated by the shoe-mounted harvester is still not sufficient for practical applications, it has potential to be further improved.

2.4.1.2 Gait Analysis for Shoe-Mounted Harvester

To effectively make use the kinetic energy from human working by using shoe-mounted piezoelectric harvester, it is very useful to have a deeper understanding on the gait pattern. Previous studies have indicated that foot movement of human is characterized by large displacements and accelerations, which is thus very promising sources of vibrating mechanical energy that can be harvested by using shoe-mounted devices. The high velocities and accelerations are observed in foot movement, especially during the foot/ground contact phase [81]. As an example, Fig. 2.23 plots a typical acceleration time history measured in the calcaneous of one limb, in one gait during normal walking (the gravitation acceleration has been subtracted already). Several significant features are mentioned as follows. First, the acceleration peak at heel strike (A, G) is followed by certain oscillation after heel strike (B). Second, there area baseline during stance phase (C) and an acceleration during foot movement (D–E). Finally, there is a downward acceleration at heel strike (F) [81].

To effectively harvest the energy with shoe-mounted piezoelectric harvesters, it is import to understand the characteristics of gait cycles of human movement. Human foot movements are characterized by gait cycles as a well-defined sequence. Within a sequence of two consecutive heel strikes, i.e., “contact phase,” of the same limb, the gait actually consists of a “stance phase” when the foot is at rest and a subsequent “swing phase” when the foot starts to move [83]. The contact phase is usually instantaneous, while the stance and swing phases take approximately 60 and 40 % of a single gait cycle [84]. The heel starts moving at approximately 40 % of the stride while the foot is still in contact with the ground and reaches its maximum displacement just after toe-off, when the velocity of the heel is approximately zero. During the upward and downward heel movements in

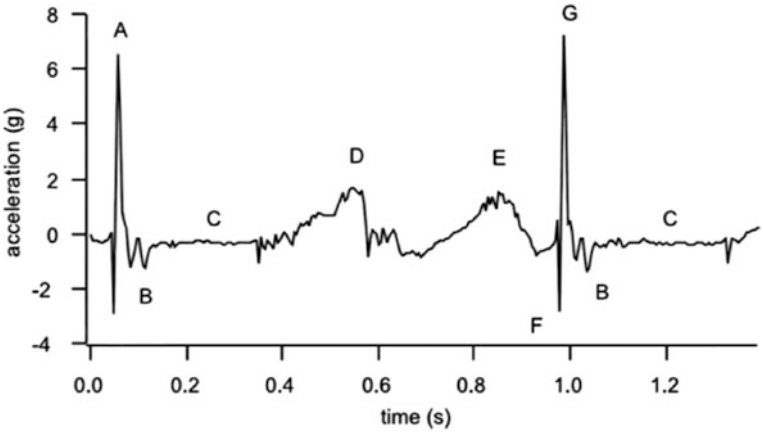

Fig. 2.23 Acceleration signal of the calcaneus for one complete gait (heel strike to heel strike of the same limb). The accelerations are normalized to that of gravity $g = 9.81\ \text{ms}^{-2}$. Reproduced with permission from [81]. Copyright @ 2001, Elsevier

the swing phase, the velocity has a sinusoidal trend, while the acceleration shows some oscillation consequent to velocity change [85].

The vertical and horizontal accelerations in the foot are potential vibration sources of energy to be harvested. The acceleration signal shown in Fig. 2.23 that every heel strike has a large acceleration, followed by certain oscillation during the swing phase. The observed acceleration spikes have been confirmed by the measurement of ground reaction forces under the foot [86]. The heel acceleration has been shown to vary due to several factors, such as characteristics of the ground surface, conditions of gait, types of shoes, status of the walkers. Therefore, different walking conditions lead to acceleration signals with different characteristics. A common sense is that a variation in these walking conditions has only influences on the measured values, without significant change in the overall trend [81]. In this respect, an experimental measurement of gait acceleration time histories is essential to identify all the relevant features, so as to have a standardized acceleration signal that can be used as a reference excitation in numerical evaluation of the electromechanical response of a shoe-mounted vibrating device.

Such experiments have been conducted by using a custom-made clamp system to fix on the heel pad, while an accelerometer is aligned along the tibial axis. Gait accelerations, of a male subject (1.75 m in height and 70 kg in weight) walking on a level walkway at a natural pace (about 0.8 steps s^{-1} for the same limb), have been measured with five repeated tests [79, 80]. The signal is virtually periodic and contains all the relevant features observed in the acceleration time history of Fig. 2.23. At contact phase, a large acceleration spike is followed by a negative valley, which is most likely caused by the mid-foot and toe impact to the ground. During the stance phase, the acceleration is almost zero, while it exhibits a sinusoidal-shaped oscillation during the swing phase.

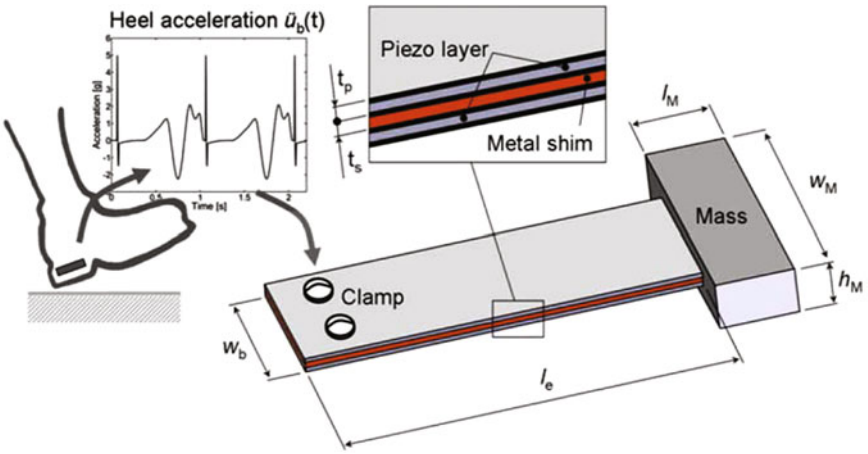

Fig. 2.24 Rectangular bimorph excited by heel acceleration at its base. Reproduced with permission from [79]. Copyright @ 2013, Springer Science+Business Media

The information has been used to synthesize all the relevant features of gait acceleration into a periodic acceleration signal, as a reference input in numerical simulations of an electromechanical bimorph. The standard acceleration signal can be established by combining the values of vertical and horizontal displacements, velocity and acceleration, as well as the typical time variation of the foot–ground angle during walking. For example, the average step distance is 65 cm [87] and the maximum vertical heel elevation is about 25 cm [85], where the foot–ground angle reaches its maximum of 46° [86], with other aspects being also taken into account [81]. All these have been validated by experimental measurements, for the definition of acceleration during the contact phase. Finally, the periodic standard acceleration signal can be obtained. There are certain typical features, including two sharp positive/negative peaks in the contact phase, an oscillation in the swing phase, followed by a small double peak, due to the vertical and horizontal accelerations [79, 80].

Having these data, the electromechanical response of a shoe-mounted vibrating scavenger excited by heel acceleration during human gait can be simulated, with bimorph as an example [79, 80]. As shown in Fig. 2.24, the bimorph has a rectangular shape, made of two piezoelectric layers bounded to a metallic shim. One end is clamped, a tip mass is mounted on the other end, which reduces the natural frequency of the bender. Material properties are typical PZT-5A piezoceramic and stainless steel.

Figure 2.25 shows the results of theoretical simulation and experimental measurement for the shoe-mounted bimorph excited by the nonharmonic heel acceleration [79]. The simulation and the experiment are in a very good agreement, which means the standardized acceleration signal, even if somewhat simplified, represents all the relevant features of gait acceleration to reproduce the real measured signal. Therefore, it can be conveniently used as a reference of the

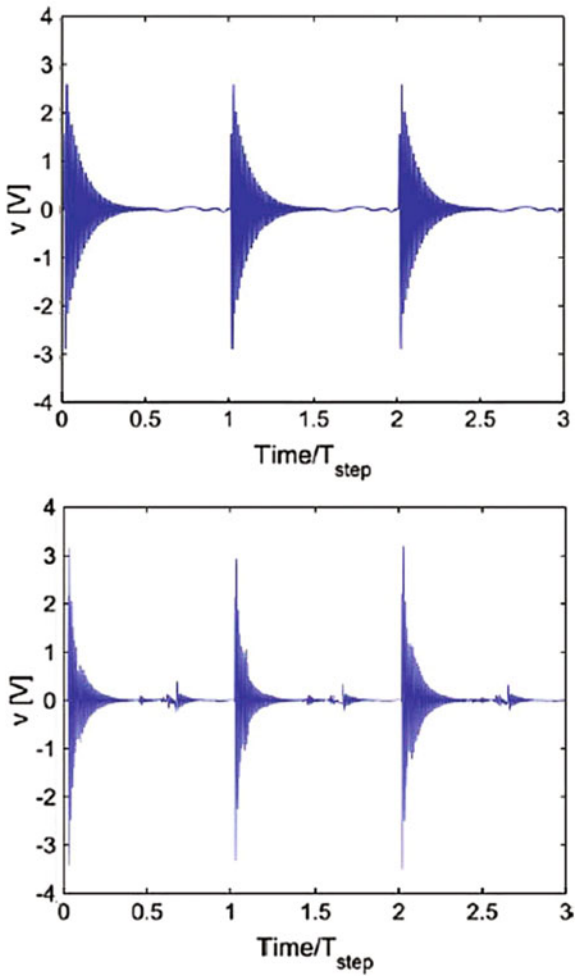

Fig. 2.25 Transient output voltage at heel acceleration for three heel strikes of the same foot: **a** numerical simulation and **b** experimental measurement results. Reproduced with permission from [79]. Copyright @ 2010, IoP Publishing

measured signals to simulate and predict the dynamic responses of shoe-mounted harvesters.

The performance of a shoe-mounted piezoelectric harvester can be represented by the average power per footstep dissipated across the resistance R_L, given by:

$$P_{\text{ave.}} = \frac{1}{n_s} \int_0^{T_{\text{step}}} \frac{v^2(t)}{R_L} \mathrm{d}t, \tag{2.18}$$

where n_s is the number of footsteps counted in the time period T_{step}. This definition of power is independent of pace frequency or period. It can be used to compare the performance of harvesters with different materials and configurations.

Experimental data indicate that the power harvested per step is about 13 μW, just about 6 % higher than the power calculated numerically with the standard acceleration input. Such a small difference can be attributed to the unpredictable low-level oscillations observed in the measured signal. Also, the consecutive steps may provide slightly different acceleration signals, even under same stable walking conditions. Although for practical applications the obtained power levels are still not sufficiently high, there are rooms for further improvement. For example, the performance of the harvester can be optimized through materials selection and structure design. Nevertheless, the simulation method can be used to estimate energy harvesting performance of a given device.

2.4.2 Energy from Human Body Motion

Human activities, with the exception of vocalization, occur at very low frequencies, only up to a few hertz in most cases. It has been well known that piezoelectric bimorphs operating for sensing or energy generation are most effective at quite high frequencies. Devices of acceptable dimensions and mass for human integration and offering power outputs in the order of milliwatts have resonance frequencies of hundreds of hertz. This frequency mismatch between excitation and harvester makes it challenging to efficiently harvest energy from human motion with piezoelectric devices. As a result, various strategies have been proposed to address this problem. One of them is called frequency up-conversion method, where the low frequency motions are used as an excitation to trigger the piezoelectric components to vibrate at their resonant frequencies, which is the focus of this subsection. The harvesters in the following discussion are grouped according to the types of target energy sources instead of the harvesting principles.

2.4.2.1 Impulse-Excited Harvesters

In this section, three examples will be discussed on energy harvested from human body motion by using piezoelectric harvesters [88–90]. The first example is a piezoelectric impulse-excited approach, in which a cylindrical proof mass actuates an array of piezoelectric bi-morph beams through magnetic attraction [88]. With an initial excitation, the transducers start to vibrate at natural frequency. By using this approach, the operational frequency range can be widened while the electromechanical coupling is significantly increased. The principle of the impulse excitation is demonstrated by using a commercially available integrated circuit for voltage regulation. At a frequency of 2 Hz and an acceleration of 2.7 m s^{-2}, the harvester has a maximal power output of 2.1 mW. This type of harvesters can be used for promising medical applications, for example, as power suppliers for wearable and implantable sensors for heart rate, blood glucose level, blood pressure and oxygen saturation.

There is a limit in the achievable power output for inertial devices, which is given by:

$$P_{\max} = \pi f a_0 Z_L m, \tag{2.19}$$

where $f = \omega/2\pi$ is the excitation frequency in Hz, a_0 is the external acceleration, Z_L is the internal displacement limit and m is mass of the seismic element. Here, a sinusoidal excitation, with acceleration $a(t) = a_0 \sin(\omega t)$, is assumed. More commonly, a_0 is expressed in terms of external motion amplitude Y_0 and angular excitation frequency ω as $a_0 = Y_0\omega^2$. This equation gives an upper limit regardless of actual transduction mechanism, because only the mechanical kinetic energy is calculated. Moreover, for resonant designs, Y_0 is smaller than Z_L, whereas for nonresonant devices, Y_0 can be much larger than Z_L.

There are several characteristics of human motion that must be taken into account. First, the excitation frequencies that determine the power output are usually very low. Second, different points of human body have different frequencies and accelerations. For instance, in normal gait, the highest excitations are about 2.5 g and 1.7 Hz at the ankle, while for chest, shoulder, and wrist, it is about 0.3–0.5 g and between 1 and 2 Hz [88]. At the same time, the displacement limit and mass are should be also considered in practical designs.

The theory only predicts the amount of the kinetic energy stored in the proof mass, while the performance of actual devices is related to the conversion mechanism. Therefore, to maximize the efficiency of a harvester, it is necessary to the effectiveness of the transducer used, i.e., the percentage of the available inertial energy that can be actually converted into electrical energy. In this respect, impulse excitation of the transducer has such characteristics. The approach involves two steps. A large proof mass moves under external acceleration at low frequency. This mass periodically transmits an impulse to the actual transducer, which then vibrates at a higher frequency [88]. However, such a device is still limited by the kinetic energy of the large proof mass. To achieve the maximum performance, the transducer needs to work under its ideal conditions.

The impulse-excited harvesters have another advantage, broad range of working frequency. Every time the transducer is actuated, a fixed amount of energy is converted. If the excitation frequency is increased, the number of actuations of transducer is increased, so that the power output is increased. At resonance frequency, the power output of a device with continuously optimized damping and spring constant increases as cube of frequency. However, the power output of the impulse-excited devices is linearly proportional to frequency. Theoretically, if the excitation is too slow, the proof mass fails to actuate the transducer at all, corresponding to a drop power output at a specific frequency, which is similar to a critical frequency.

Figure 2.26 shows a prototype of the piezoelectric impulse excited harvester [88]. This design has taken into account the challenges for human body energy harvesting. An external steel cylinder is used as a proof mass due to its high density. An electrostatic device with a rolling rod is specifically developed, with a

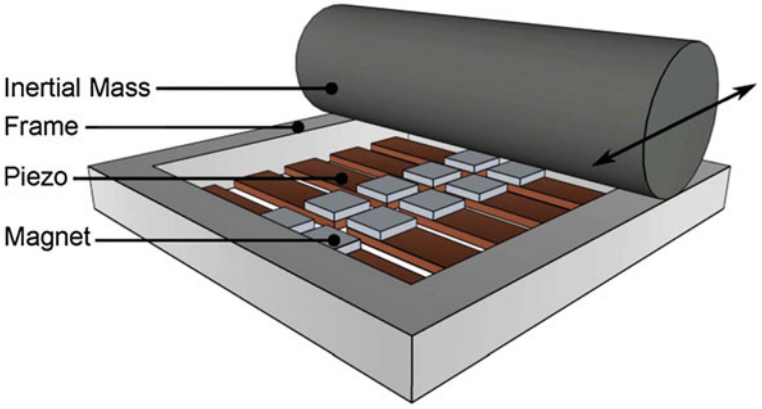

Fig. 2.26 Impulse-excited piezoelectric harvester prototype. Courtesy of P. Pillatsch, Imperical College London. Reproduced with permission from [88]. Copyright @ 2012, IoP Publishing

high coupling over the given travel range. In this piezoelectric approach for energy conversion, a series of bi-morph piezoelectric beams are used transducers. The tip of each beam is attached with a permanent magnet. When the proof mass rolls over one element, the magnet snaps onto the steel cylinder and the beam bends, as shown in Fig. 2.27. As the proof mass continues its travel, the beam is released and oscillates freely at its damped natural frequency.

In this design, the device is in perpendicular direction of proof mass motion and transducer actuation. As a result, the travel range of the proof mass is not limited by the actuation range of the transducer. Also, the actuation forces can be spread over a larger number of individual transducers and adjusted by changing their shapes. According to above theory, with an initial gap, for example, h = 1 mm, the required force on each single beam for optimal operation as a function of excitation frequency and total number of beams can be obtained. This segmented transduction is the reason that the bandwidth can be effectively widened.

Figure 2.28 shows a macroscale functional model as a proof of concept [88]. Two cylinders machined from mild steel have masses of $m_1 = 285$ g and $m_2 = 143$ g (half mass of m_1), which are used to check the influence of mass on power output of the device. Two rails, with adjustable heights, constrain the travel to linear motion with two blocks acting as variable end stops. At each side, a clamping mechanism holds eight piezoelectric beams. The beams having a dimension of $72 \times 5 \times 0.5$ mm^3 are cut out of a series of connected bi-morph plate. The top and bottom layers are made of PZT 507 material (Morgan electroceramics) with a thickness of 0.2 mm. The center shim consists of a thin layer FeNi alloy with thickness of 0.1 mm. These beams are clamped to a free beam with a length of 60 mm. The tip mass is N52 type neodymium magnets with a dimension of $5 \times 5 \times 1$ mm^3. Consequently, the device has a damped natural frequency of 46.3 Hz. Each single beam has a capacitance $C = 30$ nF. Therefore,

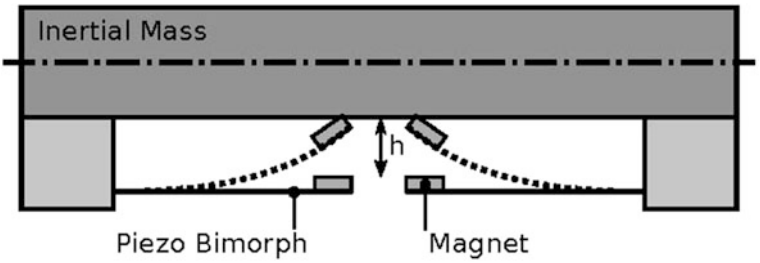

Fig. 2.27 Section view of the prototype, showing the bending of the beams. Courtesy of P. Pillatsch, Imperical College London. Reproduced with permission from [88]. Copyright @ 2012, IoP Publishing

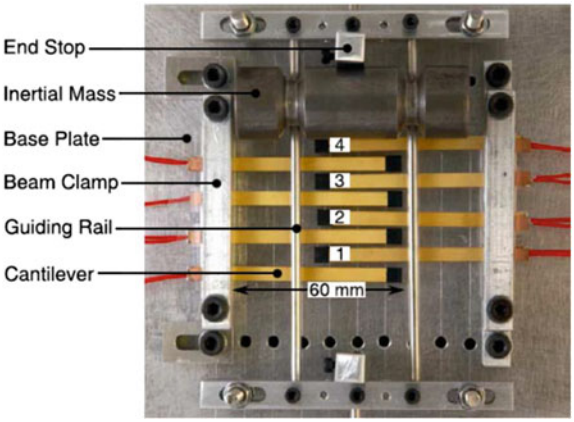

Fig. 2.28 Functional model of the impulse-excited harvester. Courtesy of P. Pillatsch, Imperical College London. Reproduced with permission from [88]. Copyright @ 2012, IoP Publishing

according to the output impedance of the beam, i.e., $Z = 1/\omega C$, the matched resistive load for maximal power output is $R = 120$ kΩ. The corresponding values of the results are calculated as the measured root-mean-squared (rms) voltage squared divided by this load resistance.

A rocking table has been used to describe the functional model, which is used for reproducible excitations [88]. The angular velocity ω of the driving wheel is adjustable between 20 and 120 rpm, and 0.33 and 2 Hz, respectively. This motion is transferred to the platform through a connection rod giving rise to a sinusoidal excitation:

$$a(t) = g\frac{r}{L}\sin(\omega t) = a_o \sin(\omega t), \tag{2.20}$$

where L is the distance between the rotational axis of the platform and the mounting point of the connection rod and g is the gravitational acceleration. The radius r stands for the eccentric position of the connection rod on the driving wheel. By adjusting r, the tilt angle of the table can be changed. At angles of 16.1°

and 5.1°, a high acceleration $a_1 = 2.7$ m s^{-2} $\approx$ 0.28 g and a low acceleration $a_2 = 0.87$ m s^{-2} $\approx$ 0.089 g are obtained. This allows for four possible configurations between masses, m_1, m_2, and accelerations, a_1, a_2.

The measurement setup also has a piezoelectric energy harvesting power supply (Linear Technology LTC3588-1). It contains a full wave bridge rectifier and a DC–DC converter with selectable regulated output and an input voltage range between 2.7 and 20 V, with a dimension of 3×3 mm^2. The values are: $C1 = 1$ μF, $C2 = 4.7$ μF, $C3 = 47$ μF, $C4 = 10$ μF and $L1 = 10$ μH.

The open circuit voltage on a single beam for one actuation has been measured and explained [88]. As the proof mass approaches the beam, the magnet latches onto it, pulling the tip of the beam up. Initially, the beam stays in this deflected position as the cylinder continues its traveling. In second phase, the corner of the magnet holds onto the proof mass and the beam is pulled up further due to the curvature of the cylinder, before is finally released and vibrate freely. This is an ideal scenario because the release occurs just after the equilibrium at which point the beam force matches to the magnetic attraction.

When the device is continuously operated at 0.33 Hz, beam 4 is actuated first, followed by beam 3, and then beam 2 and finally beam 1. The oscillation of the individual beams has completely stopped before the next actuation is started. If the continuous operation is at a higher frequency of 1.66 Hz, the above-mentioned advantage of the segmented transduction is demonstrated. Although beams 1 and 2 are not actuated at all, beams 3 and 4 are wording very well. It means that the device can also be used to harvest energy at this higher frequency, indicating its wide range of operating frequency.

The measured power output of the whole device and the corresponding rms voltage of a single beam have been characterized for four described measurement configurations with different proof masses and external accelerations [88]. It has been found that the power output curves, especially in the cases of large accelerations, the expected linear behavior is observed, i.e., the power output doubles at the frequency is doubled. The rms voltages on each beam are within a usable range of 2–6 V.

Ideally, the device should be operated at low acceleration with light proof mass, because this is the case in which the amount of the available kinetic energy matches that of the energy that can be extracted by the transducers in each cycle. This has been confirmed by experimental results. Up to about 0.5 Hz all four curves are very close to each other. At high accelerations, although the amount of the energy stored in the heavier proof mass m_1 is high, the transducers cannot extract it. Therefore, no energy is harvested, in contrast to the case of the lighter proof mass m_2 at frequencies above 1.7 Hz. At this frequency, m_2 does not travel the full range and thus the level of the output power drops. Similar behavior is observed for lower acceleration a_2, but with the breakdown point occurs at a lower frequency of about 0.5 Hz for m_2 and about 0.7 Hz for m_1. This can be readily understood that the kinetic energy of the proof masses is smaller at lower accelerations. The harvester has a maximum output power of 2.1 mW at 2 Hz.

The device has a maximum power efficiency of about 8 %, when the proof mass just about touches the end stops and energy lost in collisions is at the minimized level. This implies that a proper match between the transducers with optimized excitations and the intended proof mass is important for high power efficiencies. This can be taken into account during device design, for example, higher proof masses can be realized by simply using thicker beams. At certain combinations, for instance, a_1 plus m_2, pretty high level of power efficiency ($\sim$3 %) can be maintained over the whole frequency range, confirming again the wide bandwidth capability of the impulse excitation approach. The device exhibits a power density of 3.8–13 μW cm^{-3}, with proof mass m_2 at high acceleration $a_1 = 2.7$ m s^{-2} $\approx$ 0.28 g and excitation frequencies of 0.33–2 Hz. The low operation frequency, wide frequency range, and relatively high power density, make the harvester very favorable for human body applications.

The LTC3588-1 voltage regulator has been tested on a single beam at high acceleration a_1 and with the lighter proof mass m_1 between 0.33 and 2 Hz. The voltage from the piezoelectric actuator is first rectified to charge the input capacitor connected to V_{in}. Once a threshold of 5 V is reached, a certain amount of charge is transferred to the output capacitor. As a result, the output voltage rises in steps until it reaches the predefined level of about 3.6 V.

The power output after voltage regulation is determined by using a variable resistor with initial value of 1,050 kΩ. After the target level is reached, the resistance is decreased, so as to increase the load current, until the voltage at the output terminals starts to drop. The power can then be calculated as the chosen output voltage squared divided by the resistance ($P = V^2/R$). An efficiency of close to 40 % is observed. Furthermore, at 0.33 Hz, because the consumption of the load is too high, the level of output voltage is always below 3.6 V and an equilibrium instead of a drop at a lower level is attained after every transfer of charge coming from the input capacitor.

2.4.2.2 Impact-Driven Harvesters

The second type of piezoelectric devices is called impact-driven harvesters, specifically harvesting mechanical energy due to human body motion [89, 90]. A design based on the impact of a moving mass on piezoelectric bending structures will be discussed first [89]. With the aid of theoretical analysis, the parameters influencing the device performances in terms of energy harvesting have been optimized. Experimental results on a prototype of the impact harvester have shown that a generator with a volume of 25 cm^3 and weight of 60 g has an output power of 47 μW, which is measured across a resistive load when the device is rotated by 180°/s. At 10 Hz, 10-cm amplitude linear motion results in a power of 600 μW.

The piezoelectric element in this impact-driven harvester is a bimorph, consisting of two piezoelectric capacitors supported by an elastic cantilever. An additional mass can be added at the tip of the bimorph. The piezoelectric capacitors can be arranged in series or parallel configuration, which are connected to the

powered device through a signal conditioner. The principal deformation of the piezoelectric layer occurs along the direction (axis-1) perpendicular to the direction (axis-3) of polarization in the piezoelectric layer, so that the piezoelectric material is excited in the transverse e_{31} mode. The parameters of the electrical load can be tuned to optimize the transfer efficiency of energy from mechanical to electrical domain.

For energy harvesting due to vibration, piezoelectric bimorphs should be designed according to resonant frequencies. In this case, the behavior of the bender can be approximately treated a mass-spring system damped by electrical dissipations. Therefore, the bimorph has to be excited at a frequency close to its fundamental frequency ω_0 in order to maximize the output power. If the displace is not limited, the power generated is dependent on ω_0^3. For this reason, resonant vibration harvesters are usually used to harvest energy from vibrations in an 'industrial' environment, for example, on the motor of a vehicle. This type of harvesters is not able to harvest the energy due to the motion of human body occurring at very low-frequencies (<25 Hz) and irregular motion of the limbs.

Although this problem has been addressed by applying mechanical excitation directly to piezoelectric transducers, such as shoe-mounted harvesters discussed above, this type of devices is relatively large and the energy harvested must be transmitted to devices to be powered in on another part of human body. Therefore, inertial principle has been used as an alternative method, where the harvesters can be located with the sensors to be powered. Also, if the slow body vibrating can be transferred to high-frequency cantilevers, the energy can then be harvested. The impact-driven harvester is developed by taking these into account. Figure 2.29 shows conceptual representation of the system. It consists of a frame with a channel inside which allows for free sliding of a mass and two piezoelectric bimorphs located at two sides of the frame. If the frame is shaken along the direction of the channel, the mass strikes the piezoelectric cantilevers alternatively. Kinetic energy of the moving object can be harvested by the piezoelectric harvester. The device to be powered is also included inside the frame.

The impact-driven harvester can be described by using an electrical network model [89]. There are several requirements for piezoelectric bimorph to be represented by an electrical network. The constitutive equations relating mechanical and electrical variables are linear. The magnitude of displacements is small. The mechanics of the bimorph can be described by using Euler–Bernoulli beam theory with assumption of plane stress or plane strain. There is an ideal interface between the elastic and piezoelectric layer. The mechanical input applied to the harvester can be accurately represented by a concentrated force and excites only the fundamental vibration mode of the bimorph.

Because all these requirements are met for the impact-driven harvester, the behavior of the piezoelectric bimorph can be described by a circuit shown in Fig. 2 in Ref. [89]. The mechanical part of the system is represented by the series association of an inductor m and a capacitor k. m and k correspond to the effective mass and the stiffness of the bender, respectively. k is a complex quantity, which can be expressed as $k = k'(1 + j/Q)$, so that parasitic dissipations are represented

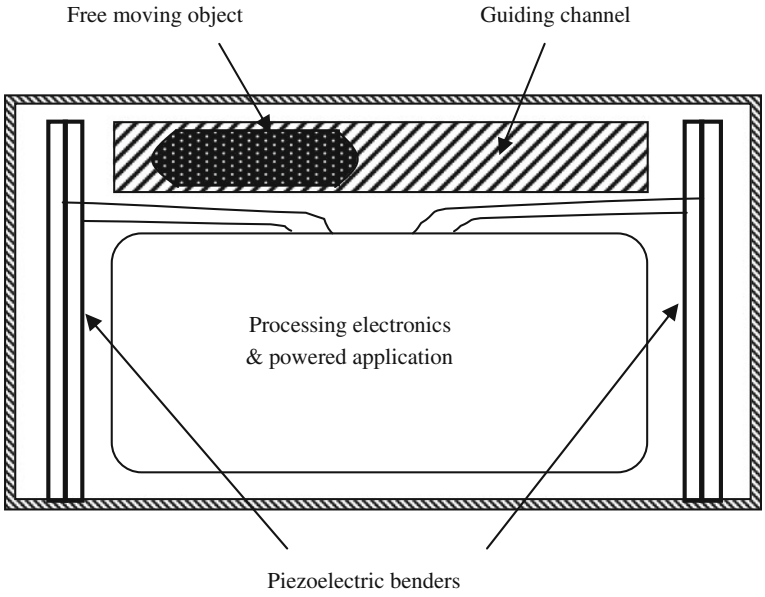

Fig. 2.29 Conceptual representation of the impact-based vibration energy harvester. Courtesy of M. Renaud, Interuniversity Microelectronics Center (IMEC). Reproduced with permission from [89]. Copyright @ 2009, IoP Publishing

in the model through the quality factor Q. F and δ stand for the concentrated force due to the mechanical excitation and the deflection at the position of the force applied. The mechanical elements are connected to the piezoelectric capacitor with a capacitance C_p through a perfect transformer with a ratio of Γ:1. C_p is the clamped capacitance, which is measured when the piezoelectric layer is not deformed. The coefficient Γ is directly proportional to the piezoelectric constant e_{31}. Finally, I and V are the electrical current injected into the capacitor and the voltage developed across the electrodes of the piezoelectric layers.

The analysis has been limited to one-dimensional collision on a flexible beam. The velocities of the objects and the mechanical excitation due to the collision are assumed to be in the direction perpendicular to the surface of the beam. The contact surfaces are supposed to be perfectly smooth, so that the friction mechanisms can be neglected. The impact has different phases. First, the moving object approaches the beam at a velocity which is dependent on the particular excitation applied to the frame of the device in Fig. 2.29. The impact process consists of two separate phases.

In the first phase, the two objects tend to interpenetrate each other and a local compression referred to as indentation δ_i is observed in the area surrounding the contact point. The contact area becomes larger as the magnitude of the indentation is increased. The compression phase ends when the amplitude of the restoring elastic force $F(t)$ is large enough to induce a local expansion of the two bodies

which tend to repulse each other at this moment. During the contact time, radial waves due to the indentation start propagating away from the impact location. The contact area and the magnitude of the indentation are small, so the corresponding radial waves do not have an important influence on the macroscopic behavior of the two bodies and thus can be ignored. Another wave consisting in a vertical displacement is initiated in the beam during the impact process; it is referred to as a bending wave that results from the exchange of momentum between the two objects. After the expansion phase, the two objects separate with velocities in opposite directions. The object also oscillates along its own eigenmodes after the separation. Because the moving object is assumed to be very stiff, these oscillations do not have any effects on the general dynamics. In the beam, the bending wave propagates further away from the impacted vertical segment. The behavior of the bender prior to a second impact can be treated as free oscillations.

The analysis of the model has revealed several important aspects. The contact force $F(t)$ can be expressed by the Hertz model. The dynamics of two spherical contact surfaces during an elastic impact can be represented by a simple model consisting of two lumped masses connected by a nonlinear spring k_i, which creates a contact force of $k_i\delta_i^{3/2}$. The lumped mass associated with the impacted segment of the beam corresponds to its effective mass m. For the impacting process, this corresponds to its full mass M. The indentation stiffness k_i can be expressed in terms of the curvature radius of the impacting surfaces and certain compliance components.

The moving object can be treated to be perfectly rigid, so the equations of motion for the indentation δ_i and the displacements of the two bodies have been established through the Euler–Bernoulli beam model. The equations can be solved analytically by having certain assumptions. If the nonlinear contact force can be described by a sinusoidal pulse of angular frequency ω, there is $F(t) \approx F_c \sin \omega(t)$, with $t_i < t < t_i + t_c$, and otherwise $F(t) = 0$. F_c is the maximum amplitude of the impact force, t_i is the time at which the two objects collide, and $t_c = \pi\omega$ is the contact time. F_c and ω can be obtained by solving the equation of motion for the indentation.

Numerical values of F_c and t_c can be obtained with the dimensions of the bimorphs: $W = 10$ mm, $l = 25$ mm, $t_s + 2t_p = 800$ μm, without an attached mass. The relevant values of stainless steel moving object and NavyIII-PZT5A of the beam are: $\varepsilon_{33}^E s_{33}^E = 15.6$ pPa^{-1}, $\varepsilon_{13}^E = -4.8$ pPa^{-1}. The radius of curvature at the contact surface is 5 mm while the beam is flat. M is 4 g and the average density of the beam ρ is 7,600 kg m^{-3}. The relative approach velocity U_0 is set to 1 m s^{-1} ($U_0 = v_{b0} - v_{M0}$, with v_{b0} and v_{M0} being the velocity of the impact points of the beam and the sliding object just before impact, respectively). With these values, there are $F_c = 15$ N and $t_c = 7 \times 10^{-6}$ s. The numerical expression of $F(t)$ can be used to check the validity of the last assumption to develop the network model of the bimorph. Combined with finite element (FE) simulation, it is found that the single-mode approximation lead to negligible errors in the general dynamics of the system [89].

Because the contact time is very short as compared to the fundamental period of the bender, the velocity of the impacted segment in the beam and of the moving object, due to the impact process and the corresponding pulse, can be redefined quasi-instantaneously. In this case, the dynamic behavior of the system can be treated to be discontinuous at the moment of the collision. The velocities of the two objects before (v_{b0} and v_{M0}) and after (v_{b0}' and v_{M0}') the impact can be obtained with the fact that the variation in momentum during the compression-expansion phase is equal to the time integral of the pulse $F(t)$. However, the momentum principle is only valid when it is a perfect elastic impact without energy dissipations. In practice, there have complex dissipation mechanisms in the collision, such as heat due to viscoelastic or internal friction and local plastic deformations. All these factors result in a decrease in the time integral of the impulse.

To account for these loss mechanisms, an energetic coefficient of restitution e is defined for each body. It is the square root of the ratio of the work W_c done on the contact surfaces during the compression over the work W_e done by the force in the expansion phase. That is: $e_b = (W_{e,\,b}/W_{c,\,b})^{1/2}$ for the beam and $e_M = (W_{e,\,M}/W_{c,\,M})^{1/2}$ for the sliding object, with e_b and e_M being the fractions of energy dissipated in each body during the compression-expansion. Similarly, it is further to define an effective coefficient of restitution e_{eff}, which relates the energy in the system before ($W_{c,\,b} + W_{c,\,M}$) and after ($W_{e,\,b} + W_{e,\,M}$) impact. This is particularly useful to the impact-driven device due to the very short duration of the impact process. The magnitude of e_{eff} depends on the effective masses, the curvatures and areas of the contact surfaces, the material properties, and the relative collision velocity. Generally, e_{eff} decreases as U_0 is increased. The values of e_{eff} have been determined experimentally. According to the energy conservation principle, the velocities of the two bodies after the impact can be expressed in terms of their velocities before the impact as follows:

$$v_{b0}^{'} = \frac{mv_{b0} + Mv_{M0} - e_{\text{eff}}M(v_{b0} - v_{M0})}{M + m}, \tag{2.21}$$

$$v_{b0}^{'} = \frac{mv_{b0} + Mv_{M0} + e_{\text{eff}}M(v_{b0} - v_{M0})}{M + m}. \tag{2.22}$$

With all these discussed above, equations to describe the dynamics of the impact-driven harvester can be established [89]: $M\mathrm{d}_2\delta M/\mathrm{d}t^2 + D_v\mathrm{d}\delta_M/\mathrm{d}t = F_{\text{ext}}$, where D_v is a viscous damping factor, δ_M is the position of the mass with respect to that of the piezoelectric bender (δ_M is assumed to be one-dimensional), and F_{ext} is the apparent force due to the motion of the frame. The behavior of the whole system can be presented by coupling the two network models of the bimorph with the impact representation consisting of the velocities at the moment of collision.

By having specific types of load circuitry and input forces, the power delivered to the load can be analyzed and optimized [89]. Because the equations of motion are transcendental, it is not possible to develop an analytical model to represent the exact behavior of the human motion harvesters. However, to have a reference for

device fabrication, it is still necessary to conduct theoretical analysis with simplified situations. To do so, a single-impact approximation has been used, in which the sliding object hits one of the benders and but does not interact with it thereafter. That is, the piezoelectric beam oscillates freely without perturbation after the impact. It is assumed that there is only a purely resistive load. With this impact, it seems that an initial quantity of mechanical energy has been applied to the cantilever, which is $E_o = 1/2mv_{b0}{}'^2$. If there is no energy loss, the average output power of the harvester per impulse can be given by $P = E_o/T$, with T being the time interval between two consecutive impacts. The piezoelectric cantilever should be designed in such a way that its output power is as close to this theoretical limit as possible.

One way to increase the electromechanical energy conversion is to maximize the value of the generalized electromechanical coupling factor (GEMC) K^2 [89]. The GEMC can be expressed in terms of the circuit parameters as $K^2 = \Gamma^2/(kC_p)$, which is the equivalent for a piezoelectric bending structure, with the effective electromechanical coupling (EMC) to be $k_{31}^2/\left(1 - k_{31}^2\right)$, for a suspended and axial piezoelectric transducer, with $k_{31}^2 = d_{31}^2 s_{11}^E/\varepsilon_{33}^T$.

To the first approximation, the optimum value of the GEMC is directly proportional to k_{31}^2, which can be obtained by implementing a specific ratio of the thickness of the elastic to that of the piezoelectric layers. This thickness ratio depends on the ratio of the compliances between the two layers. With these parameters, the optimum thickness ratio and the optimum value of K^2 normalized to k_{31}^2 can be expressed as a function of the compliance ratio. The maximum values of the GEMC that can be obtained with state-of-the-art piezoelectric and elastic materials are between 0.1 and 0.3. The value of the GEMC is not affected no matter whether the piezoelectric capacitors in the bimorph are connected in parallel or series.

In addition, the mechanical quality factor Q has to be maximized, so that the maximum amount of the vibration energy initially applied to the beam is harvested by the device and not dissipated otherwise. An approximate expression for the optimum resistive load R_{opt} is given as follows, where $\omega_0 = (k/m)^{1/2}$ is the fundamental frequency of the short-circuited piezoelectric bender.

$$R_{\text{opt}} = \frac{1}{\omega_0 C_P\left(1 + \frac{K^2}{2}\right)}. \tag{2.23}$$

This equation is similar to Eq. (2.10), but with somehow simplification. Although these results are derived from a simplified situation; the conclusions are applicable to most representative cases. Although the real behavior of the device is very complicated, it is assumed that the conditions of maximum GEMC and Q for optimum power derived in the case of single impact are also applicable to the cases of multiple impacts. The parameters, k, Γ, C_p and Q, are 1,000 N m^{-1}, 0.5 m N V^{-1}, 3 nF and 50, so there is $K^2 = 0.08$. Additionally, the dissipations of the sliding object (D_v) must be minimized due to the negative influence on the output power of the device.

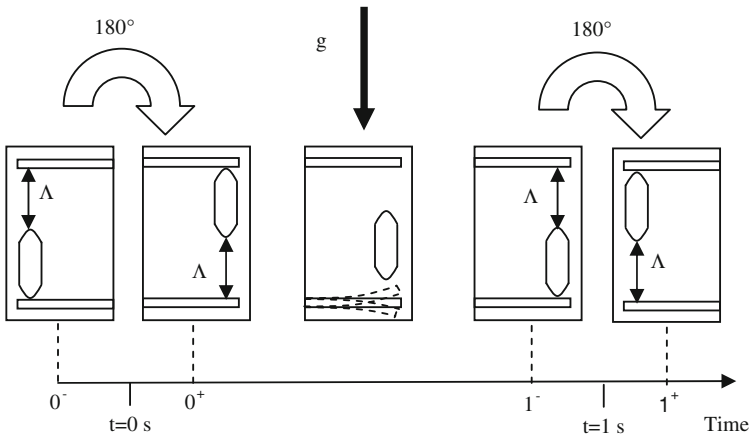

Fig. 2.30 Assumed motion of the harvester for the numerical simulations. Courtesy of M. Renaud, Interuniversity Microelectronics Center (IMEC). Reproduced with permission from [89]. Copyright @ 2009, IoP Publishing

Figure 2.30 shows the assumed motion of the frame for the numerical analysis, which is a quasi-instantaneous 180° rotation per second [89]. Between every two rotations, the frame is supposed to be oriented in such a way that the sliding channel is aligned with the gravity field g, so the missile experiences a gravitational force $F_{\text{ext}} = -Mg$, which makes it move from one cantilever to the other, with the action of gravity on the beams being neglected. There are a lot of such body motions in human daily activity.

Simulation results indicate that the performance of the harvester has a slight decrease with increasing traveling distance Λ of the sliding object. This is because longer traveling distance means longer traveling time required. For example, if the object cannot reach its rest position on the second cantilever before the second rotation starts, the potential energy of the mass will not be totally transferred to the piezoelectric cantilever. As a result, the efficiency of the energy conversion is reduced. This does not necessarily mean a lower output power but in any case a lower output power per unit volume. A constant value $\Lambda = 15$ mm has been used for further analysis.

It is also found that when the natural frequency of the piezoelectric beam is much higher than that of the rotations of the frame, the performance of the harvester in dependent only on the mass ratio M/m, being irrelevant to their individual values. The electrical load used for analysis should be a simple circuit consisting of only a pure resistor. The use of two cantilevers makes the system complicated. For example, if the piezoelectric benders are connected to the same load circuit, they can be arranged in either parallel or series. In this case, when one of the cantilevers is excited, part of the electrical energy it harvests flows toward the second cantilever, rather than toward the load. This inevitably reduces the conversion efficiency. This problem can only be addressed by design, for example,

the use of appropriate switching. For simplicity in analysis, each cantilever is connected to its own load. It is also usually assumed that the sliding object is at rest on one of the cantilevers before every rotation, the power generated by the harvester solely can be estimated by studying the behavior of the system between two successive rotations [89].

In practice, every real impact is followed by a certain number of collisions that are separated by short-time intervals, until the sliding object is ejected from the neighborhood of the cantilever. At this moment, the beam oscillates freely till a second real impact occurs. Depending on the values of the different parameters, the sliding object might apparently "stick" to the cantilever for a short duration. If it is a perfectly inelastic case ($e_{\text{eff}} = 0$), the sliding object and the beam merge into a single oscillator just after the impact and they then separate when the acceleration of the beam becomes zero. For nonzero values of the coefficient of restitution, it is difficult to predict the details of the impact, because they are dependent on different characteristic parameters. However, when the effective mass of the cantilever is negligible as compared with that of the sliding object, the behavior is very similar to the inelastic one, which is independent of the value of the coefficient of restitution.

It is important to estimate the maximum value $\delta_{\max}$, of the deflection of the cantilevers, because too large displacements lead to failure of the device. The upper and lower limits of $\delta_{\max}$ can be estimated according to energy conservation principles. The upper limit of $\delta_{\max}$ is obtained when the impact is perfectly elastic ($e_{\text{eff}} = 1$), while its lower limit can be derived from inelastic impact. By equating the kinetic energy of the sliding object and the beam just after an inelastic or elastic impact to the elastic energy of the cantilever when it has reached its maximum deflection $\delta_{\max}$, an inequality can be obtained in Eq. (2.24), noting that the electrical energy in the piezoelectric beam is neglected [89]. Therefore, the maximum deflection increases proportionally with the impact velocity and the inverse of the open circuited resonance frequency of the cantilevers. Also, the larger the mass of the sliding object, the larger the $\delta_{\max}$ is. Equation (2.24) also indicates that when *M/m* is very large, the upper and lower limits of $\delta_{\max}$ become the same value, i.e., there is no difference between elastic and inelastic impact.

$$\frac{U_0}{\omega_0}\sqrt{\frac{M}{m_{\text{eff}}}\left(1-\frac{m_{\text{eff}}}{m_{\text{eff}}+M}\right)} \le \delta_{\max} \le \frac{U_0}{\omega_0}\sqrt{\frac{M}{m_{\text{eff}}}}. \tag{2.24}$$

The open circuit voltage of the piezoelectric beam as a function of time has been developed on the electrical ports [89]. Every first real impact is characterized by a sharp peak of voltage followed by decaying sinusoidal oscillations. The open circuit voltage V can be related to the deflection δ by $V/\delta = \Gamma/C_p$, if an open circuit and mechanically unconstrained situation are present. In this case, the voltage is directly proportional to the magnitude of the deflection, so a maximum voltage $V_{\max}$ corresponds to a maximum deflection δ and thus the value of $V_{\max}$ can be can be estimated by using Eq. (2.24).

The effects of M/m, e_{eff} and R_L on the efficiency of the energy conversion have also been studied [89]. The initial energy E_0 in the system at the beginning of a cycle can be estimated by the potential energy of the sliding object $E_0 = Mg\Lambda$, with $g = 9.8$ m s^{-2} and $\Lambda = 15$ mm. The energy E_L dissipated in the load resistor during a period of the motion is obtained by integrating $V(t)^2/R_L$. The efficiency η is defined as E_L/E_0 and the average output power P is equal to $\eta E_0/T_i (T_i = 1$ s). With these parameters, waveform of the voltage and the energy dissipated in the resistive load can be well simulated.

The analytical expression of the optimum load resistor for the single-impact approximation has been evaluated for the validation in multiple-impact situations. For such a purpose, the power conversion efficiency η has been systematically studied, with various values of coefficient of restitution and mass ratio, at a constant load resistor. It is found that the effect of the coefficient of restitution on the value of the optimum load is not noticeable, whereas that of the mass ratio M/m is very significant. This important observation has been explained by considering the characteristics of the behavior of the cantilevers. The efficiency does not vary monotonically with M/m [89].

In summary, the efficiency of the energy harvester from human body motion can be optimized by maximizing the GEMC, minimizing the parasitic losses, selecting an appropriate load and using an appropriate mass ratio. In such a way, an optimum efficiency of 40–50 % has been predicted.

The value of the coefficient of restitution e_{eff} has been obtained by measuring the velocity of a steel sliding object before and after impact by using a laser detection method. The excited piezoelectric beam is clamped, so there is no need to measure the velocity of the cantilever. The sliding object is dropped from a height of 15 mm onto the surface of the clamped piezoelectric cantilever. A laser beam coupled to a light detector is used to detect the successive times t_1 and t_2 at which the moving object crosses and exits the beam. From the basic law of motion $L_M = g(t_2 - t_1)/2 + v_1(t_2 - t_1)$, and, as t_1 and t_2 are measured, v_1 can be derived, which is the velocity at time t_1. The velocity v_2 at time t_2 can be obtained from $v_2 = v_1 + g(t_2 - t_1)$ with $v_1 = L_M/(t_2 - t_1) - g(t_2 - t_1)/2$. The impact time t_3 is determined according to the surface wave created at the moment of the collision, which leads to a voltage across the open circuit piezoelectric laminate. The distance between the laser beam and the piezoelectric cantilever L_L is chosen just to be a bit larger than L_M. In this way, the dissipations due to air damping can be neglected in this portion of the motion of the sliding object, and its velocity just before impact v_3 can be approximated by $v_2 + g(t_3 - t_2)$. Similarly, the velocity just after impact, v_3', can be estimated from the time interval between the impact and t_4, so $v_3' = (L_L - L_M)/(t_4 - t_3) - g(t_4 - t_3)/2$. If the impact of a sliding object is on a clamped beam ($v_{b0} = v_{b0'} = 0$ and $m \gg M$), there is $e_{\text{eff}} = -v_3'/v_3$, which mean that the energetic coefficient of restitution is equivalent to the kinematic one. In addition, the angle of drop of the sliding object also has effect on the measured values of e_{eff}, with a standard deviation of 5 %. The average coefficient of restitution is 0.55.

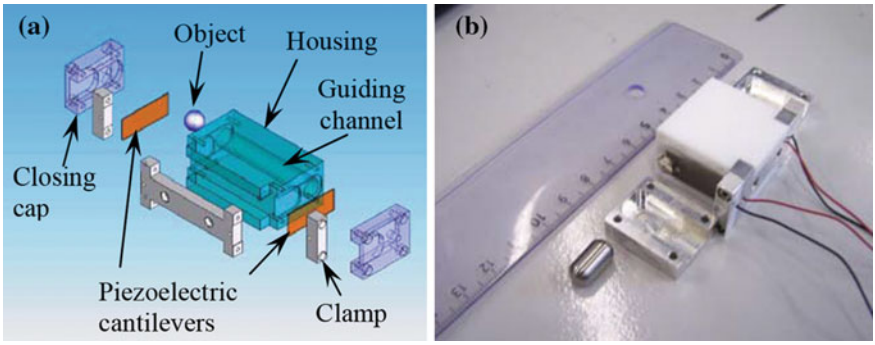

Fig. 2.31 **a** Conceptual representation of the harvester prototype. **b** Photograph of the actual prototype. Courtesy of M. Renaud, Interuniversity Microelectronics Center (IMEC). Reproduced with permission from [89]. Copyright @ 2009, IoP Publishing

The voltage predicted theoretically across the electrodes of the piezoelectric beam and the power dissipated in the load resistor has been compared with experimental measurements. The equivalent network parameters of the piezoelectric beam used in the experiments are: $k = 980$ N m^{-1}, $m = 460$ mg, $M = 4$ g, $Q = 50$, $\Gamma = 0.5$ mN V^{-1}, and $C_p = 3.1$ nF, which lead to $K^2 = 0.08$. They are determined from the analysis of the frequency dependence of the impedance. Experimental results indicate that, with a drop distance of 15 mm, $R^m_{\text{opt}} \approx 400$ kΩ $\approx 2/\omega_0 C_p$, corresponding to $e_{\text{eff}} = 0.5$ and $M/m = 10$, the predicted efficiency is about 50 % higher than the measured one, which has been attributed to the losses occurring during the motion of the sliding object. These losses have been neglected in the numerical simulation. To include these losses in the model, a viscous damping term D_v in the motion of the sliding object should be introduced.

A drawing and photograph of a prototype of the impact-driven energy harvester are shown in Fig. 2.31a and b [89]. The frame of the device is made of Teflon, while Al is used for the clamps and the closing caps. The sliding object is made of steel ($M = 4$ g) with an oblong shape, so that it occupies approximately half of the length of the guiding channel, 30 mm. The electronics to be powered are built inside the frame, so as to have a high output power per unit volume or mass. The characteristics of the equivalent network are: $k = 6{,}000$ N m^{-1}, $m = 600$ mg, $Q = 40$, $\Gamma = 1$ mN V^{-1}, and $C_p = 9.6$ nF, $e_{\text{eff}} = 0.55$, corresponding to $K^2 = 1.7 \times 10^{-2}$.

The kinetic energy of the mass when hitting one of the cantilevers is equal to $Mg = 593$ μJ. Due to the low value of the GEMC, the maximum theoretical value of the efficiency is reduced to 13 % instead of 40 %. The measured maximum efficiency is 8 %. The discrepancy between the predictions and the measurements is slightly lower, which can be attributed to the fact that the sliding object is fully guided so that the losses are reduced.

The device is tested when it is shaken in a hand, as shown in Fig. 2.32a. The output power of the device, as a function of the load resistance, is demonstrated in

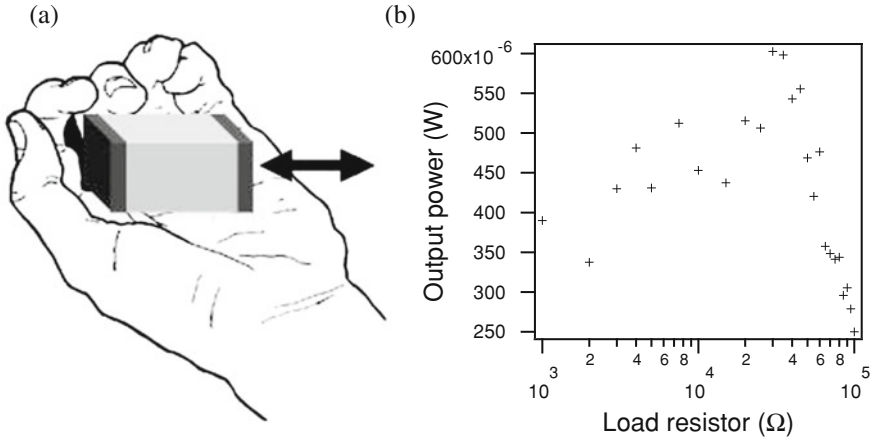

Fig. 2.32 **a** Illustration of the motion applied to the impact energy harvester. **b** Measured output power. Courtesy of M. Renaud, Interuniversity Microelectronics Center (IMEC). Reproduced with permission from [89]. Copyright @ 2009, IoP Publishing

Fig. 2.32b. The frequency of the motion is about 10 Hz, while the amplitude is about 10 cm. A maximum of 600 μW can be achieved. As the resistor is ranging from 3 to 60 kΩ, the average power is up to 400 μW. This amount of power is sufficient to supply energy to simple sensor nodes [89].

There are still rooms to improve the power density of the device, for example, reducing the volume of the device, decreasing its weight, optimizing the performance of the piezoelectric cantilevers, increasing the frequency of the motion and circuit designing [89]. A power density of 10 μW cm^{-3} or 4 μW g^{-1} is expectable for such an impact-driven harvester in human motion energy harvesting applications.

The second example of impact-driven piezoelectric energy harvester from human motion represents the latest development of the type of energy harvesting devices [90]. It uses high-frequency PZT-5A bimorph cantilever beam with attached proof mass at the free end. An aluminum prototype, with a dimension of $90 \times 40 \times 24$ mm^3, has been designed for attaching to human leg to harvest energy produced by waling. An open circuit voltage of 2.47 V and maximum average power of 51 μW can be achieved across a 20 kΩ external load resistance at walking speed of 5 km h^{-1}.

Figure 2.33 shows schematic drawing of the impact-driven energy harvester [90]. It consists of a ridged cylinder, which can slide freely on a shaft and a PZT bimorph, with a tip that can be fixed in parallel with the cylinder. When the cylinder is excited by external impacts, the ridge on it hits the tip and the PZT bimorph vibrates at its resonant frequency after they separate. As the PZT bimorph vibrates, the stored mechanical energy is converted into electrical energy, which is thus transferred to external circuits. The asymmetric design of the tip is to increase the vertical impulse force when the cylinder moves backwards. The parallel layout

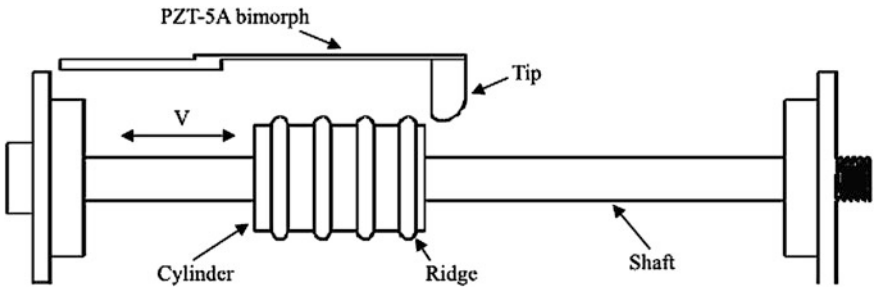

Fig. 2.33 Schematic drawing of the impact-driven piezoelectric energy harvester. Reproduced with permission from [90]. Copyright @ 2013, IoP Publishing

of the piezoelectric cantilever beam and the sliding mass take the unused space so as to achieve high power density. Numerous ridges on the cylinder ensure a repetition of the impact actions to achieve sustained output power. The suitable overlap between the ridge and the tip restricts the impulse force to prevent the PZT bimorphs from damaging.

Figure 2.34a shows a general piezoelectric cantilever beam structure of bimorph, where the attached proof mass on the free end of the beam is used to reduce the resonant frequency [90]. In this configuration, the piezoelectric layer is excited in a bending mode, e.g., d_{31} mode. When the cantilever bean is excited at its resonant frequency, maximum deflection is observed and an electric field is built up between the upper and the lower electrodes.

An analytical model has been established to predict the response of the piezoelectric beam. Because it is a vibration-based energy harvester, lumped parameter models can be used, as shown in Fig. 2.34b. In this approach, the electromechanical properties of the device can be simply modeled as a spring, mass, damper and a piezoelectric element, as discussed earlier. The energy in the piezoelectric layers is measured by using an external resistive load R.

A coupled piezoelectric-circuit finite element method has been used to predict optimized load resistance, as well as amplitude of displacement and resonant frequency of the piezoelectric beam. The PZT bimorph is a 0.13 mm thickness brass shim sandwiched by two piezoelectric layers, with each having a thickness of 0.19 mm. Its overall dimension is $31.8 \times 6.4 \times 0.51$ mm^3. The open circuit resonant frequency is about 260 Hz in modal simulation, which is a reference for further simulation and experiments. Maximum output power is observed as the electrical load is 30 kΩ.

Components used to assemble the impact vibration harvester prototype are shown in Fig. 2.35a, including a PZT bimorph, a cylinder with four ridges, and the tip and the shaft. An aluminum rectangle frame is used encapsulate the PZT bimorph and the sliding cylinder. The structure has a through hole to support the smooth shaft, on which the cylinder can move freely. A piece of rubber is used to protect the harvester, as shown in Fig. 2.35b. The experimental setup to test the

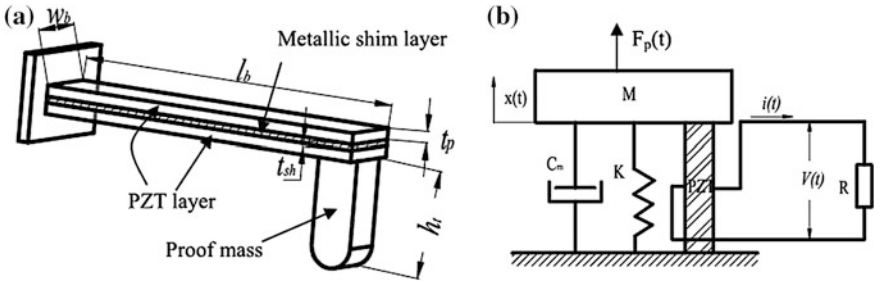

Fig. 2.34 **a** Schematic diagram of a piezoelectric bimorph. **b** General electromechanical model of the piezoelectric vibration energy harvester. Reproduced with permission from [90]. Copyright @ 2013, IoP Publishing

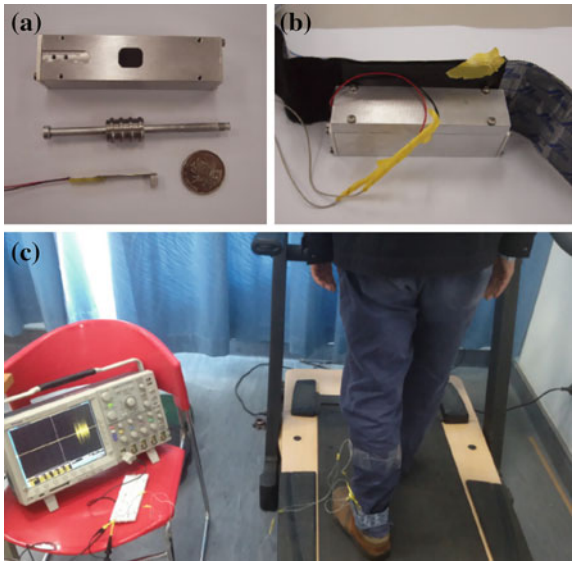

Fig. 2.35 **a** Photograph of components of the harvester, showing the PZT bimorph, shaft, cylinder, cover and frame. **b** An assembled prototype of the harvester. **c** Experimental layout for measuring voltage and power of the harvester, showing an oscilloscope, a circuit board and a treadmill. Reproduced with permission from [90]. Copyright @ 2013, IoP Publishing

impact-driven energy harvester is shown in Fig. 2.35c. The energy harvester is mounted on human leg and the cylinder moves repeatedly along the shaft when the human walks on the treadmill and the ridges in the cylinder impact the tip, so that the PZT bimorph beam vibrates. The output voltage is measured by using the oscilloscope.

The performance of the harvester prototype has been tested at four walking speeds, 3.5, 4.0, 4.5, and 5.0 km h^{-1}. The actual measured resonance frequency of the PZT bimorph with 30 kΩ electric load is 265.5 Hz, very close to the value predicted by the simulation. The output voltage of the harvester is proportional to the magnitude of the deflection of the piezoelectric bimorphs and the impulse force increases with increasing walking speed. Therefore, the peak amplitude of voltage

increases with increasing walking speed. A maximum of 51 μW is observed at walking speed of 5 km h^{-1}. Further improvement in performance of the impact-driven piezoelectric harvester is expectable through materials and design optimization.

2.4.3 Energy from Joint Motion

Piezoelectric harvesters have been designed and fabricated for energy harvesting from joint motion of human body, including knee-joint [91–94] and elbow joint and finger [94]. PZT piezoelectric bimorph is used in the former case, while PVDF sheet is used in the latter case. The PZT bimorph is excited to vibrate with the frequency up-conversion technique. The PVDF device works due to the bending and releasing process of the polymer piezoelectric sheet. Both can be used for wearable applications.

2.4.3.1 Rotary Knee-Joint Harvester

Figure 2.36 shows schematic diagram of the mechanical plucking process, constituting of a sequence of phases [91]. In the approach phase, the distance between bimorph and plectrum is reduced until they come into contact. At the point they contact, the loading phase is immediately started, during which both elastic elements are deflected, according to their mechanical compliances. With their further deflection, the overlap between the two items is reduced, i.e., their contact area becomes smaller and smaller. A maximum deflection is reached when the contact is just lost and the two items are free to return to their un-deformed states, which is the releasing point. At this instant, the bimorph starts to vibrate at its resonance frequency as a cantilever beam. As the bimorph vibrates, the stored mechanical energy is converted through the direct piezoelectric effect into electrical energy, which is then transferred to the external circuit. Part of the mechanical energy is dissipated through various forms of damping, such as air damping, dielectric losses and material internal damping. The outcome of the plucking is frequency up-conversion, because a large number of vibrations are created at high frequency by one single slow movement of the plectrum.

Figure 2.37 shows a knee-joint harvester that can apple repeat plucking actions to achieve continuous power harvesting during the motion of walking or running [91]. During normal gait, the knee alternatively bends and extends nearly once per second, covering a rotation angle of approximately 70°. The outer ring that carries the plectra is fixed to the thigh, while the internal hub that is connected to the bimorphs rotates with the knee as it is fixed to the shank. As the person walks, the knee alternatively extends and bends, each of the multiple plectra on the outer ring plucks the bimorphs in the sequence outlined in Fig. 2.36. This is the principle why the harvester is able to harvest the energy due to the slow motion of walking.

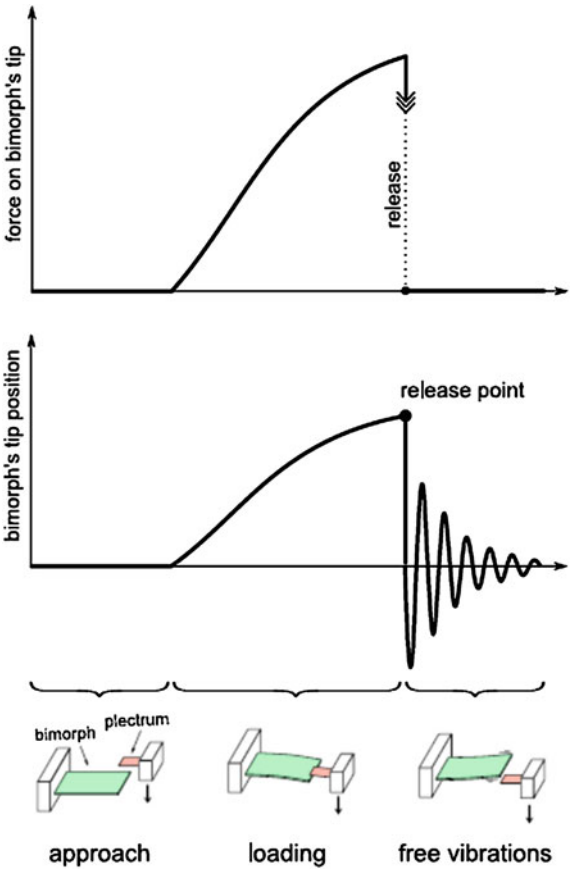

Fig. 2.36 Illustration of the plucking action: during approach, the force on the bimorph is zero, force increases during loading, where mechanical energy is input in the bimorph (and the plectrum), after release, the external force on the bimorph is limited to air damping and to its constraints (mounting) and the device can vibrate unhindered. Courtesy of Dr. M. Pozzi, Newcastle University. Reproduced with permission from [91]. Copyright @ 2011, IoP Publishing

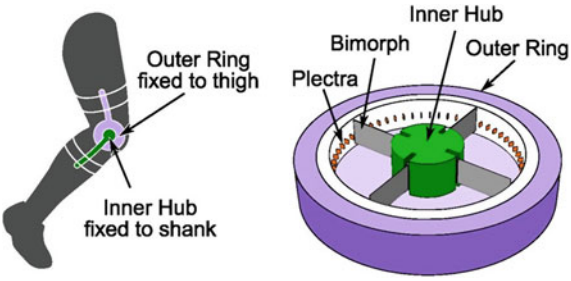

Fig. 2.37 Knee-joint piezoelectric harvester. It is worn on the external side of the knee and fixed by braces. Inside, a hub carries a number of bimorphs which are plucked by the ring-mounted plectra as the joint rotates during walking. Courtesy of Dr. M. Pozzi, Newcastle University. Reproduced with permission from [90]. Copyright @ 2011, IoP Publishing

Finite element (FE) modelling has been employed to analyze the harvester [91]. The power output is calculated from the voltage difference between the two electrodes, i.e., the voltage across the resistor. The boundary conditions include

displacement constraints on the top and bottom surfaces in the clamped portion of the beam. The device this is modelled is a series bimorph with an internal brass shim and two sheets of PZT on either side, covering the entire surface, with given geometry and material properties. The geometry of the bimorph is determined by the acceptable dimensions of the overall harvester.

The model includes viscous damping with the damping matrix C, given by:

$$C = \beta_{\text{PZT}} K_{\text{PZT}} + \beta_{\text{Brass}} K_{\text{Brass}}, \tag{2.25}$$

where, β is stiffness matrix multiplier, K is portion of structure stiffness matrix. The β parameters are calculated from the tabulated mechanical quality factor Q_m and the resonant frequency of the device by:

$$\beta = \frac{1}{\omega Q_m}. \tag{2.26}$$

Two types of analyses are conducted: harmonic and transient. In the harmonic analysis, a sinusoidally varying force of 10 mN is applied at the tip and its frequency is scanned in the neighborhood of the first resonant frequency of the structure. This analysis is similar to the widely used conventional analyses, where the cantilever, with a large mass applied on its tip, is seismically excited by the vibration of its base. The force is not distributed along the cantilever, instead, it is localized on the nodes at the tip. The power output during the harmonic analysis is calculated as root-mean-square power using the amplitude voltage V_0 detected across the resistor R, as shown in Eq. (2.16).

The transient analysis consists of two steps to clarify the effects of different conditions applied for each step without interference of each other. The first is a loading step, where the bimorph is deflected to a predefined tip displacement at constant speed. The second step is the release phase, starting with a stepped removal of the tip constraints of a statically deflected beam. In the transient analyses, the instantaneous power $P(t_i)$ at substep i is calculated from the voltage across the resistor at the same substep, similar to Eq. (2.16):

$$P(t_i) = \frac{V^2(t_i)}{2R}. \tag{2.27}$$

From this equation, the average power $P_{\text{avr.}}$ produced up to the time t_n can be calculated as:

$$P_{\text{avr.}}(t_n) = \frac{1}{t_n} \sum_{i=0}^{n} P(t_i) \Delta t_i \quad (n > 0) \tag{2.28}$$

where Δt_i is the duration of each substep. The average power is of particular interest in the release phase, as it permits to optimize the interval between plucking actions and to predict the ensuing sustained power. Finally, the instantaneous power is also used to calculate the cumulative energy that is produced up to substep n, as a monotonic function of time:

$$E(t_n) = \sum_{i=0}^{n} P(t_i)\Delta t_i. \tag{2.29}$$

Harmonic response measurements with seismic excitations have been conducted to test the performance of the harvester. A Laser Doppler Vibrometer (Polytec CLV-2534) is used to measure the velocity of vibrations. The bimorphis made of PZT-5H that is poled for series operation, with a 130-μm-thick metal shim sandwiched between two layers of PZT, each of thickness of 125 μm. For the harmonic response test, the sample is mounted within copper-clad mechanical fixtures doubling up as pick-off electrodes, leaving a free length of about 22.5 mm. Seismic excitation is created with an acceleration of about 7.1 m s^{-2}. The plucking excitation is produced by loading the bimorph against a plectrum by displacing it over a given distance; release occurs upon retraction of the plectrum, mounted on a linear translation stage. Velocity data are collected with the Polytec LDV. A fixture is use to mount the bimorph test within the copper-clad plates leaving a free length of 26 mm. The plectrum is a 3 × 2 mm^2 rectangle 125 μm-thick Kapton® polyimide film. In both the harmonic and plucking excitation tests, the output of the bimorph is connected to the same circuit, with electrical loads ranging from 25 to 550 kΩ.

The harmonic analysis simulates the normal operating conditions of an environmental energy harvester. The power output curves for the piezoelectric bimorph correspond to maximum voltage amplitudes ranging from 2.7 mV at 300 Hz with 2 Ω up to 24 V at 320 Hz with 1 MΩ electrical load. The largest power output is found with an electrical load of 10 kΩ. As the electrical load increases, we observe a shift in the resonance frequency toward higher values; as is well known, this is due to the stiffening effect produced by the direct piezoelectric effect when the voltage on the electrodes is permitted to build up, which does not happen with lower resistors. The curve corresponding to 20 kΩ is particularly interesting as it has a maximum at frequencies intermediate between open and closed circuit and shows the largest area under the curve (it is lower but broader), indicating that it corresponds to maximum electrical damping, i.e., most efficient power transfer from the piezoelectric bimorph to the resistor, where it is dissipated. With 20 kΩ, a peak voltage amplitude of 6.1 V was detected at about 310 Hz. Meanwhile, the peak amplitude is the minimum in this case.

It has been found that the electrical loads with higher power are also accompanied by larger displacements. This is harmful to the PZT ceramic materials due to the potential failure. It is therefore important to determine the optimized value of the resistor that yields the maximum output power while limiting the strain of the material to a safe level. Therefore, it is necessary to define an appropriate "figure of merit" to figure out the optimal electrical load. This parameter should include both displacement (δ) and the electrical output. Noting that the voltage increases monotonically with increasing load and the power depends on the square of the displacement through the voltage, both V/δ and P/δ are not suitable. To address this problem, the quantity has been proposed:

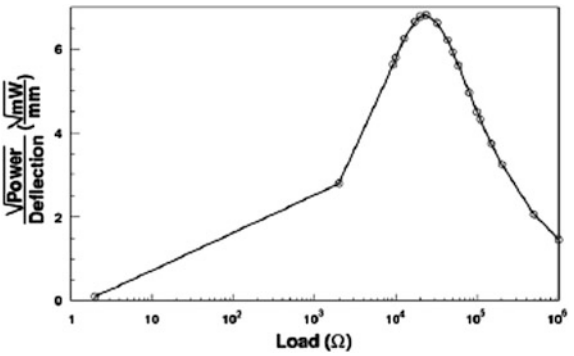

Fig. 2.38 Calculated "figure of merit" as defined in Eq. (2.30) to identify the optimal electrical load of the PZT-5H bimorph under harmonic excitations. Courtesy of Dr. M. Pozzi, Newcastle University. Reproduced with permission from [91]. Copyright @ 2011, IoP Publishing

$$f(R) = \frac{\sqrt{P}}{\delta}. \tag{2.30}$$

The values of "figure of merit" calculated with Eq. (2.30) for the devices are shown in Fig. 2.38 [91]. The best performance is obtained at 311 Hz with $f(R) = 6.8\ (\text{mW})^{1/2}\ \text{mm}^{-1}$ and electrical load of 20 kΩ. It has been found that there is a good agreement between the theoretical modeling and experimental results. Such an agreement is also observed in theoretical predictions of transient analysis (loading step and release step) and experimental measurements of plucking action.

A further study has been carried out to demonstrate the capability of energy harvesting of such harvesters for knee-joint wearable applications, by focusing on the effects of connection of the electrical load and excitation [92]. Two series of measurements are conducted at a speed of 5 s per revolution, as shown in Fig. 2.39. In one series, the bimorph is directly connected to a resistance, whereas in the other, a rectifying bridge is placed between the bimorph and potentiometer. Both curves have a maximum output energy, corresponding to an optimized value of resistance. This occurs when the impedance of the electrical load matches the impedance of the piezoelectric bimorph at the dominant operating frequency.

The optimal electrical load with the presence of a rectifying bridge ($\sim$100 kΩ) is higher than that without the bridge ($\sim$50 kΩ). This is because higher voltages are present across the bimorph electrodes if a higher resistance is connected. Therefore, the fixed forward voltage drop introduced by the diodes in the bridge becomes proportionally less important, i.e., the energy dissipated by the diodes becomes smaller fraction. As a result, when a rectifying bridge is used, higher electrical loads are beneficial and thus the maximum shifts toward higher values of resistance. In addition, when a bridge circuit is used, the amount of total output energy is decreased, with a magnitude of 50–80 μJ, which is due to the dissipation of the diodes in the bridge. Noting that the difference between the two maxima is only about 56 μJ, this loss due to the bridge is readily compensated by the higher electrical load.

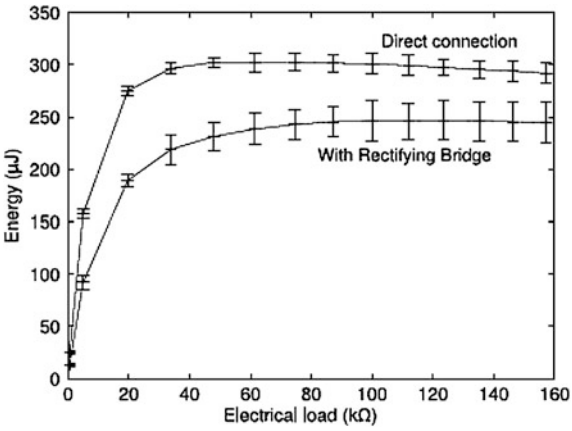

Fig. 2.39 Total energy produced by the bimorph during a full revolution of the outer ring, occurring in 5 s. The plot shows the effect of the resistive load with and without a rectifying bridge. The error bars represent the 90 % confidence level. Courtesy of Dr. M. Pozzi, Newcastle University. Reproduced with permission from [92]. Copyright @ 2012, IoP Publishing

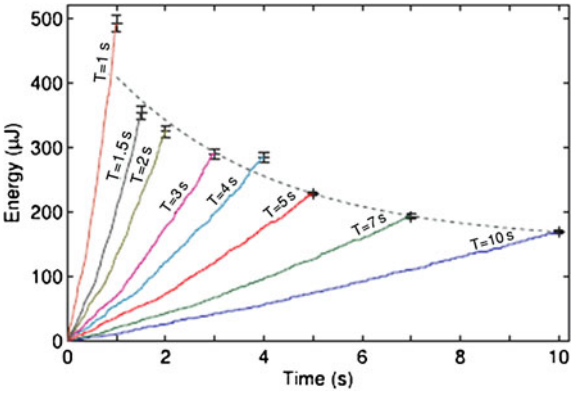

Fig. 2.40 Total energy produced by the bimorph during a full revolution of the outer ring. A 47.6 kΩ resistive load was directly connected to the bimorph. Courtesy of Dr. M. Pozzi, Newcastle University. Reproduced with permission from [92]. Copyright @ 2012, IoP Publishing

It has been reported that during normal gait of human being the angular speed of the knee-joint varies considerably, from 0 up to 6–7 rad s^{-1}. It is therefore important to characterize the harvester over a similarly wide range of angular speed in terms of practical applications. Two groups of measurements have been conducted to check the effect of the rotational speed: one with a directly connected electrical load (Fig. 2.40) and the other with a rectifying bridge interposed (Fig. 2.41) [92].

The results in the two figures indicate that the amount of energy that can be harvested by the harvester increases with increasing walking speed. This is simply because a higher walking speed means a larger total deflection of the bimorph, quicker initial deflection and clearer release, which are all favorable to a high energy output. The trend is likely to be exponential in both cases. This is a reflection of how the three factors combine. For example, larger deflections are observed only at the highest speed, while a quicker initial deflection gives a hyperbolic response.

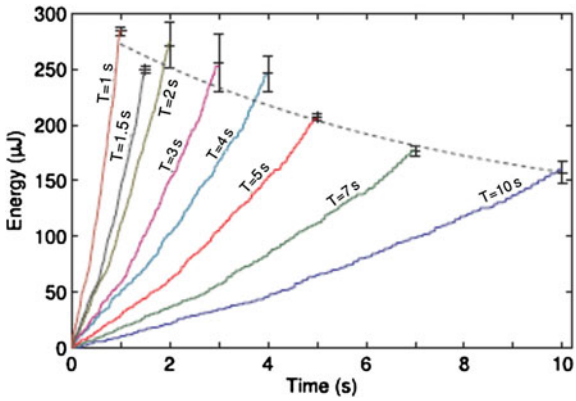

Fig. 2.41 Total energy produced by the bimorph during a full revolution of the outer ring. A rectifying bridge was connected between the bimorph and a 99.1 kΩ resistive load. Courtesy of Dr. M. Pozzi, Newcastle University. Reproduced with permission from [92]. Copyright @ 2012, IoP Publishing

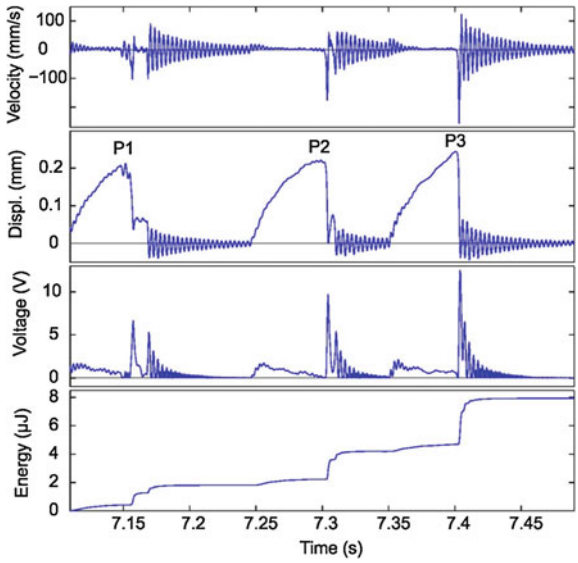

Fig. 2.42 Time domain data for a slow run ($T = 10$ s), from *top* to *bottom*: velocity, displacement (via integration of velocity and after baseline removal), voltage and energy. The first peak is the most common, showing an unclean release, with the plectrum slowly rubbing the bimorph; the second is cleaner and the third is almost ideal and a rare occurrence. Courtesy of Dr. M. Pozzi, Newcastle University. Reproduced with permission from [92]. Copyright @ 2012, IoP Publishing

The process of signal production has been analyzed in detail [92]. Time domain data for a slow run ($T = 10$ s) and fast run ($T = 1$ s) are shown in Figs. 2.42 and 2.43, respectively. Both figures are derived with a rectifying bridge. The displacement traces are extracted from the velocity via time integration, while the energy traces are obtained through time integration of the instantaneous power, calculated as $P(t) = V^2(t)/R$, with $R = 99.1$ kΩ and V is the rectified voltage. Figure 2.42 shows that, when the period is 10 s, all the plucking actions can be clearly identified. For instance, the bimorph is deflected by a plectrum over a time of about 60 ms to the maximum deflection before it is released and quickly returns to the initial state, but with the consequent vibrations about the rest position. The voltage signal already rises during the deflection, although it remains below 2 V in

the 60 ms of the deflection. Much high voltages are produced just after the bimorph is released, with peaks of between 7 and 12 V. The energy curve exhibits a staircase-like character with three major steps, each of which is associated with a plucking action.

Although energy has been generated during the initial deflection, the greatest portion of energy is produced during the first several oscillations after the release. It is found that there are three main types of peaks. The first peak (P1) is characterized by a few of oscillations in the displacement before release and a fragmented step afterwards, implying an unclearn release. As a result, the voltage signal is relatively low and the energy step is small. The second peak (P2) has a cleaner release so that the output voltage is higher. The last peak (P3) is nearly an ideal release, with a sharp rise in displacement before the release point. Therefore, the output voltage and the energy step are both the highest. If the quality of the release is mainly determined by the plectra, there is always a fixed set of plectra that can provide the cleanest peaks.

As shown in Fig. 2.43, high speed ($T = 1$ s) leads to a difficulty in identifying the signals. The first plectrum (P1) causes decaying in the vibrations, due to the presence of a defect in the harvester. The following plectrum (P2) is too short to contact with the bimorph. As a consequence, there is a decaying voltage peak there. Also, the following plectrum (P3) is encountered by a bimorph almost at rest. However, there is still superposition of the fundamental vibration onto the displacement peak caused by the deflection. The next four plectra (P4 → P7) are met at short time intervals, yielding an uninterrupted oscillation of the bimorph, modulated by the contact with the plectra. As a result, the voltage signal shows a rapid succession of peaks with different heights and the energy trace is a wavy line instead of a sequence of steps. The outcome of this continuous vibration of the bimorph is an energy production that is significantly higher than that observed at lower speed.

Three major reasons have been identified to explain why higher energy is produced at faster rotational speeds. The first reason is a faster speed implies a faster initial deflection of the bimorph. The output voltage is proportional to the strain rate during deflection of the bimorph. This phenomenon can be understood from the fact that the energy produced by the harvester is approximately given by:

$$E = \frac{RQ^2}{\Delta t}, \tag{2.31}$$

where Q is the charge generated on the electrodes of the bimorphs, which is assumed to be independent of the strain rate, R is the electrical load and Δt is the deflection time [91]. At $T = 10$ s, the deflection occurs over about 60 ms (Fig. 2.42), at $T = 1$ s, it takes only 5–6 ms (Fig. 2.43). That is to say, a tenfold increase in the speed of revolution implies a tenfold increase in energy generation in the loading phase.

The second factor responsible for the high output energy is the cleanness of the release. As shown in Fig. 2.42, an unclean release, where the time of the contact

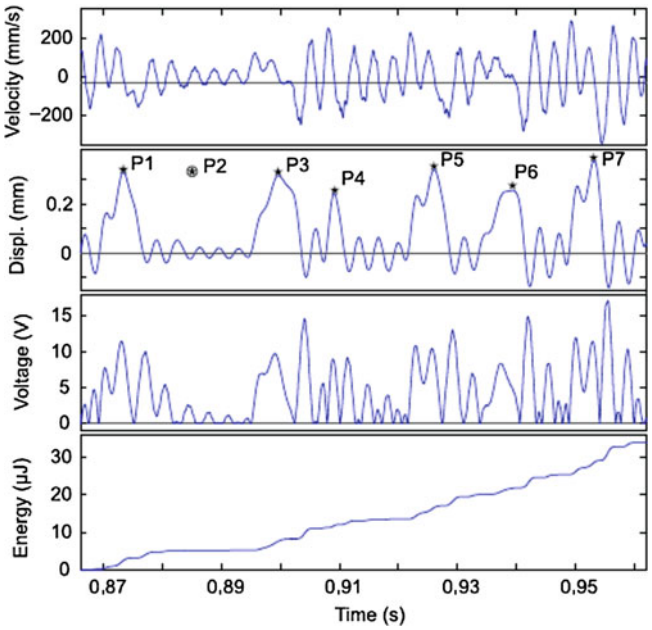

Fig. 2.43 Time domain data for a fast run ($T = 1$ s), from *top* to *bottom*: velocity, displacement (via integration of velocity and after baseline removal), voltage and energy. After the first plucking (*P1*), the bimorph has time to ring down as the immediately following plectrum (*P2*) is too short and does not touch the bimorph; the following plectrum (*P3*) is met by an almost still bimorph; the last peaks (*P3* → *P7*) are almost merged into each other and it can be seen that the bimorph continues to vibrate with considerable amplitude and generate large voltages. Courtesy of Dr. M. Pozzi, Newcastle University. Reproduced with permission from [92]. Copyright @ 2012, IoP Publishing

between the bimorph and the plectrum is too long, the bimorph is almost at the rest position, so that the deflection speed is very low. As a result, there is a lowlevel of energy production. At higher rotational speeds, however, the bimorph is released more quickly and sharply, so that high level of energy production is observed. The last factor is the increase in magnitude of the average maximum displacement, which is only effective at the highest rotational speed. In this case, the continuous encountering of the plectra and the bimorph makes the latter continuously vibrate.

It is also found that the ratio of achievable over measured energy increases with increasing speed, in both cases of with and without a bridge. This means that at higher speeds a larger portion of the measured energy is produced by the better performing plectra. In other words, at high speeds, the quality of the plectra is more important than at low speeds. This is because high quality plectra are less affected than poor performance plectra by speed. The use of a rectifying bridge makes the influence of the quality of the plectra less pronounced, due to the fact that a voltage drop is present.

Noting that the values of the maximum deflections are all well below 0.4 mm, while the displacement suggested by the supplier is 0.51 mm, there is much room to improve performance of the harvester. Other potential aspects include the use of high quality and multiple piezoelectric bimorphs, which is achievable when the PZT components made in laboratories are replaced by large-scale manufactured products.

A field test has been carried out to study the performance of the above mentioned knee-joint piezoelectric energy harvester [93]. Gait cycle data are collected with a marker-based motion capture system and are processed to control a custom-made knee simulator designed to test a piezoelectric energy harvester based on the plucking technique of frequency up-conversion. The performance of the harvester has been assessed by using the gait data collected with the human subject carrying three levels of backpack loads. The harvester can produce an average power of 2.06 ± 0.3 mW, during the normal walking of human being, which is sufficient for useful potential applications.

The harvester has been introduced earlier, which has four bimorphs mounted on the inner hub and 74 plectra mounted on the outer ring. The four PZT bimorphs are referred to as B1, B2, B3 and B4. The prototype harvester has a volume of 226 cm^3 and weight of 235 g. Kinematic data derived from marker-based motion capture systems is an accurate method for the characterization of human biomechanics. A healthy male subject is employed for the test, at a speed self-determined by the subject. A motion-analysis capturing system with six cameras (Qualisys Proreflex MCU240) is used, which captures at a frequency of 100 Hz.

Reflective markers are attached to lower limbs of the subject at the anterior superior iliac spine, posterior superior iliac spine, iliac crest, greater trochanter, fibula head, tibial tubercle, medial condyles, lateral condyles, calcaneus, lateral malleolus, and medial malleolus. The markers form the basis of anatomical reference frames and centers of rotations of the joints. Five rigid plates, each consisting of four noncollinear markers, are also secured on the antero-frontal aspect of the leg, thigh and around the pelvis, as shown in Fig. 2.44 [93]. The calibrated anatomical systems technique (CAST) is used to monitor and record the movement of these segments during the walking trials. The trial is repeated for five times, with three backpack load levels of 0, 12 and 24 kg. The backpack loads are evenly distributed to avoid bias and all of the markers are remained attached to minimize positional inconsistency in re-attachment.

The knee-joint angle displacement can be extracted from the main kinematics dataset. The joint kinematics is calculated by using an X–Y–Z Euler rotation sequence in which the center of the knee-joint is defined as the midpoint between the medial and lateral condyles markers. The angle between the thigh and shank in the sagittal plane is used in the knee-joint simulator, where a naturally standing extension is calibrated to 0° and all higher angular displacements represent flexion. A further extension is possible beyond the natural standing position, but giving negative angles. The angular displacement during the time interval of 0.01 s is averaged over all trials, offering a mean angular displacement sampled at 100 Hz.

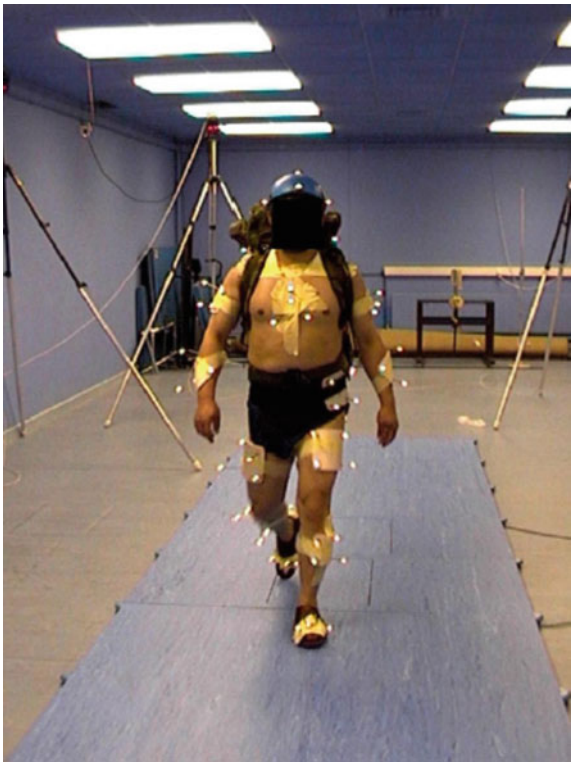

Fig. 2.44 The marker configuration and motion analysis system used for the calibrated anatomical systems technique (CAST). Courtesy of Dr. M. Pozzi, Newcastle University. Reproduced with permission from [93]. Copyright @ 2012, IoP Publishing

Figure 2.45 shows biomechanical data collected from the human subject carrying different levels of backpack loads [93]. It is found that the load indeed has influences on the gait pattern. There are two peaks in all three curves. The first peak, having an angle close to 20°, is attributed to the flexion of the knee-joint immediately following the heel-strike, when the leg is loaded with the weight of the body. The second one, slightly higher than 50°, is ascribed to lift-off, when the leg has left the ground and is carried forward before the next heel-strike. The gait patterns are almost the same for the 0 and 12 kg loads, while the highest load of 24 kg leads to a different gait pattern, with a delay of about 0.1 s, corresponding to a decrease in average step frequency from 0.95 to 0.88 Hz.

Figure 2.46 shows time-domain results of one of the four bimorphs (B4) tested with the kinematic data for the backpack load of 0 kg. In the first 0.5 s of motion, due to the low speed, the frequency of the plucking actions experienced by the bimorph is low, so that the plucking process can be clearly identified. The resonance vibration of the bimorph cannot be distinguished due to the relative high frequency of 300 Hz. The wide peak centered at about 0.4 s is due to the long time plectrum-bimorph contact. It means that plucking is not clear. Two groups of strong and dense peaks are observed in the second half of the gait cycle, with large angles experienced by the knee in short time duration. The appearance of the close peaks results in a continuous bimorph vibration [93].

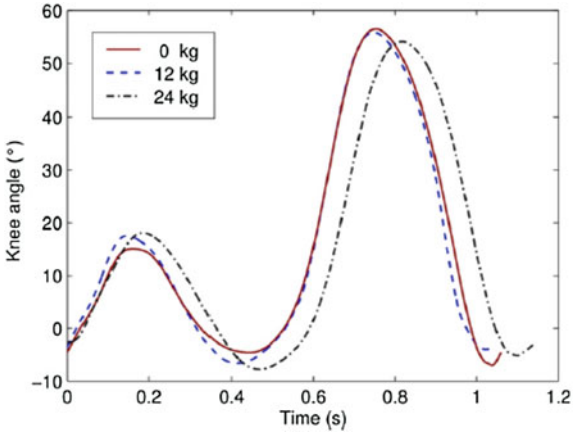

Fig. 2.45 Mean angular displacement covered by the knee-joint of the subject when carrying a selection of backpack loads. Courtesy of Dr. M. Pozzi, Newcastle University. Reproduced with permission from [93]. Copyright @ 2012, IoP Publishing

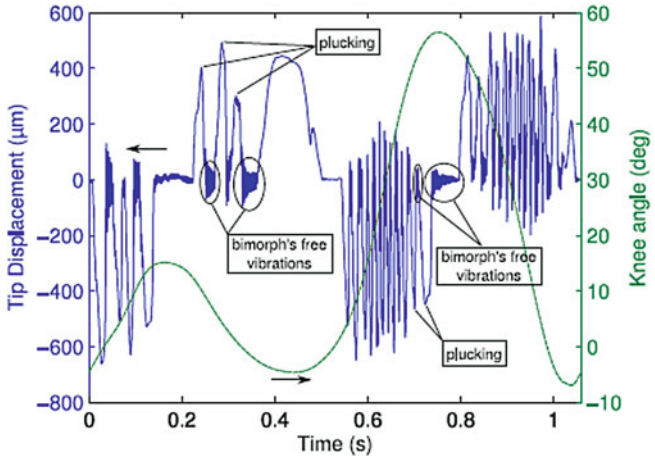

Fig. 2.46 Displacement of the tip of bimorph B4 during the gait cycle with 0 kg load. The angle covered by the knee-joint is also plotted (*dashed line*, *right* ordinate axis). Courtesy of Dr. M. Pozzi, Newcastle University. Reproduced with permission from [93]. Copyright @ 2012, IoP Publishing

The corresponding output power and voltage signals are shown in Fig. 2.47 [93]. In the first half of the gait cycle, the signal peaks are relatively low with large spaces, whereas two groups of dense peaks with much higher magnitude are observed in the second half. There are only two very low voltage peaks, with one in the beginning and the other at the end, for the wide displacement peak at about 0.4 s. This wide peak almost does not produce power, due to the slow deflection of the piezoelectric beams. Therefore, a clear plucking can produce higher power

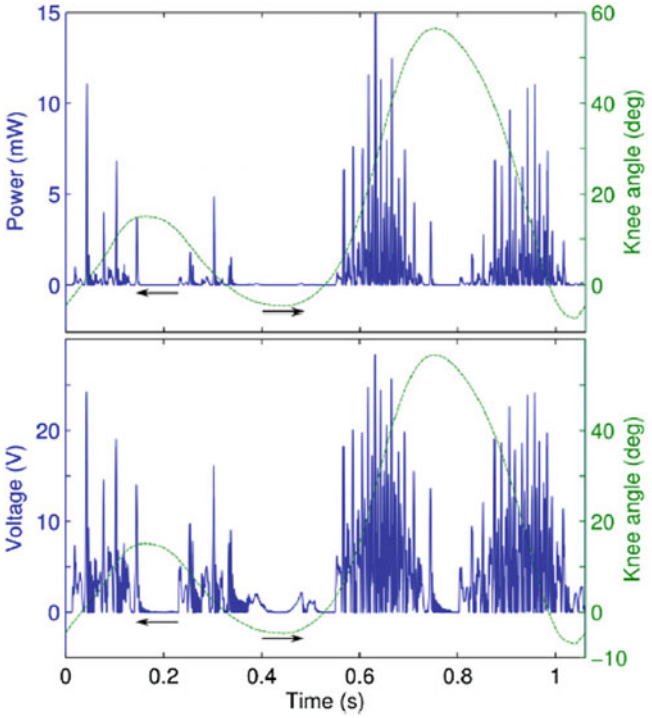

Fig. 2.47 Voltage and instantaneous power detected across a 52.9 kΩ equivalent resistor connected to bimorph B4 as a function of time during the gait cycle with a backpack load of 0 kg. The angle covered by the knee-joint is also plotted (*dashed line*, *right* ordinate axes). Courtesy of Dr. M. Pozzi, Newcastle University. Reproduced with permission from [93]. Copyright @ 2012, IoP Publishing

than a quasi-static deflection of the bimorph, although they may create the same amount of charges in open circuit. The maximum output power and voltage of the harvester are 20 V and 15 mW, respectively.

The energy versus time, E(t), during the gait cycle, calculated from the instantaneous power, P(t), by numerical integration via the trapezoidal method, $E(t) = \int_0^t P(t)\ \mathrm{d}t$, also indicates that the contribution of the first half gait cycle is only less than 20 %. In addition, the quality of the plectra also has a significant effect on the performance of the harvester. It is desired that all plectra have exactly the same dimension and same protrusion, so that they provide uniform and clear plucking to the bimorphs. This can be readily achieved in large-scale industrial production.

The final energy produced by the end of the gait cycle by the bimorphs has been evaluated [93]. In one round of test, three successive runs are performed for each of the three gait cycles, i.e., with three loads of 0, 12, and 24 kg, resulting in nine groups of measurements. In the next round, by reversing the direction of the motion, it is likely that the device is mounted on the other leg or connections to

inner hub-shank and outer ring-thigh are reversed, corresponding another nine set of measurements. The four bimorphs have different energy harvesting capabilities. The energy produced by B3 is about 30 % higher than that by B2 in the first nine runs, while the difference in the amount of energy by B1 and B4 is less than 3 %. After the direction is reverse, bimorph B4 produces 33 % more energy than B3, while B1 and B2 produce the same energy (within 3 %). It means that the amount of energy generated by a bimorph can be different in different directions, implying that the exact shape of the plectra and the angle at which they are mounted have more pronounced effect than the bimorph. However, these effects have been balanced among the four bimorphs, so that the total average energy productions are almost the same in the first and second nine runs of experiments. In other words, the energy generated by the harvester presented here is not affected by the way that the device is mounted.

It is noticed that the gait cycle with the load level of 24 kg yields a slightly lower amount of energy than those of the cases with 0 and 12 kg [93]. According to the total angle, 166, 168, and 170°, for loads of 0, 12, and 24 kg, it would be expected that the gait cycle with the load 24 kg should facilitate more plucking actions and thus generate more energy. This means there is certain reason behind. It is found that the average bending speed of the knee-joint is affected by the level of the load. The average angle speeds are 161, 157, and 149° s^{-1} for 0, 12, and 24 kg, respectively. Therefore, it is further concluded that a high quality of plucking (quick and clear) ensures high energy generation [91, 92]. The average power produced by the bimorph is 2.06 ± 0.3 mW. Therefore, if more bimorphs are used, for example from the current 4 to 16–20, the output power can be over 30 mW.

2.4.3.2 Flexible Wearable Harvester

Different from the harvesters discussed above, in this subsection, a flexible energy harvester with a piezoelectric polymer PVDF in-shell structure that can generate high power from slow human motion [94]. Starting with description of working principle, fabrication and characterization of such flexible energy harvesters will be presented and discussed.

According the piezoelectric effects given by Eq. (2.12), if a linear relation between stress and strain is assumed, the total induced charge can be expressed as:

$$Q = \mathrm{d}YA\frac{\Delta l}{l_0}, \tag{2.32}$$

where Q is the total charge induced in the material, Y is Young's modulus, A is the surface area, and l_0 and Δl are the initial and differential lengths of the piezoelectric material, respectively. The effect of the electric field on the strain has been ignored. The output current and voltage over a resistive load can be obtained by differentiating both sides of Eq. (2.32) as:

$$I = \frac{V}{R_L} = \dot{Q} = \mathrm{d}YA\frac{l}{l_0}\dot{\Delta}\, l, \tag{2.33}$$

where I is the output current, V is the output voltage, and R_L is the load resistance. In addition, the energy generated by the materials in Eq. (2.32) can be expressed as:

$$W = \frac{Q^2}{2C} = \frac{tA}{2\varepsilon}d^2Y^2\left(\frac{\Delta l}{l_0}\right)^2, \tag{2.34}$$

where C is the capacitance of the piezoelectric layer and t is its thickness. Equations (2.33) and (2.34) indicate that a fast deformation of the piezoelectric material is required to have high output current and voltage, as can be found in the previous section. In addition, a large strain is necessary to generate high electrical energy and high output power, which is time derivative of the energy given in Eq. (2.34). Therefore, a pre-stressed shell structure is intentionally used to provide a large strain and fast transition, so as to achieve high output voltage and power.

The shell structure offers a fast transition from the initial state to the bending state, and vise-versa, when it is activated by a bending excitation [95, 96]. The proposed shell structure device consists of a PVDF layer attached to a curved polymer film, as shown in Fig. 2.48a as a concept [94]. In the initial state of the shell structure, no voltage is generated. When the shell structure is subject to a bending force at a threshold point, the film experiences a fast transition from its initial state to a folding state. As such, a tensile stress is applied to the PVDF layer, which thus produces an output voltage. When the structure is stretched, experiences a fast transition back to its initial state, which again leads to and output voltage, but in the opposite direction. With repeated folding and unfolding motion, the shell structure device converts mechanical energy into electrical energy continuously, although the motion might be irregular and slow. Figure 2.48b shows parameters of the shell structure in a cross-sectional view [94]. The curvature of the shell is defined by the following equation:

$$k = \frac{1}{r} \approx \frac{8h}{w^2 + 4h^2}, \tag{2.35}$$

where k is the laminate curvature, r is the radius of curvature, and w and h are the width and center height of the structure, respectively [97]. For a laminated piezoelectric film, as shown in Fig. 2.48c, the strain vector $\{S\}$ can be expressed as:

$$\{S\} = \{S_0\} + z\{k\}, \tag{2.36}$$

where $\{S_0\}$ is the mid-plane strain, $\{k\}$ is the mid-plane curvature and z is the distance variable in the direction perpendicular to the film surface. If the piezoelectric properties are isotropic in the given plane, the electrical displacement of the piezoelectric shell structure can be determined from Eq. (2.12) as:

$$D_{\text{shell}} = d_{31}\{110\}\{S\}. \tag{2.37}$$

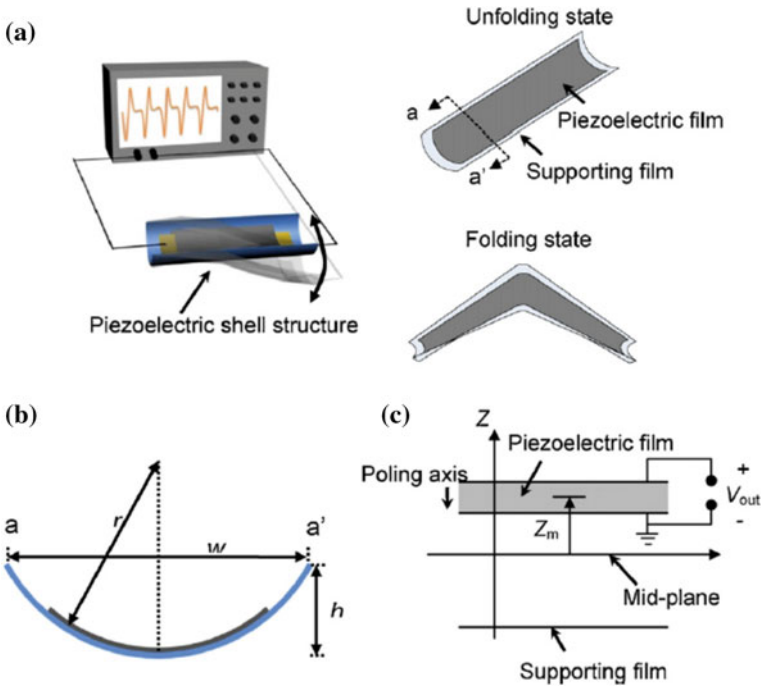

Fig. 2.48 **a** Schematic of the proposed shell structure device depicting the initial unfolding state and folding state. **b** Cross-sectional view of the piezoelectric shell structure. **c** A magnified partial cross section. Reproduced with permission from [94]. Copyright @ 2012, Elsevier

To find the charge induced by the shape transition of the piezoelectric shell structure, it is necessary to have its electrical displacements before and after the transition (Fig. 2.48a) [94]. However, the electrical displacement after the transition is negligible because the curvature in the transverse direction becomes almost flat in the folding state and the curvature in the longitudinal direction is very small as compared to the initial shell curvature. Therefore, the induced charge can be obtained by integrating the electrical displacement given by Eq. (2.37) over the surface deformation during the state transition:

$$Q = \int_{\Omega} D_{\text{shell}} \mathrm{d}\Omega = d_{31}\left(\int_{\Omega} S_0 \mathrm{d}\Omega + z_m \int_{\Omega} \kappa \mathrm{d}\Omega\right), \tag{2.38}$$

where z_m is the distance from the mid-plane of the shell film to the middle point of the piezoelectric layer. The first integral represents the contribution of the average membrane strains over the piezoelectric layer, while the second term stands for the charge generated by the bending of the piezoelectric layer. The above equation shows that the induced charge and consequently the generated energy are proportional to the initial curvature of the shell structure.

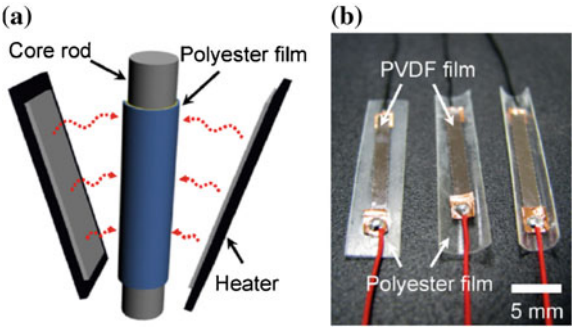

Fig. 2.49 **a** Schematic view of the fabrication method. **b** Photograph of the fabricated prototype devices. Reproduced with permission from [94]. Copyright @ 2012, Elsevier

The prototype shell structure device consists of a polyester film and a PVDF layer. A polyester film has a thickness of 127 μm and a dimension of 30 × 6 mm^2. Further, a thick commercial The PVDF film has a thickness of 110 μm, with metal electrodes on both sides over an area of 20 × 2 mm^2. Figure 2.49a shows a schematic view of the fabrication process [94]. The polyester film is rolled around a metal rod and fixed to the rod with a heatproof tape. It is then heat-treated at 150 °C for 3 min. The curvature of the polyester film is determined by the radius of the core rod. Metal rods with four different radii are used to produce shell structures with four curvatures (κ = 200, 300, 400, and 500 m^{-1}). The strains of the piezoelectric layers calculated with Eq. (2.36) are 2.36, 3.54, 4.72, and 5.90 %, respectively. After that, the PVDF films are attached to the concave surface of the polyester film. In this step, the PVDF film is positioned in such a way that positive voltage is generated on the upper surface when compressive stress is applied, as shown in Fig. 2.48c. Figure 2.49b shows a photograph of the prototype devices with curvatures of 0, 200, and 500 m^{-1}.

For the folding and unfolding experiment, a bending force is applied to the shell structure after it is mounted on a linear actuation system. The actuation system consists of a linear motion stage and step motor, with the moving distance, velocity and acceleration being accurately controlled. During the folding and unfolding process, the open-circuit voltages of the shell structures with different curvatures are measured. In addition, the effect of angular velocities or frequencies of the folding and unfolding operation has been tested, at a maximum bicep curl rate of 2 curls s^{-1} or an angular velocity of around 10 rad s^{-1}.

Experimental results have demonstrated that the shell structure generated much higher output voltage than the flat structure under the same conditions. This is because the shell structure experiences a faster transition between the two states. For the shell structure with a curvature of 500 m^{-1}, with a folding angle of 80° and folding/unfolding frequency of 2 Hz, the output voltages generated is negative during the folding and is positive during the unfolding. This is because the folding and unfolding correspond to tensile and compressive strain in the PVDF film, respectively.

The peak output voltage of the flat structure is always not over 10 V, which has only a very slight increase with angular velocity and the magnitude of displacement. In contrast, the output voltage of all the shell structures was almost linearly proportional to the angular velocity. The maximum output voltage is over 65 V at a folding angle of 80° and a folding and unfolding frequency of 3.3 Hz, when the shell curvature is larger than 300 m^{-1}. In addition, at low folding angles (40° and 60°), the output voltage is slightly dependent on the shell curvature. At high folding angles (80°), there is a critical curvature, 300 m^{-1}, output voltage has no change with increasing curvature.

The relationship between resistive load and output power has been studied to determine the optimal load for maximum output [94]. All measurements are conducted with a folding angle of 80° at a folding and unfolding frequency of 3.3 Hz, corresponding to an angular velocity of 9.3 rad s^{-1}. The optimal load resistance is 90 kΩ for the shell structure with a curvature of 500 m^{-1}. The maximum output power for the single shell structure is 0.87 mW, corresponding to a power density of 2.18 mW cm^{-2}, which is much larger than that of the flat structure (26 μW).

Durability of the shell structure has also been evaluated by measuring the output voltage with repeated folding and unfolding operations. The output voltage gradually decreases to 50 % of its initial value after 50 repeated operations. This degradation has been attributed to the reduction in curvature of the structure and peeling of the metal electrodes from the PVDF film. It is expected that these mechanical problems can be readily addressed by using more sophisticated fabrication technologies. For example, by using reactive metals such as chromium and titanium as an adhesion layer between PVDF and the metal electrode, the adhesion will be improved. High durable substrate materials with better mechanical strength can be used to replace the polyester.

An update version of the shell structure harvester, fabric device, has been developed, as shown in Fig. 2.50. In the fabric device, the piezoelectric shell structures are embedded in textiles. The fabrics are stitched and fitted to human body. The shell structures are inserted into the paths formed by stitching the fabric and the structures are connected in parallel. The fabrics are made in the form of a band for wearing either on elbow joints or on fingers. Three types of shell curvatures, i.e., 0 (flat), 200, and 500 m^{-1} have been tested. The numbers of the PVDF structures embedded in the fabrics are ten and four for the elbow joint and the finger, respectively.

Energy harvesting performances of the fabric devices have been measured. Figure 2.51 shows peak output voltages, as a function of frequency, of the fabrics with different curvatures, worn on elbow joint and finger. The bending angles are fixed at 130° and 70° for the elbow joint and finger motion, respectively. In all cases, the output voltage is proportional to the shell curvature and the bending speed.

The maximum output power generated by using the fabric harvester, made with the shell structures with a curvature of 500 m^{-1}, worn on the elbow, is 0.21 mW, corresponding to a power density of 0.05 mW cm^{-2}, for a resistive load of 90 kΩ

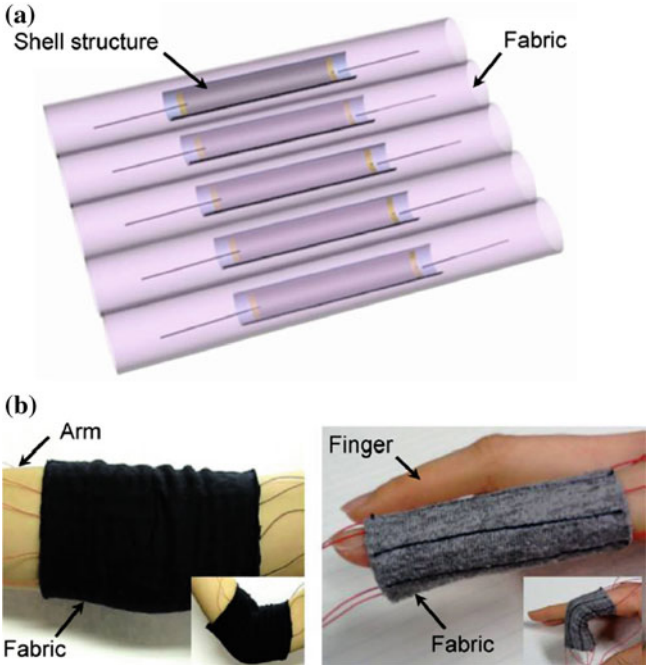

Fig. 2.50 **a** Conceptual view of fabricated fabric embedded with piezoelectric shell structures. **b** Photograph of fabrics worn on the elbow joint and the finger. Reproduced with permission from [94]. Copyright @ 2012, Elsevier

at a bending speed of 5 rad s^{-1}. The output powder is about 40 times that ($\sim$5.4 μW) offered by the fabric with flat piezoelectric structures. In summary, this device has obvious advantages, such as simple fabrication process, low cost and lightweight. It still has potential to further improve its performance.

2.4.4 Rotating Harvesters

2.4.4.1 Structure and Principle

A compact passively self-tuning piezoelectric energy harvester for rotation applications has been developed, which can be related to household activities [98]. The harvester rotates in a vertical plane, consisting of two beams: a relatively rigid piezoelectric generating beam and a narrow flexible driving beam with a tip mass mounted at the end. The mass impacts the generating beam repeatedly due to the influence of gravity. Centrifugal force from the rotation modifies the resonant frequency of the flexible driving beam and the frequency response of the harvester

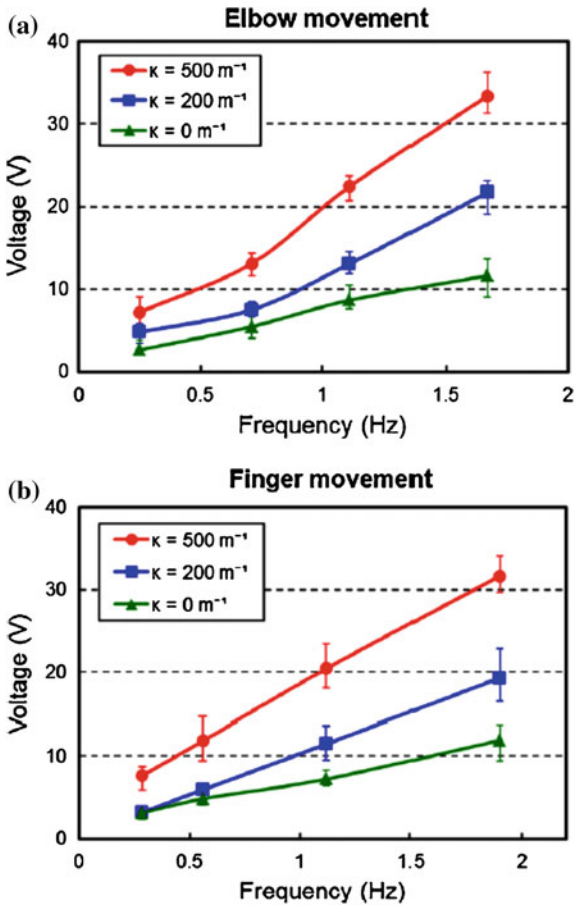

Fig. 2.51 Average output voltage generated when the fabrics are worn on **a** the elbow joint and **b** the finger. Reproduced with permission from [94]. Copyright @ 2012, Elsevier

beam. With an optimized design, resonant frequency of the harvester substantially matches the frequency of the rotation over a wide frequency range from 4 to 16.2 Hz. A prototype of the passive self-tuning energy harvester with a PZT generating beam exhibits a power density of 30.8 μW cm^{-3} and a bandwidth of more than 11 Hz. Passive tuning has also been demonstrated with PVDF as the generating beam.

Figure 2.52 shows schematic diagrams of structure and working principle of the rotatory piezoelectric harvester [98]. The harvester consists of a rigid piezoelectric generating beam located adjacent to a much more flexible driving beam with a steel ball at its tip. The walls of the harvester package can limit the motion of the ball to one direction, as shown in Fig. 2.52a. This ensures that motions have sufficiently large amplitude to apply an impact by the ball to the generating beam, so as to produce electrical output. The resonant frequency of the flexible driving beam is affected by the rotational frequency, thus affecting the natural frequency of harvester. The resonant frequency of the generating beam is almost not affected by

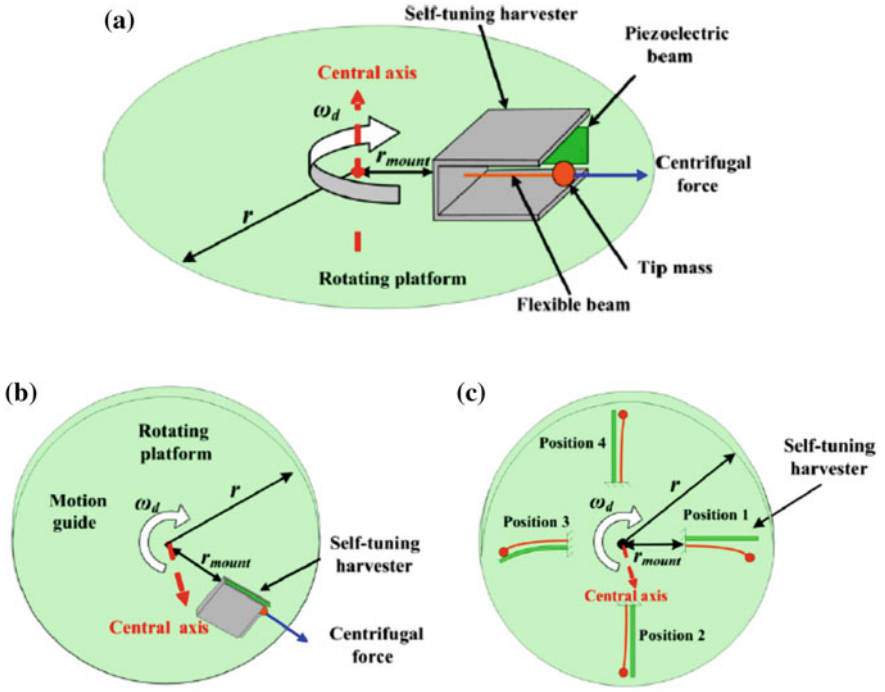

Fig. 2.52 **a** Schematic view of the impact harvester with frequency self-tuning. Although in reality the system rotates in the vertical plane, here it is drawn in the horizontal plane for clarity. **b** Schematic diagram showing the harvester mounted on a vertically rotating wheel. **c** Schematic diagram of the driving and generating beam positions as the wheel rotates through 360°. Beam positions are shown at 90° intervals. Reproduced with permission from [98]. Copyright @ 2012, IoP Publishing

the rotational motion. In operation, the harvester is mounted on a vertically oriented rotating platform such as a wheel or a fan (Fig. 2.52b and c).

When the flexible driving beam is mounted on a frictionless pivot at one end, the system can be described similar by using the conventional equations of a pendulum. However, the flexible driving beam in this harvester is mounted as a conventional cantilever beam, so that the displacement of the tip mass should be described by beam bending. According to classical beam theory, the stiffness of a cantilever beam can be tuned by applying an axial force [98]. Due to the tensioning of the frequency-dependent beam resonant frequency tracks the driving frequency in the rotational harvester. This approach has been used to ensure that the impact-driven harvester is more compact and can work at resonance over a wide frequency range.

For small deflections, the equation of motion for a cantilever beam with an applied centrifugal force f_c is given as by:

$$v''''(x) + \frac{f_c + \rho_d I_d \omega_r^2}{Y_d I_d} v''(x) - \frac{\rho_d A_d \omega_r^2}{Y_d I_d} v(x) = 0, \tag{2.39}$$

where $v(x)$ is the oscillation amplitude of the beam at position x along the beam, Y_d is Young's modulus of the driving beam, I_d is its moment of inertia, ρ_d is its density, A_d is its cross sectional area, and ω_r is the resonant frequency of the cantilever beam. The driving beam has a circular cross-section and its moment of inertia is given by:

$$I_d = \frac{\pi D_d^4}{64}, \tag{2.40}$$

where D_d is the diameter of the driving beam.

The relation between the resonant frequency ω_r of the driving beam and the applied force (centrifugal force) f_c can be established by solving Eq. (2.39) [98]. The centrifugal force is also related to the rotational speed or driving frequency as:

$$f_c = m(r + l_d)\omega_d^2, \tag{2.41}$$

which links the driving frequency to the resonant frequency of the flexible beam. Because the driving beam and the generating beam are separated with a narrow gap, the resonance frequency of the harvester system, ω_{sys}, can be given by:

$$\omega_{\text{sys}} = \frac{2\omega_r \omega_{\text{coup}}}{\omega_r + \omega_{\text{coup}}}, \tag{2.42}$$

where ω_r is the resonance frequency of the driving beam when it vibrates independently. The ω_{coup} is used to describe the time scale of the coupled motion of the driving beam and the generating beam after the generating beam is excited by the tip mass of the driving beam before they are separated.

During the coupled vibration, the tip mass of the driving beam remains in contact with the generating beam, so that they vibrate together. The spring constant of the generating beam is much larger than that of the flexible driving beam. According to Eq. (2.4), the resonant frequency, ω_{coup}, is given by:

$$\omega_{\text{sys}} = \sqrt{\frac{k_g + k_d}{m}}, \tag{2.43}$$

where k_g and k_d are the spring constants of the generating and driving beams, respectively. The effective mass of the generating beam is neglected. When $\omega_{\text{coup}} \gg \omega_r$, the resonant frequency of the harvester system can be approximated to $\omega_{\text{sys}} = 2\omega_r$, according to Eq. (2.42). Therefore, the resonance frequency of the harvester system can be related to the rotational speed of the system, which is the fundamental physics of the self-tuning rotational energy harvester. When the harvester works at its resonant frequency, the maximum open circuit voltage (V_{oc}) is given by:

$$V_{\text{oc}} = -\frac{d_{31} t_p \sigma_s}{\varepsilon}, \tag{2.44}$$

where d_{31} is the piezoelectric coefficient of the materials of the generating beam, t_p is the thickness of the piezoelectric beam, ε is dielectric constant of the piezoelectric layer and σ_s is the average stress on surface of the generating beam, which is express as:

$$\sigma_s = \frac{3 k_g X_0 L_p}{b_p t_p^2}, \tag{2.45}$$

where k_g and X_0 are the spring constant and the deformation of the generating beam during the impact. L_p and b_p are the length and width of the piezoelectric beam. The deformation of the generating beam can be obtained by energy conservation, where the kinetic energy before impact is equal to the potential energy stored in the driving and generating beams at the maximum displacement [99]. Similarly to Eq. (2.27), the average electrical power generated by the harvester and delivered to the external load at resonant frequency can be evaluated by:

$$P_{\text{avr.}} = \frac{R_L}{2(R_S + R_L)^2} V_{\text{oc}}^2 = \frac{R_L}{2(R_S + R_L)^2} \left(\frac{-3 d_{31} k_g X_0 L_p}{\varepsilon b_p t_p} \right)^2, \tag{2.46}$$

where R_L and R_S are the load resistance and the source impedance, respectively. It means that the output power of the harvester is proportional to the square of the magnitude of deflection by the generating beam, which is similar to that observed in a conventional harvester, but in a relatively complicated way. In this rotatory harvester, the deflection of the generating beam is dependent on the gap between the driving and the generating beams and the driving frequency. The gap determines the effective stiffness and therefore the amplitude of motion of the centrifugally tuned driving beam.

2.4.4.2 Parameter Studies

The design parameters have been optimized so that the harvester always works at its resonant frequency, while driving frequency range should be as wide as possible. The overall self-tuning performance of the harvester is determined by the driving beam. Frequency matching has been tested over a frequency range, with the highest drive frequency up to 20 Hz. The driving beam is made of nylon due to its low Young's modulus.

The first parameter is the diameter of the driving beam [98]. The resonant frequency of the harvester system, as a function of rotational frequency, for the flexible beam with various thicknesses (35, 50, 75, 100, and 150 μm), has been calculated. For thin beams (35 and 50 μm), the thickness has no effect on resonant frequency at given rotational frequencies. For thick beams (≥75 μm), the resonant

frequency slightly increases with increasing thickness, because larger-diameter beams have larger zero-tension bending stiffness.

For each beam diameter, there is a specific rotational frequency that perfectly matches the resonant frequency of the harvester system. This frequency increases from 5 Hz for $D_d = 35$ μm to 19 Hz for $D_d = 100$ μm. Such an intersection means that the stiffness of the driving beams consists of two parts: a fixed zero-stiffness term and a frequency-tuned centrifugal tensioning term. This can be used as a guide to design a harvester with the perfectly-matched frequency to be within the frequency range of interest for specific applications. In this respect, it is easier to ensure a perfect matching between the resonant frequency of the harvester and the driving frequency, when using a thinner beam than a thicker beam, because thinner beam has smaller deviation.

The second parameter of interest is the proof mass [98]. It has been shown that the relationship between the resonant and driving frequency is relatively less sensitive to the proof mass. This insensitivity has been attributed to the fact that an increase in mass has two opposite effects. On the one hand, an increase in proof mass leads to an increase in centrifugal force, thus resulting in an increase in the resonant frequency of both the driving beam and the piezoelectric beam. On the other hand, it reduces the contribution of zero-tension to the resonant frequency of the driving beam and the harvester beam. Therefore, a larger proof mass is usually used to increase the displacement of the generating beam and thus the output power of the harvester.

The resonant frequency of the generating beam is also affected by the length of the driving beam (l_d) and the mounting radius (r_{mount}) [98]. The resonant frequency of the harvester, as a function of the rotational frequency, has been simulated, with the l_d varying from 15 to 25 mm, at a given r_{mount} of 5 mm. It is found that the matching between the rotational and resonant frequencies is quite sensitive to l_d, as compared to the driving beam thickness and the proof mass. This implies that the length driving of the driving has its effect through both the zero-tension stiffness and the centrifugal force. For a given harvester, the only parameter that can be changed is the r_{mount}. The simulated resonant frequency of the harvester, as a function of the rotational frequency, indicates that the quality of the frequency matching is very sensitive to the mounted radius r_{mount}. However, the frequency mismatch related to the length of the driving beam can be compensated by adjusting the mounting radius [98].

The last consideration is the optimization of the whole harvester system. With given optimal parameters, the predicted resonant frequencies of the harvester system and driving frequencies match well over a wide frequency range from 6 to 20 Hz with a maximum mismatching of only 0.5 Hz. The resonant frequency of the harvester system is almost the same as the driving frequency at the intersection frequency of 15 Hz, which has been actually treated as the resonant frequency of the self-tuning harvester. The predicted resonant frequencies of the harvester system also match quite well over a wide range of vehicle speed (up to 70 miles per hour (mph)).

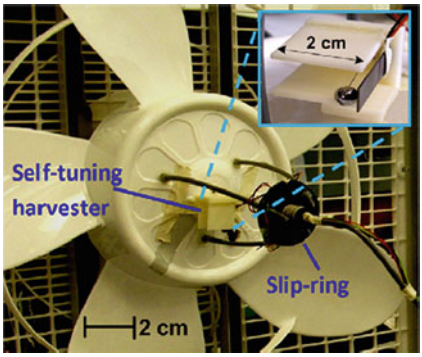

Fig. 2.53 Photograph of test bed with a harvester prototype mounted on an electrical fan. Reproduced with permission from [98]. Copyright @ 2012, IoP Publishing

Besides the advantage of the self-tuning capability, this harvester is able to harvest energy from low frequency sources, due to the frequency up-conversion. The impact vibration process involves two stages. The first stage begins when the driving beam's tip mass impacts the generating beam and thereafter they move together. If the mass of the generating beam is negligible as compared with the tip mass of the driving beam, the process is very similar to an inelastic impact. The second stage starts from the separation of the tip mass and the generating beam. During this stage, the generating beam vibrates alone with an exponentially decaying amplitude at its self-resonant frequency, while the driving beam is driven at the ambient driving frequency. The two stages are repeated at a frequency determined by the periodic rotational motion.

2.4.4.3 Characterization and Performance

Two types of materials, PZT and PVDF, have been used as generating beams of the rotational harvester [98]. Figure 2.53 shows photograph of a prototype of the harvester, which consists of a 0.4 g steel ball as tip mass mounted on a driving beam that is a 2 cm long and 75 μm-diameter nylon cable fixed to a frame holding a separate 25 mm long, 6.4 mm wide and 0.51 mm thick PZT generating beam. The gap between the steel ball and the generating beam is less than 1 mm, so that the amplitude of the ball's motion is larger than the gap. This is to ensure that the impact occurs at least at a driving frequency of up to 16.2 Hz, corresponding to a speed of 65 mph of a typical vehicle wheel. Two ABS plates are placed on the two sides of the driving beam to confine the motion of the steel ball within a path that impacts the generating beam. The harvester is attached to an electrical fan with the driving beam oriented parallel to the fan blade and along the radial direction. The root of the driving beam is offset from the center of the fan. The fan has been retrofitted to enable continuously varying speed and simulate the time-varying rotational motion of a wheel. The wires of the rotating harvester are connected to an optimal static load resistance through a slip-ring. A frequency range from 6.2 to 16.2 Hz is used to imitate the case of rotating tires at speeds ranging from 25 to 65 mph.

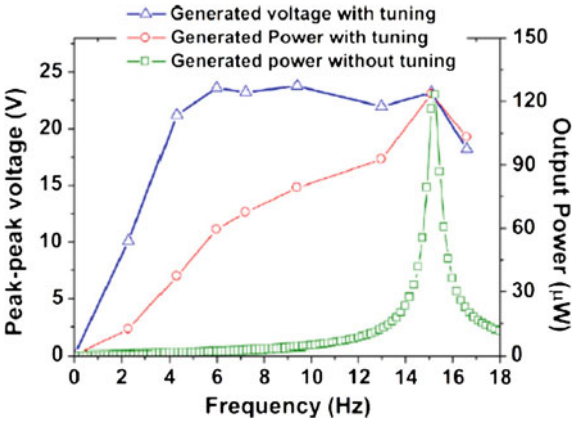

Fig. 2.54 Measured output power and generated voltage of the self-tuning energy harvester plotted versus frequency, along with output power of a comparable untuned harvester. Reproduced with permission from [98]. Copyright @ 2012, IoP Publishing

To evaluate the performance of the harvester, the optimal mounting radius r_{mount} is measured to be 7.5 mm, which is slightly larger than the theoretically predicted optimal radius, due to the effects of damping in the real system. It has been demonstrated that, at the optimal radius, the measured resonant frequency of the harvester matches the driving frequency very well, over a wide frequency range from 4 to 16.2 Hz. The maximum mismatching between the resonant and driving frequencies is less than 0.2 Hz.

Output voltage waveforms of the harvester have been measured with matched load at driving frequencies of 5.96, 9.44 and 15.2 Hz. The impact of the steel ball to the PZT beam has been characterized by the exponentially decayed signals. The observed peak–peak voltages are well within the range of 21.9–23.2 V, as the driving frequency is increased. The response of the harvester to the applied gravitational acceleration is constant over the frequency range. Although the stiffness of the driving beam increases with increasing rotational speed, which leads to decrease in amplitude, the potential energy stored in the driving beam remains constant at resonance. The potential energy transferred to the generating beam due to the impact can be considered to be equal to the maximum potential energy stored in the driving beam, which is responsible for the constant output voltage.

Figure 2.54 shows the output power and voltage of harvester with tuning and output power without tuning. The peak-to-peak voltage remains nearly constant from 4 to 15.2 Hz, indicating that the harvester works at resonance in this frequency range. The output power increases with impact frequency in this frequency range. The drop in the output power at high frequency can be attributed to the increase in the cable tensioning effects. The maximum output power is 123 μW at 15.2 Hz, corresponding to a maximum power density of 30.8 μW cm^{-3}. The self-tuning harvester shows a wider bandwidth 11 Hz as compared with that of the unturned harvester (0.8 Hz).

The optimal load resistance R_L is chosen to match the source resistance R_S, given by:

$$R_S = R_L = \frac{1}{\omega_g C_g} \tag{2.47}$$

where ω_g and C_g are the self-resonant frequency and the capacitance of the generating piezoelectric beam, respectively. Because the generating beam's bending stiffness is dominant over the effects of tensioning, its vibrational frequency remains essentially constant, so that the matched load resistance can be remained constant of 220 kΩ.

The power output of a harvester without tuning can be obtain analytically based on the measured peak output power when the harvester works at resonant frequency and the measured damping ratio. The damping ratio can be calculated from the exponentially decayed waveforms according to the experimental measurement of the resonant frequency of the harvester. The damping ratio ξ is given by:

$$\xi = \frac{1}{2\pi} \ln\left(\frac{p_1}{p_2}\right), \tag{2.48}$$

where p_1 and p_2 are consecutive peak amplitudes. The peak output power of the frequency-matched but harvester without can be considered to be the same as that of the tuned harvester at its resonant frequency. Thus, the semi-empirical plot can be evaluated by:

$$P_{\text{semi-impirical}} = \frac{4P_{\text{peak}}\xi^2(\omega/\omega_n)^2}{[1-(\omega/\omega_n)^2]^2 + (2\xi\omega/\omega_n)^2}, \tag{2.49}$$

where P_{peak} is the output power at resonant frequency, while ω and ω_n are the angular frequency and the resonant frequency of the untuned harvester, respectively.

There is always a potential problem of reliability when using PZT ceramics as active piezoelectric components in a harvester, due to its brittle characteristics. In comparison, PVDF is more flexible than PZT, therefore, the reliability problem is expected to be addressed by using the former to replace the latter. A 16 mm wide, 33 mm long, and 0.2 mm thick PVDF beam has been used as the generating beam in the above discussed self-tuned energy harvester. Since the PVDF beam is very flexible, the optimal mounting radius should be changed from 5 to 15 mm according to modeling results. Figure 2.55 shows measured output voltage and power of the harvester with the PVDF generating beam. With the matched load resistance of 586 kΩ, the PVDF-based harvester exhibits a maximum output power of 27 μW at 15 Hz with a working frequency bandwidth of more than 9.5 Hz. The low output power of the PVDF-based harvester is due to the lower piezoelectric coefficient of PVDF. It is expected that the output power can be further increased by using thicker PVDF beams.

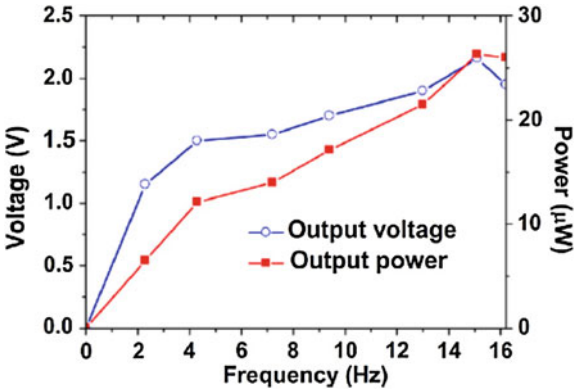

Fig. 2.55 Measured output power and generated voltage plotted versus frequency for a self-tuning energy harvester with a PVDF generating beam. Reproduced with permission from [98]. Copyright @ 2012, IoP Publishing

2.5 Energy from Civil Infrastructure and Transportation

2.5.1 Simulated Study of Bridge

This section is aimed to show the possibility of harvesting energy from civil infrastructure and transportation facilities by using piezoelectric harvesters. The examples are two case studies on bridges [100, 101]. In the first example, piezoelectric effects under various loading conditions on bridges are systematically studied [100]. A steel beam-slab type bridge specimen is fabricated and piezoelectric modules are attached at various positions, where different structural responses are expected under moving vehicles on the bridge. Traffic conditions, including vehicle weight and moving speed, and load conditions, such as load amplitude and loading frequency, have been tested. The performance of the harvester is evaluated by using the generated voltage. The test results are compared with the well-known analytical formulations of piezoelectric effects. It has been shown that the piezoelectric effects are sensitive to the rate of straining and peak strain of the piezoelectric materials, which are determined by the moving speed and weight of moving vehicle on the bridge. The second example is in situ study of a pre-stressed concrete highway bridge, with a piezoelectric cantilever harvester [101]. Although the bridge vibratins are characterized by small amplitude and low frequencies (<15 Hz), the mean output power is in the order of 0.03 mW, with voltages between 1.8 and 3.6 V. The experimental results have been simulated by using theoretical models.

As discussed earlier, when piezoelectric material is attached to a substrate, such as printed circuit board (PCB), the generated voltage of the piezoelectric module is determined by the stress and strain experienced by the piezoelectric material, which can be calculated with analytical formulations taking into account the stress and strain. There have been well-established analytical formulations to estimate the output voltages generated by the piezoelectric modules according to their dimensions, shape, and the attached modules. These analytical formulations

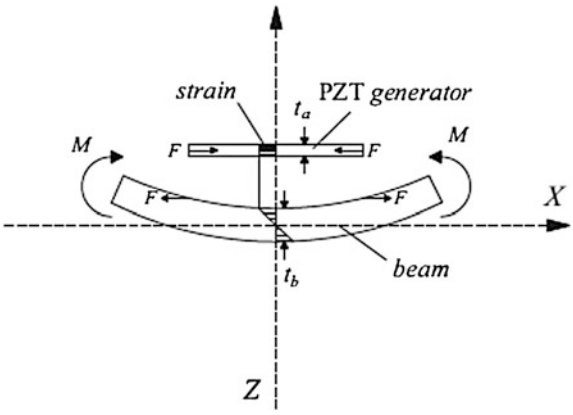

Fig. 2.56 Pin-force model of a unimorph-type piezoelectric module. Reproduced with permission from [100]. Copyright @ 2011, Elsevier

include the pin-force model, enhanced pin-force model, and Euler–Bernoulli model [100].

The pin-force model is able to estimate the output voltage of a piezoelectric harvester by considering the relationship of mechanical force between the piezoelectric material and the substrate. The piezoelectric material is attached to the substrate with a pin connection. Therefore, the shear force is intentionally designed to apply to the piezoelectric material at end of the pin connection. In this case, the shear stress exerted to the piezoelectric material is concentrated only within a small area at the end of the pin connection. The strain in the substrate is derived by Euler–Bernoulli beam theory, but the strain in the piezoelectric material is assumed to be constant. Because of this constant strain, the pin-force model does not consider the bending stiffness of the piezoelectric materials.

Figure 2.56 shows the pin-force model with a unimorph-type piezoelectric module, illustrating the strain distributions of the piezoelectric modules that consist of piezoelectric material and the substrate (PCB). When a pin-force is applied to the piezoelectric modules, an output voltage is produced, which is given by:

$$V = \frac{6g_{31}M}{bt_b(3 - Y_b t_b / Y_a t_a)}, \tag{2.50}$$

where g_{31} is piezoelectric constant, M is external moment, b is width and Y_b is Young's modulus of the piezoelectric material. Other parameters are shown in Fig. 2.56.

By considering the bending strength of the piezoelectric material, the pin-force model is modified to enhanced pin-force model. In the enhanced pin-force model, the stress and strain of piezoelectric materials are determined by the deformation shape of the substrate derived from the acting moments, as shown in Fig. 2.57. In this case, the output voltage can be estimated by:

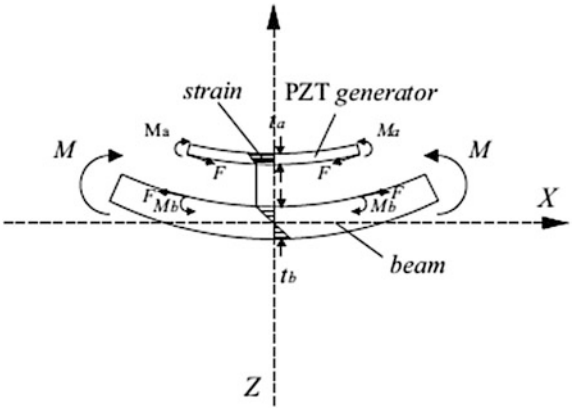

Fig. 2.57 Enhanced pin-force model of a unimorph-type piezoelectric module. Reproduced with permission from [100]. Copyright @ 2011, Elsevier

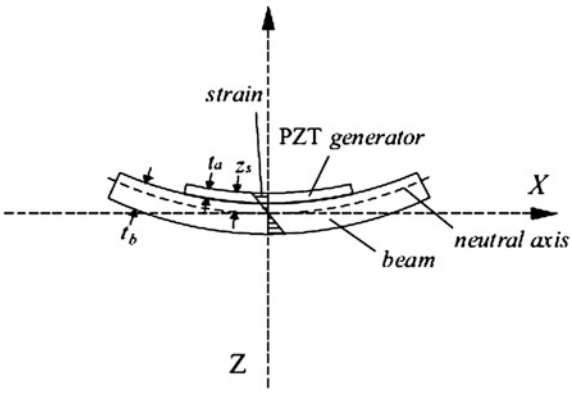

Fig. 2.58 Euler-Bernoulli model of the piezoelectric material and the substrate. Reproduced with permission from [100]. Copyright @ 2011, Elsevier

$$V = \frac{6g_{31}(t_b/t_a)M}{bt_a[3(t_b/t_a)^2 - 1 - (Y_b t_b/Y_a t_a)(t_b/t_a)^2]}, \tag{2.51}$$

Comparatively, the Euler–Bernoulli model is more accurate. This model assumes that the piezoelectric material and the substrate are deformed with the new neutral axis due to the perfectly composited piezoelectric material and the substrate, as shown in Fig. 2.58. The output voltage is given by:

$$V = \frac{6g_{31}M \cdot \frac{Y_b t_b}{Y_a t_a}\left(1 + \frac{t_b}{t_a}\right)}{bt_a\left[1 + \left(\frac{Y_b t_b}{Y_a t_a}\right)^2\left(1 + \frac{t_b}{t_a}\right)^2 + 2\frac{Y_b t_b}{Y_a t_a}\left(2 + 3\frac{t_b}{t_a} + 2\left(\frac{t_b}{t_a}\right)^2\right)\right]}. \tag{2.52}$$

The piezoelectric component is a unimorph, wording in 31 mode, with 8 mm width, 60 mm length, and 0.55 mm thickness. The unimorph is attached on a PCB with a width of 10 mm and a length of 97 mm, as shown in Fig. 2.59. The piezoelectric material is PZT ceramics prepared by using the traditional ceramic processing with a sintering temperature of 1,000 °C. After sintering, top and bottom sides of the bulk piezoelectric ceramics are coated with Ag electrode.

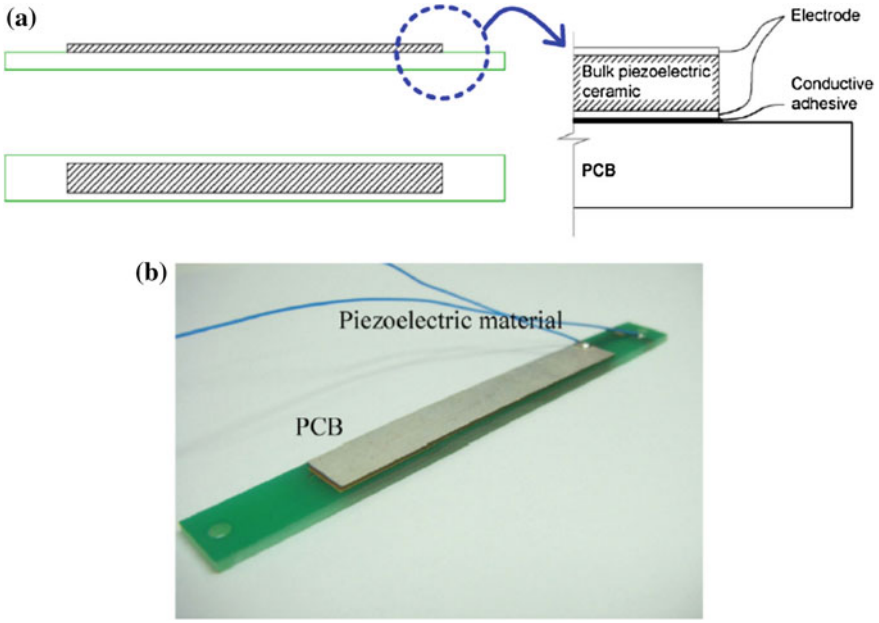

Fig. 2.59 PCB bonded piezoelectric material. **a** Detail of PCB bonded piezoelectric material. **b** Photograph of an actual PCB bonded PE material. Reproduced with permission from [100]. Copyright @ 2011, Elsevier

A steel beam-slab type bridge specimen with two steel plate girders are designed to examine the piezoelectric effect of the harvester under various loading conditions. The specimen is composed of two steel girders and a concrete slab, which is designed to have full shear connection for composite behaviors by installing shear connectors [100]. The steel girders have SS 400 grad hot rolled beams with a height of 294 mm and a width of 200 mm, while the concrete slab is 1,800 mm in width and 100 mm in thickness with a 30 MPa compressive strength. Natural frequency of the specimen is 21.0 Hz.

Ten piezoelectric modules are tested on the bridge specimen using an actuator of 250 kN capacity, with which cyclic loadings can be applied to simulate the loading conditions and effects on a real bridge. Strain gages and linear variable displacement transducers (LVDTs) are used to compare the generated piezoelectric effects with the behaviors of the structures. The output voltages of the piezoelectric modules are measured by using an oscilloscope, while the strains and displacements are measured by sing a data logger. Loading conditions include amplitude, frequency, and weight and speed of vehicles. A uniform loading test with constant velocity (PL-UV test) is conducted by changing the load amplitude from 10 to 100 kN, with constant loading frequency through the repeated process of loading and unloading. Load amplitude and the frequency variation test (PL-AP test) are carried out by varying the load amplitude and frequency. Loading frequency

variation test (PL-AV test) is to change the frequency at two load amplitudes of 20 and 40 kN. There is also a loading effect test (PL-LE test) to check the piezoelectric effect caused by the loading effects of moving vehicles [101].

It is found that the output voltage of the piezoelectric modules has a peak-to-peak value of about 13.8 V under cyclic loading of 10 kN. The output voltage shows a distorted sine wave due to the distorted phenomenon of voltage, which must be calibrated in order to use the harvested energy as electric current. Theoretically, if the applied load to the piezoelectric material is constant, the voltage output should be constant. However, in the real deformation of the piezoelectric component could not be perfectly recovered after unloading, thus resulting in the distorted waveform of the output voltage. The output voltage is found to increase as the loading frequency is increased from 0.5 to 1 Hz, and after that, saturation is observed, because the deformation of the piezoelectric component is not further increase with frequency due to the overlapping of the loading deformation.

Output voltages of the harvester have been evaluated with uniform loading that ranges from 10 to 100 kN at a constant loading velocity of 10 kN s^{-1}. The uniform loading ranging is divided into 3.0–13.0, 3.0–23.0, …, and 3.0–113.0 kN. The piezoelectric module has been attached at the lower part of the lower flange and the lower part of the concrete slab at center of the bridge specimen, where both the tensile strain and compressive strain are at the maximum level. The output voltage of the piezoelectric module at the lower part of the lower flange is $\pm$8.0 V, while that of the piezoelectric module at the lower part of the concrete slab is $\pm$2.0 V. It is found that the output voltage is slightly increased as the loading level is increased, but the increment magnitude is not proportional to the level of the loading. In addition, the output voltage is not proportional to the magnitude of strain. It also does not have a clear relation to the strain range.

Because the output voltage does not correlate with simple variation of strain, it is of interest to test the effect of loading frequency. Therefore, cyclic loadings with a sine wave with frequencies from 1.0 to 3.0 Hz are applied on the bridge specimen. Their amplitudes are varied from 10 to 50 kN. The output voltage is up to $\pm$30 V at the lower part of the lower flange in the center span, at the maximum tensile strain. The output voltage at the lower part of the concrete slab is only $\pm$2.0 V. Generally, the output voltage increases almost linearly with increasing loading level. At a given loading level, the output voltage increases with increasing frequency. This is because an increase in loading frequency means an increase in straining rate.

It is expected that the loading condition on a bridge applied by moving vehicles continuously changes. Behaviors of a bridge, such as magnitude of displacement and rate of deformation, have close relation to vehicle speed, distance between moving vehicles and location of moving vehicles on the bridge, which also have influences on the magnitude of the output voltage.

The magnitude and wave shape of the output voltage of the piezoelectric module calculated by using the Euler–Bernoulli model are quite similar to the measurement results, while there are relatively large differences between experimental results and theoretical predictions when the other two models are used.

Fig. 2.60 The bridge for the in situ study. Reproduced with permission from [101]. Copyright @ 2013, IoP Publishing

2.5.2 *In Situ Study of Bridge*

The in situ study on energy harvesting from traffic-induced vibrations involves a prestressed concrete highway bridge located on a heavily trafficked itinerary in the north of France (Fig. 2.60) [101]. It has a 33 m long simply supported span carrying three one way lanes. The structure consists of five cross braced girders. The mean flow of heavy lorries is about 8,000 per day, with large variations according to the day of the week and time in the day.

Acceleration time series are measured at a sampled frequency of 300 Hz on girders 1 and 3 of the simply supported span at three locations labeled as 1–3 in Fig. 2.61. At a high traffic intensity, the root mean square value of the measured acceleration at mid-span on girder 1, which is more heavily loaded, is as low as 0:03 m s^{-2}. Significantly higher levels of vibration are measured on a water pipe fixed on girder 1, especially at the location labeled as 0 in Figs. 2.61 and 2.62. The root mean square value of the measured acceleration for a high traffic intensity is 0.3 m s^{-2}, which is ten times the estimated value on the girder. At low traffic intensity, the root mean square value of the acceleration decreased to 0.1 m s^{-2}. These estimates outline the expected range of acceleration to be considered for this ambient source of vibration.

The acceleration signal consists of successive short-time pulses, each pulse corresponding to an individual lorry crossing the bridge. This is especially obvious in nighttime, during which the traffic intensity is so low that the inter-arrival time exceed the time to cross the bridge. The calculated average duration of the pulse is 2 s, corresponding to the time for a five axle semi-trailer vehicle to cross the span of the bridge under free flowing traffic conditions. The average acceleration peak level is 0.58 m s^{-2}. At high traffic intensity, there is some overlap among the excitations of different vehicles, resulting in a signal that is more difficult to identify. Light vehicles produce a low-level signal (ambient noise) that cannot be distinguished.

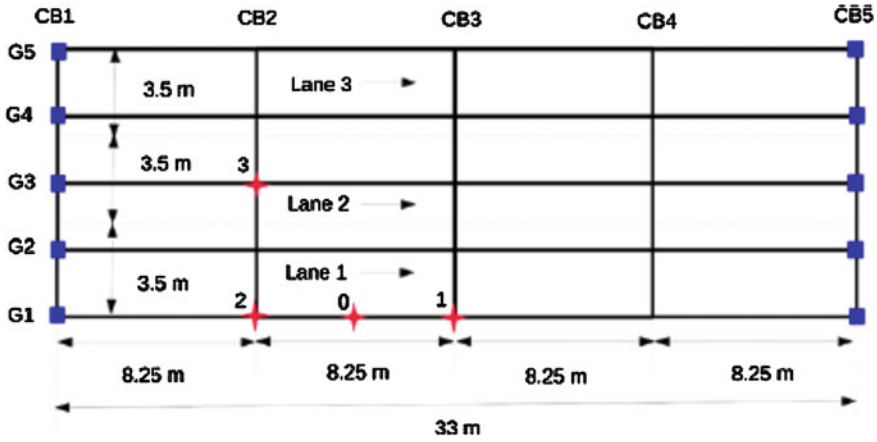

Fig. 2.61 Schematic of the bridge details. Reproduced with permission from [101]. Copyright @ 2013, IoP Publishing

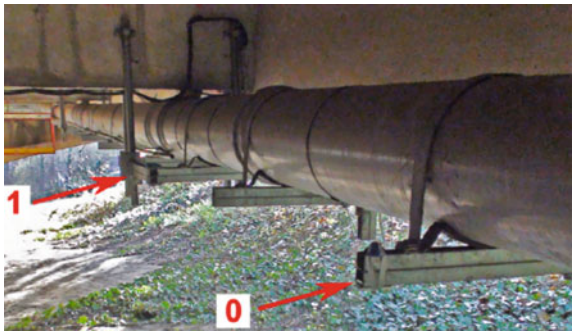

Fig. 2.62 Locations of the sensors on the pipe under the bridge. Reproduced with permission from [101]. Copyright @ 2013, IoP Publishing

To determine the frequency characteristics of the vibration sources from the bridge, it is necessary to analyze the recorded signals. Smoothed power spectra of the acceleration responses to the traffic excitation are estimated by averaging 360 power spectra of 3,000 sample blocks. Three main resonant frequencies of the bridge deck are identified in the frequency range 0–50 Hz. Two close frequencies are in the vicinity of 4 Hz and another one is at 14.5 Hz. Two close frequencies are located at 3.9 and 4.3 Hz. These resonant frequencies correspond to the longitudinal bending, torsional and transverse bending deformations of the bridge deck. The uncertainty in the frequency estimation is about 0.1 Hz and is related to fluctuations in the traffic excitation conditions. The variation in the frequency of the first bending mode induced by the change in ambient temperature with 25 °C is not more than 0.1 Hz.

In addition, the frequency characteristics are dependent on the location on the bridge. Both the mode shape of the bridge and the fixation details of the pipe have

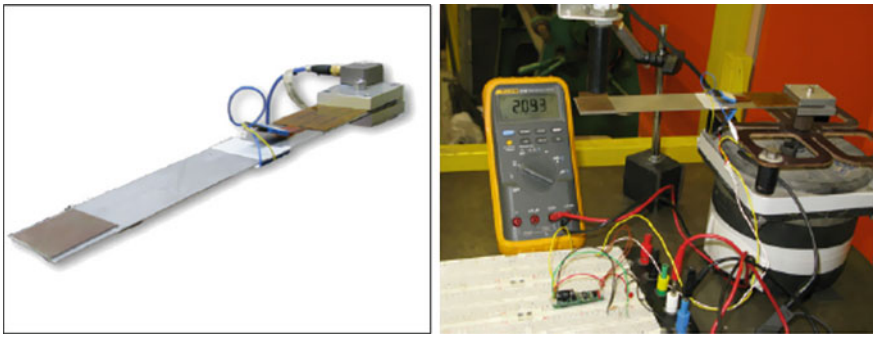

Fig. 2.63 The piezoelectric harvester designed for traffic-induced vibrations (*left*), and a view of the test set-up (*right*). Reproduced with permission from [101]. Copyright @ 2013, IoP Publishing

an influence on vibration behaviors of the pipe. The pipe usually vibrates at a resonant frequency of 14.5 Hz.

The piezoelectric energy harvesting device used in this study is a PZT cantilever, as shown in Fig. 2.63left. The resonant frequency of the harvester is tuned to be close to 14.5 Hz, thus matching the resonant vibration of the pipe discussed above. Two Mide QP20 W bimorph piezoelectric patches are bonded to the upper and lower surfaces of a 40 $\times$ 220 $\times$ 0.8 mm^3 steel plate, at the clamped end side. An additional 12 g concentrated mass is placed on the steel surface to tune the resonant frequency of the oscillator.

The experimental test setup is shown in Fig. 2.63right. An electromagnetic shaker is used to apply sinusoidal base excitations. To identify the parameters and get reference values of power conversion, tests are first carried out with a pure resistive load $R_L = 100$ kΩ connected to the output of the piezoelectric electrodes wired in series. In these tests, the RMS amplitude of the harmonic excitation is set to 0.2 m s^{-2}. The frequency of the excitation is between 14 and 15 Hz. For each frequency, the RMS voltage (V_{RMS}) across the resistor is measured. According to the power-frequency curves, the device is found to have a resonant frequency close to 14.4 Hz, at which the maximum measured power is 0.19 mW. The harvester is subsequently tested by replacing the resistive load with an ALD EH300 circuit, and further characterized by using the excitation of the bridge. Under optimized conditions, the harvester produces a power of 0.029 mW. The half-power bandwidth is about 0.8 Hz for traffic-induced excitations, which is wider than that (0.2 Hz) for harmonic excitation. Field test results indicate that an average power of 0.02 mW can be achieved. The experimental results have been in a good agreement with the theoretical predictions [101].

2.6 Energy from Natural Sources

2.6.1 Wind Energy

Wind is a promising energy source that is already used on large scales, but is less developed at smaller scales, especially by using piezoelectric harvesters. Several approaches to harvest wind energy for low power systems have been proposed. In this subsection, a device for energy harvesting from wind flows by using flexible piezoelectric films will be presented. The piezoelectric films are sandwiched between two metallic electrodes to form a capacitor structure. The generated power from multiple wind flows by using various piezofilm geometries has been theoretically calculated and experimentally characterized [102].

2.6.1.1 Power Conversion

The available power (P_{wind}) of an incident wind over a cross section unit S is given by:

$$\frac{P_{\text{wind}}}{S} = \frac{1}{2}\rho_{\text{air}} v^3, \tag{2.53}$$

where ρ_{air} is the density of air (1.225 kg m^{-3} at room temperature), assuming laminar flow, for a given wind speed v. Power transfer from wind to mechanical wave depends on wind coupling and, in particular, the alignment. At normal incidence, wind impacts the piezoelectric films, while at parallel incidence, coupling occurs due to a turbulent flow caused by the Von Karman vortexes in a bluff body, which is similar to water flows [103]. Energy harvesting efficiency is dependent on electromechanical coupling, piezofilm geometry, and external stress.

2.6.1.2 Materials and Device

PVDF piezoelectric thin films are used due to the requirement of flexibility and slow air flows. The PVDF films are sandwiched between two metallic electrodes wired to external circuits. Two wind flows are employed: one is generated by using a hairdryer and the other is generated by using a wind tunnel. The wind tunnel is used provide a laminar flow. Wind speeds are measured by using a Pitot tube. The wind from the hair dryer is turbulent. In both cases, wind speeds are kept in the range of 2–18 m s^{-1}.

Three orientations of the piezofilm with respect to wind have been studied. As shown in Fig. 2.64, (a) is parallel incidence with two cylindrical 0.5 cm diameter bluff bodies, (b) is normal incidence of the wind to the surface film, which is attached at one boundary, and (c) is normal incidence of the wind to the film, which is fixed at both sides.

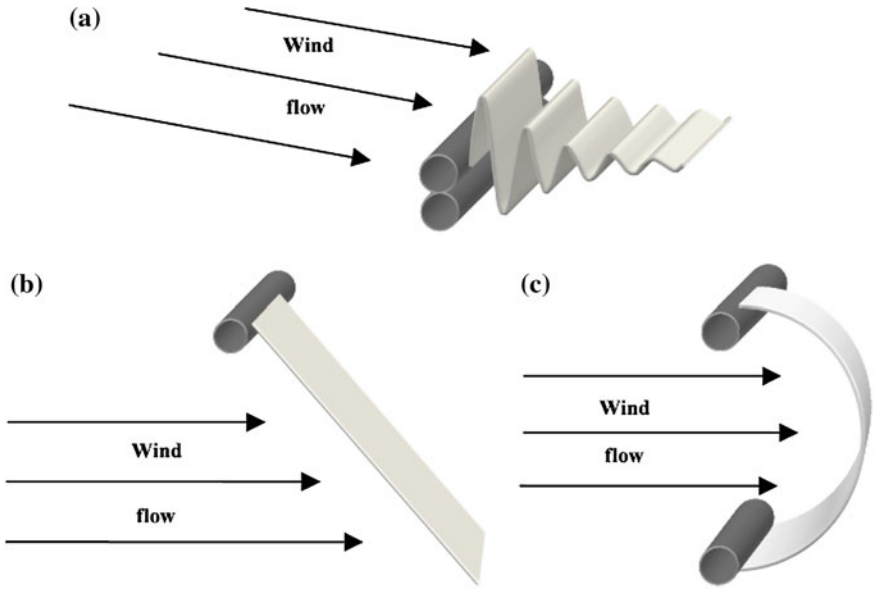

Fig. 2.64 Schematic illustration of wind incidence on the piezofilm with different oscillating behaviors. Wind incidence is parallel for setup (a) and normal for setups (b) and (c): **a** bluff body configuration, **b** one side fixed and **c** two sides fixed. Reproduced with permission from [102]. Copyright @ 2011, IoP Publishing

2.6.1.3 Characterization and Discussion

In setup (a), at low wind speed ($v < 2$ m s^{-1}), the piezofilm remains parallel to the wind flow. As the wind speed is increased to range of 2 m s$^{-1} < v < 10$ m s^{-1}, the film experiences small oscillations. Similarly, when the wind incidences perpendicularly (setup (b)), the film tends to align parallel to the flow but with small oscillations. When the film is fixed at both sides at normal wind incidence (setup (c)), oscillating waves are confined to the film. The oscillations of the three configurations seem to be similar one another. When the wind speed is further increased to $v < 15$ m s^{-1}, the oscillation amplitude of the piezofilm becomes larger, and stationary waves become chaotic movement. If the length of the film is increased, more vibrations will be observed, whereas films with smaller areas withstand stronger wind flows before becoming chaotic. Therefore, cantilever behavior is only observed at low speeds and for films with small sizes, otherwise, the films will experience traveling waves.

Theoretical relationship between wavelength and amplitude has been evaluated [102]. Wave amplitude u_0 is dependent on the configuration of the setup. For the parallel incidence (setup (a)), where stationary waves travel in a string with one end to be fixed, the piezoelectric film has a finite length, so that the relationship between the sinusoidal wave amplitude and its wavelength is given by:

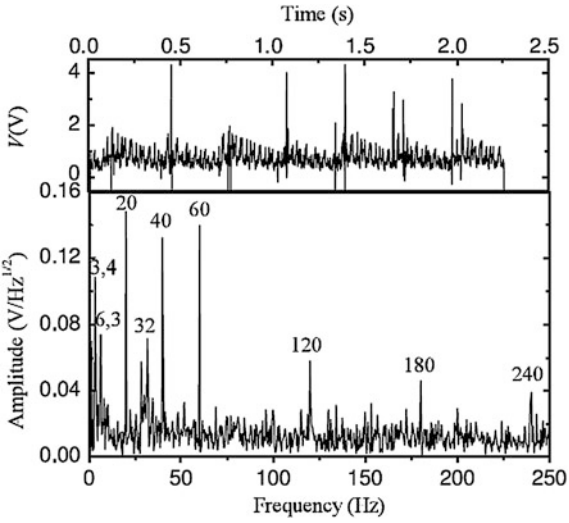

Fig. 2.65 Electrical response of a sample at 2.2 m s^{-1} in the wind tunnel excited with a bluff body. On the *top panel*, the signal is the open circuit output voltage. On the *bottom panel*, the signal is the frequency spectrum. Peaks are related to vibration modes at the indicated frequencies. Reproduced with permission from [102]. Copyright @ 2011, IoP Publishing

$$L = \int \sqrt{1 - \left(\frac{\mathrm{d}u}{\mathrm{d}x}\right)^2}\,\mathrm{d}x, \tag{2.54}$$

where, L is the total length of the film and $\mathrm{d}u/\mathrm{d}x$ is the derivative of the wave over the x-axis. This expression leads to elliptic integrals, which can be numerically solved for the films with specific lengths. The characteristics of the oscillations determine the stress applied to the piezofilms and thus charges produced by the harvester. This has been demonstrated by the frequency-dependent output voltage, as shown in Fig. 2.65, in which well-defined peaks are observed corresponding to for the various oscillating modes. The piezofilm of this device has a dimension of 1.9 cm × 15.6 cm × 40 μm.

Two parameters, speed and flow type, have been studied to characterize wind dependence energy harvesting efficiency. Experimental results are shown in Fig. 2.66. The amount of the stored energy in the capacitor increases with wind speed for a laminar flow measured in the wind tunnel. However, it does not follow the trend given by Eq. (2.53), which is mainly attributed to coupling between wind flow and the piezoelectric film, as can be seen later. The turbulent flow leads to a larger voltage than laminar flow. This is because the turbulent flow is rotational, so that it has additional contribution due to the Von Karman perturbation induced by the bluff bodies [27], which enhances the excitation effect.

It is also noticed that the energy harvesting efficiency increases with increasing thickness of the piezofilms. However, the increase in output voltage is not linear, because thickness affects mechanical damping, as discussed before. There is an optimal thickness that balances the volume of material with respect to the power increase due to the damping increase [104]. As for the effect of area of the piezofilms, only effective areas can be used for the evaluation.

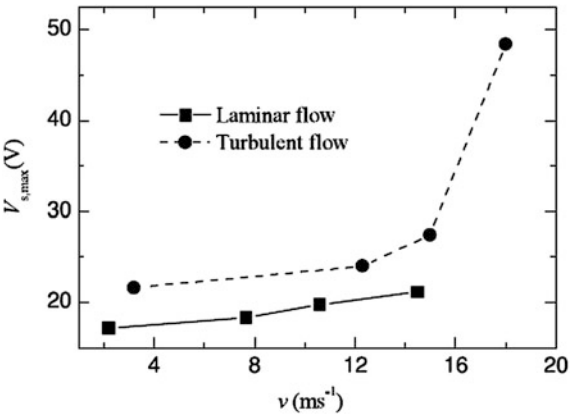

Fig. 2.66 Responses of the harvester in a bluff body configuration in the wind tunnel and by the fryer, for the piezoelectric film with a dimension of 1.2 cm × 3.0 cm × 40 μm, with a capacitor of 10 nF. Reproduced with permission from [102]. Copyright @ 2011, IoP Publishing

The power generated by the harvesters that can be delivered to capacitors with capacitance of 10 nF, 150 nF, and 1 mF have been evaluated. The current delivered by a harvester equals to the current flowing into the capacitor, which can be derived from the storage voltage as a function of time. This current is given by $I_C = C\ \mathrm{d}V_S/\mathrm{d}t$. The delivered power is thus calculated with the voltage at the storage capacitor and the current delivered to it, $P = V_S I_C$, where the losses during are neglected. The maximum available power transfer is $P_{\max} = V_{\max} I_{SC}/4$, where $V_{\max}$ is the open circuit voltage of the harvester and I_{SC} is the short circuit current. I_{SC} equals I_C when it is evaluated at the beginning ($t = 0$) when the storage capacitor voltage starts to rise. This simple evaluation has been validated by experimental results. The maximum amount of energy is produced by the harvester is 51.66 μJ, with piezofilm having an area of 7.44 cm^2 and a thickness of 64 μm, measured with a capacitor of 150 nF at a wind speed of 12.3 m s^{-1} by using a dryer in parallel configuration (setup (a)). The experimental results have a good agreement with the theoretical simulations [102].

2.6.2 Wind Energy Through Tree

Another example of using wind as an energy source is a micro-watt energy-harvester inspired by tree trunks swaying in wind [105]. A uniform flow vibrates a linear array of four cylinders affixed to piezoelectric energy transducers. Particular attention is paid to measuring the energy generated as a function of cylinder spacing, flow speed, and relative position of the cylinder within the array. Peak power is generated using cylinder center-to-center spacings of 3.3 diameters and flow speeds in which the vortex shedding frequency is 1.6 times the natural frequency of the cylinders. Using these flow speeds and spacings, the power generated by downstream cylinders can exceed that of leading cylinders by more than an order of magnitude. We visualize the flow in this system by studying the behavior of a dynamically matched flowing soap film with imbedded styrofoam disks. Our

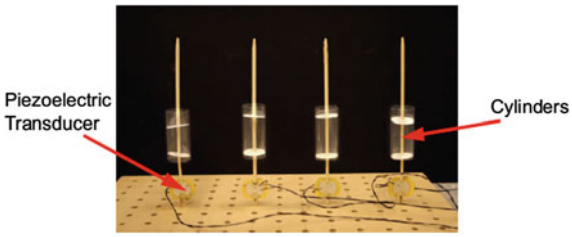

Fig. 2.67 Photograph of four piezoelectric devices arranged in series. Reproduced with permission from [105]. Copyright @ 2012, Elsevier

qualitative visualizations suggest that peak energy harvesting occurs under conditions in which vortices have fully detached from the leading cylinder.

2.6.2.1 Design and Analysis

Figure 2.67 shows a photograph of the harvester. It consists of cylinders affixed to the ground through a piezoelectric disk each. The piezoelectric disks are oriented in such a way that the cylinders can only tilt in the cross-flow direction, as demonstrated in Fig. 2.68 [105].

The cylinders in the in-line array have a geometry characterized by cylinder diameter D, height H and center-to-center distance L. Material properties of the cylinders include density ρ_c, elasticity E and dimensionless damping coefficient ζ. The fluid has density ρ_f, viscosity μ and far-field velocity U. The power generated by the harvester can be described as:

$$P = \rho_f U^3 DH \times g\left(\mathrm{Re}, \frac{L}{D}, \frac{H}{D}, \frac{f_s}{f_n}, \frac{\rho_c}{\rho_f}, \zeta\right), \tag{2.55}$$

where $\rho_f U^3 DH$ is the rate of the fluid on the cylinder and the function g depends on Reynolds number $\mathrm{Re} = UD/\nu$, dimensionless spacing L/D and cylinder height H/D, dimensionless shedding frequency f_s/f_n, mass ratio ρ_c/ρ_f and damping coefficient ζ.

The Reynolds number is in the range of $\mathrm{Re} = 4{,}000$–$9{,}000$, indicating that the viscosity effects are negligible. The cylinders are much heavier than the fluid, with a density ratio of $\rho_c/\rho_f \approx 85$. Because the amplitude of the motion of the cylinder is sufficiently small, it can be treated as two dimensional rather than three dimensional, although the motion is rotational (Fig. 2.68) [105]. The cylinders have dimensionless height of $\mathrm{H/D} = 2.2$ and dimensionless pacing of $\mathrm{L/D} = 2$–6. The height is kept at an intermediate value to increase the similarity between the piezoelectric system and the two-dimensional soap film visualizations.

The dimensionless group f_s/f_n is the ratio of vortex shedding frequency, f_s, to the natural frequency, f_n, of the elastic cylinders. In particular, resonance of the cylinder corresponds to $f_s/f_n = 1$. The natural frequency f_n of the cylinders is 11 Hz, and the cylinders under flow conditions continue to vibrate at 11–12 Hz. Because high energy generation occurs at resonance, the flow speed U should be tuned so that $f_s/f_n = 0.8$–2.0.

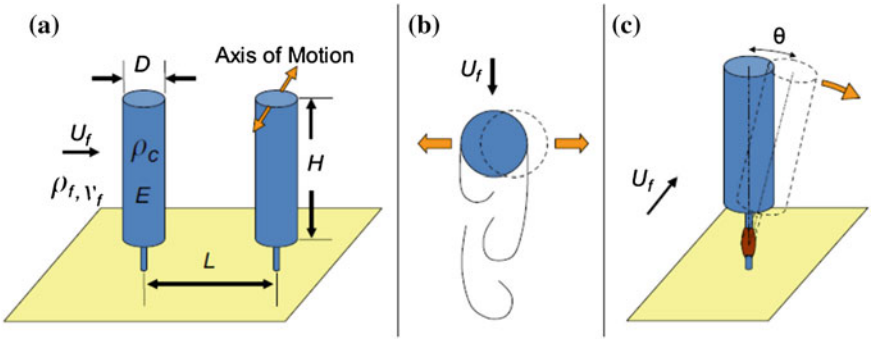

Fig. 2.68 Schematic diagrams illustrating the arrangement of the energy-harvesting cylinders. **a** *Side view* of the cylinders, along with variables characterizing the properties of the flow and the cylinder. **b–c** *Top* and *front views*. *Yellow arrows* indicate the direction of cylinder vibration, which is transverse to the incoming flow. Reproduced with permission from [105]. Copyright @ 2012, Elsevier

The resonant frequency of a circular beam in a fluid can be expressed as [106]:

$$f_n \sim \frac{D}{H^2}\left(\frac{E}{\rho_c}\right)^{1/2}\left(1+\frac{\pi\rho_f}{4\rho_c}\right)^{-1/2}. \tag{2.56}$$

Because $\rho_f \ll \rho_c$, f_s/f_n can be simplified as:

$$\frac{f_s}{f_n} \sim \frac{SU}{\sqrt{E/\rho_c}}\left(\frac{D}{H}\right)^2. \tag{2.57}$$

2.6.2.2 Fabrication and Characterization

High-speed video has been used to verify that the angular velocity of the cylinders is proportional to the output voltage. The tilting of the cylinders has been confirmed to in the cross-low direction, because the tilting in the cross-stream direction is 6°, as compared with the 1° tilting in the stream-wise direction. The output voltage of individual piezoelectric transducer is measured across a resistor of 1 MΩ, with which the output power can be calculated. The total output power of the array is given by $P_{\text{tot}} = \Sigma P_i$ (i = 1–4).

The cylinder walls are made of polyethylene storage tubes (35 mm inner in diameter, 0.4 mm in thickness and H = 78 mm in length). The tubes are attached to a bamboo rod (4.7 mm in diameter and 22 cm in length) with a pair of styrofoam spacers. A piezoelectric transducer is epoxied to the bamboo rod with a slit of 1 cm deep cut into the base of the rod. The piezoelectric transducers consist of disks for use as audio buzzers. They are composed of two ceramic layers sandwiching a 42 mm diameter brass plate between the layers. On the base of the transducer, a peg is epoxied, so as to enable the arrangement of several devices on

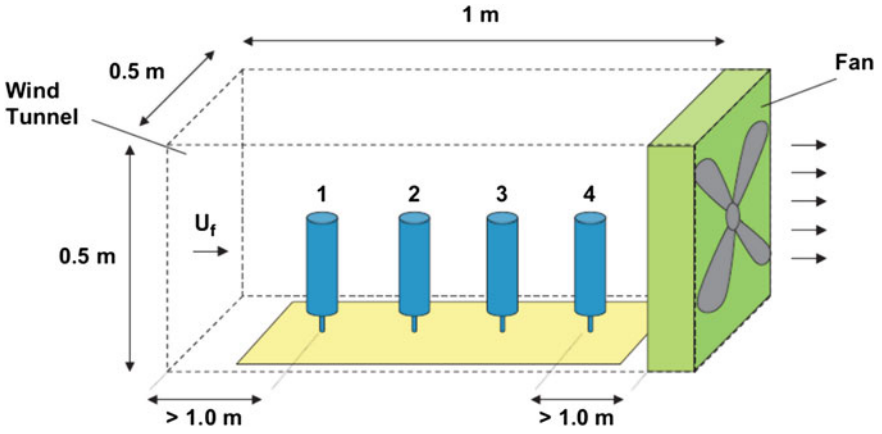

Fig. 2.69 Schematic diagram of the wind tunnel used for testing. Cylinders are numbered 1 (leading cylinder) to 4 (most downstream cylinder). Air is drawn through the tunnel, from the *left* to the *right*, by a box fan. To minimize edge effects, the first and last devices in the series are positioned at least 0.1 m from the ends of the 1 m long tunnel. Reproduced with permission from [105]. Copyright @ 2012, Elsevier

a wooden peg board, with center-to-center hole spacing of 1.5 in. The two layers of the transducer are connected in series. Wires are then run from each to a breadboard, from which voltage readings can be recorded. To tune the devices individually, such that they will resonant at 11 Hz, common metal paper clips are attached to the top of the bamboo rods, which can slid up and down the rod to change the rotational moment of inertia.

A schematic of the arrangement of four cylinders used in our tests is shown in Figs. 2.67 and 2.69. The pegboard base is designed in such a way that the arrangement of the devices can be adjusted. The cylinders are able to slide up and down the bamboo rod to adjust the mass distribution and thus the natural frequency of the devices. Figure 2.69 shows the experimental setup placed in a wind tunnel. The piezoelectric transducers and cylinders are labeled from 1 (the leading cylinder) to 4 (the most downstream cylinder). Because the devices are manually fabricated, there is a slight difference in the mechanical to electrical conversion efficiency from one device to the other. To eliminate this effect, the output power of each device has been normalized, by rotating the devices through each position, while keeping the other positions occupied, and measuring the average power output. Scaling factors of 1.26, 1.0, 1.08, and 1.30 are obtained for the devices 1–4.

Flow velocity in the wind tunnel is controlled by a combination of built-in speed controls on the fan and a 120 VAC Variac^{TM} variable transformer. The flow speed calibrated is by velocity measurements with a hand held anemometer, as so to ensure that variation in velocity is less than 5 % over the area that the piezoelectric devices are placed. The damping ratio ζ is calculated for the piezoelectric devices and the soap film system, by measuring the logarithmic decrement. Devices in each system are manually deflected and released (i.e., a step input)

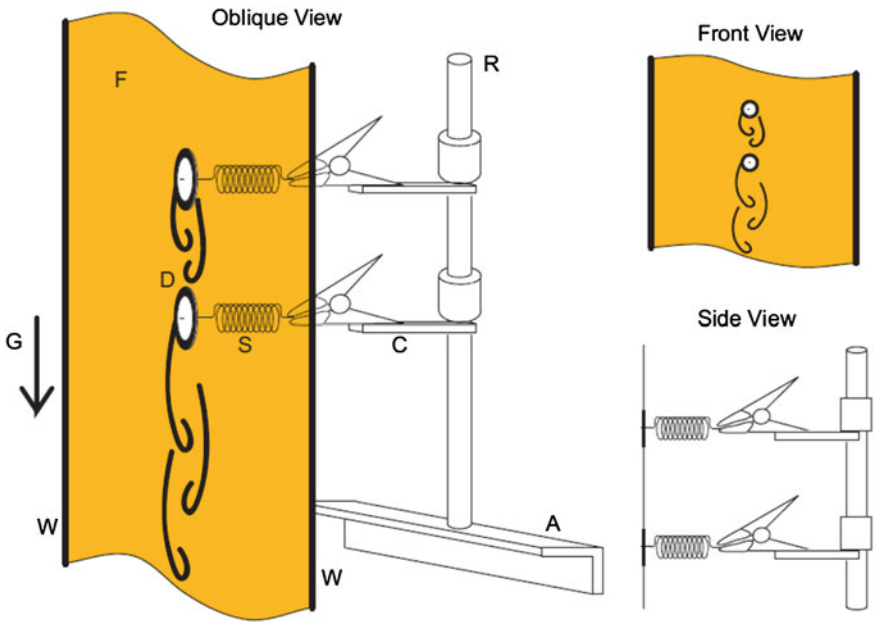

Fig. 2.70 Schematic diagram (oblique, *front* and *side* views) of the soap film apparatus. Disks (*D*) in the soap film (*F*) are suspended from linear springs (*S*) behind the film. The film flows from *top* to *bottom*, pulled by gravity (*G*). The clamps are vertically adjustable along a rod (*R*), which is fixed to an angled aluminum support (*A*). The wires (*W*) that support the film are also shown. Reproduced with permission from [105]. Copyright @ 2012, Elsevier

while the oscillating response is recorded. By measuring the decreasing motion over at least four oscillations, the damping ratio can be estimated. The springs have been verified to have a linear response in the range of flow speeds tested.

To understand the relation between vortex shedding and power output, a three-cylinder system is visualized in a dynamically matched two-dimensional flowing soap film, as shown in Fig. 2.70 [105, 107]. The styrofoam disks (diameter $D = 12.5$ mm) are suspended in the soap film with springs. The springs have a stiffness to provide dynamic similarity to the piezoelectric component. Dimensionless parameters for the wind tunnel and the soap film tests have been stated before. Two spacings, $L/D = 2$ and 5, and two flow speeds, corresponding to frequency ratios of $f_s/f_n = 0.5$ and 1.5, are used in the tests.

Systematic studies, including peak output power, relative power due to the variation in wind speed, spacing of the cylinder devices and so on, have been conducted to optimize the energy harvesting efficiency of the linear array harvesters [105]. There is an optimal wind speed for power production. Specifically, it is necessary to mention that the highest power has been found at $f_s/f_n = 1.6$, instead of $f_s/f_n = 1$, the common expectation. One of the explanations to this deviation could be related to vortex shedding frequency. The assumption that the vortex shedding frequency for the oscillating cylinders is the same as that for

stationary cylinders does not take into account the effects of frequency lock-in. In addition, the assumption that vortex shedding would only occur in the horizontal plane may not be true, because the aspect ratio of the cylinders is fairly low. This aspect deserves further study.

Future generations of our device will likely use more than four cylinders, and more work is needed to understand the limitations of adding devices. It has been found that, at intermediate wind speeds, power is maximized in third device, while at higher wind speeds, the maximum is observed in the fourth device. This means that there should be certain degree of interactions among the devices when they experience the blow of the wind. Therefore, it is important to clarify this kind of interaction before large-scale applications of this approach when more devices have to be used.

2.6.3 Water Flow

The kinetic energy due to water flow is another source of energy that can be harvested by using piezoelectric harvesters [108–110]. A new energy-harvesting device based on flow-induced vibrations has been reported, which uses PVDF flexible piezoelectric materials [108]. The second example is to PZT-5H thin film to construct the energy harvester [109], that has a similar structure to that in Ref. [108]. Another energy harvester is assembled by using macro-fiber piezoelectric composite, which is a fish-like bimorph [110]. In this subsection, the first example of piezoelectric energy harvester will be discussed in detail [108].

Figure 2.71 shows a schematic operational principle of the piezoelectric energy harvest [108]. There is a flow channel with a flexible diaphragm that is connected to a flow source. The pressure in the chamber causes the diaphragm to deflect in the upward direction. As the pressure increases to the maximum level, the diaphragm reaches its highest position. When the pressure drops, the diaphragm moves downward. As the pressure decreases to the minimum level, the diaphragm reaches its lowest position. Therefore, by connecting the energy harvester to an ambient flow source, which is capable of providing the pressure change in the pressure chamber, the energy due to the oscillating movement of the diaphragm can be harvested by using the piezoelectric film attached to it.

Figure 2.71 shows the piezoelectric energy harvester. It consists of a flow channel with two glass tubes, a polydimethylsiloxane (PDMS) diaphragm bonded to the channel and a piezoelectric PVDF film glued to the PDMS diaphragm. The device harvests the energy due to the flow-induced vibration. The flow is bounded by the flexible structure and rigid walls. If the diaphragm has small inertia and is sufficiently flexible to be able to respond rapidly to the fluctuating pressure field set up by the flow, the diaphragm can oscillate at a frequency close to that of the flow. When the fluctuating pressure is applied to the piezoelectric film, it experiences lateral strains. The normal strain causes electrical charge to accumulate on the piezoelectric electrode, resulting in a voltage in the thickness direction of the piezoelectric film.

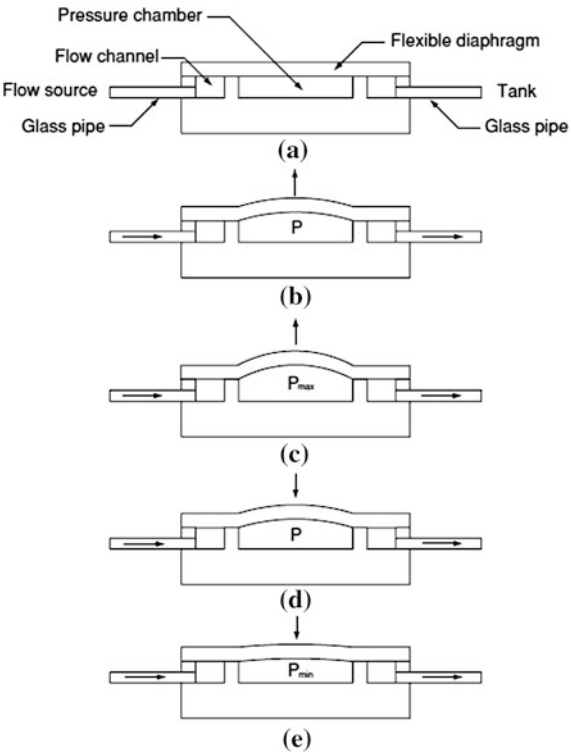

Fig. 2.71 Optional principle of the piezoelectric energy harvester due to flow caused vibration. Courtesy of Dr. D. A. Wang, National Chung Hsing University, Taiwan. Reproduced with permission from [108]. Copyright @ 2010, IoP Publishing

The piezoelectric film (LDT0-028 K/L, Measurement Specialties, Inc., USA) is a laminated film including a polyvinylidene fluoride (PVDF) film, two silver electrode layers and a polyester layer. The PDMS diaphragm has a thickness of 200 μm. The electrode layers with a thickness of 28 μm are attached to top and bottom surfaces of the PVDF film of 24 μm. A 125 μm polyester layer is laminated to top surface of the top electrode layer. When used in a bending mode, the laminated piezoelectric film develops much higher voltage output when flexed than a nonlaminated film. The neutral axis is in the polyester layer instead of in the PVDF film so the film is strained more when flexed. Because the behavior of the piezoelectric materials is assumed to be linear elastic in modelling, an almost linear increase in peak-to-peak voltage with increasing pressure difference is predicted by the theoretical simulation. For the pressure difference ranging from 1.790 to 2.392 kPa, the peak-to-peak output voltages are from 1.77 to 2.30 V.

Prototypes of the energy harvester have been fabricated for experimental evaluation. The PDMS flow channel is fabricated by a molding process with an acrylic mold. The acrylic mold is carved by a milling machine (PNC-3100, Roland DGA Co., Japan). Next, PDMS precursor material is poured over the mold to form the flow channel. The PDMS material is composed of two parts, a curing agent and the polymer. They are mixed with a volume ratio of 1:10. Before pouring into the

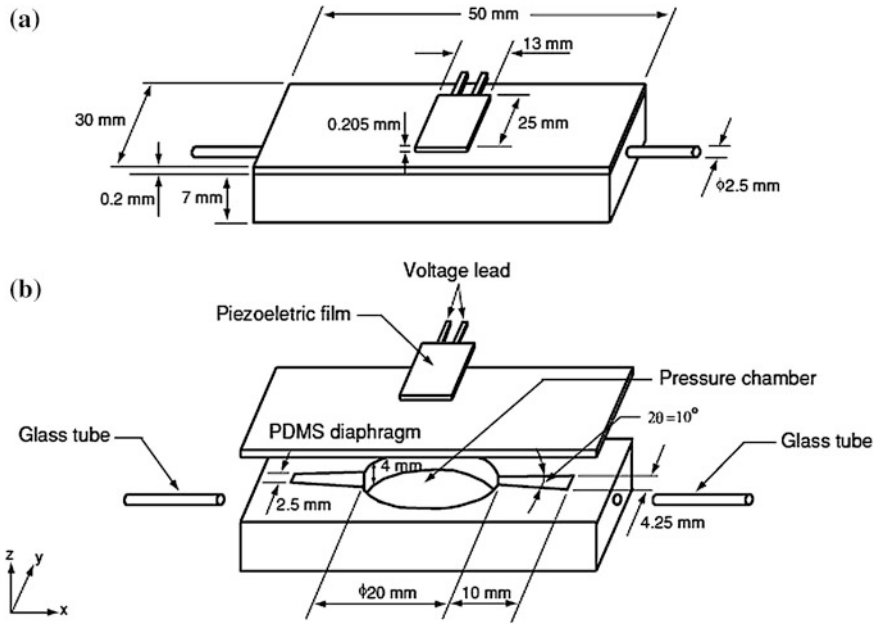

Fig. 2.72 Diagram of an assembled energy harvester (**a**) and components of the harvester (**b**). Courtesy of Dr. D. A. Wang, National Chung Hsing University, Taiwan. Reproduced with permission from [108]. Copyright @ 2010, IoP Publishing

mold, the mixture is degassed under vacuum until no bubbles appear. The PDMS is cured at 80 °C for 40 min. Then, the PDMS is peeled off from the mold (Fig. 2.72).

Figure 2.73 shows the steps to assemble the prototype of the piezoelectric energy harvester [108]. First, the inlet and outlet of the PDMS channel are prepared by piercing the front and back ends of the cured PDMS by using a copper tube with an outer diameter of 2.5 mm. After that, a PDMS diaphragm of 200 μm is glued to the flow channel with a thin layer of the liquid PDMS mixture. Two glass tubes are inserted into the inlet and outlet holes, respectively. The inlet and outlet are tightly sealed by using the PDMS mixture, after it is cured at 80 °C for 90 min. Finally, the piezoelectric film is glued to the flow channel by using an adhesive (3 M Scotch) to for the prototype. The thickness of the adhesive after the assembly step is nearly 50 μm.

Figure 2.74 shows schematic of the experimental apparatus for the characterization of the energy harvester [108]. The energy harvester is placed on the platform of a water tank. Tap water is pumped into the inlet of the energy harvester through a pulse pump to provide a periodic pressure in the pressure chamber of the energy harvester. The oscillating deflection of the piezoelectric film is monitored by using a Philtec D6 fiber optic displacement sensor. The generated voltage of the

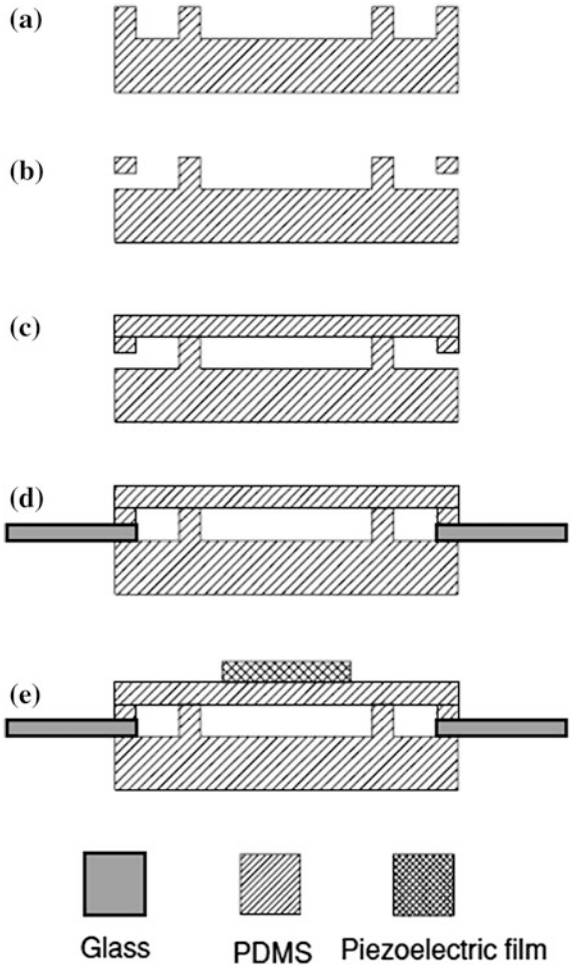

Fig. 2.73 Steps to assemble the piezoelectric energy harvester. Courtesy of Dr. D. A. Wang, National Chung Hsing University, Taiwan. Reproduced with permission from [108]. Copyright @ 2010, IoP Publishing

PVDF film is amplified and filtered by using a Stanford SR560 preamplifier, which is recorded and analyzed by using a data acquisition unit (PCI-5114, National Instruments Co., USA).

Experimental results indicate that the mean pressure and the pressure difference $P_{\max} - P_{\min}$ within the pressure chamber are 2.473 and 2.392 kPa, respectively. The measured deflection history of the center of the piezoelectric film shows that the film oscillates near a deflected position of 367 μm, with an amplitude of about 188 μm. The measured open circuit voltage generated by the PVDF film is shown in Fig. 2.75 [108]. The output peak-to-peak voltage is about 2.2 V, for an oscillation amplitude of 1.196 kPa and an excitation frequency of 26 Hz of the pressure in the pressure chamber. The experimental results do not show transient responses since they are recorded at steady state vibration. The output voltage has an almost

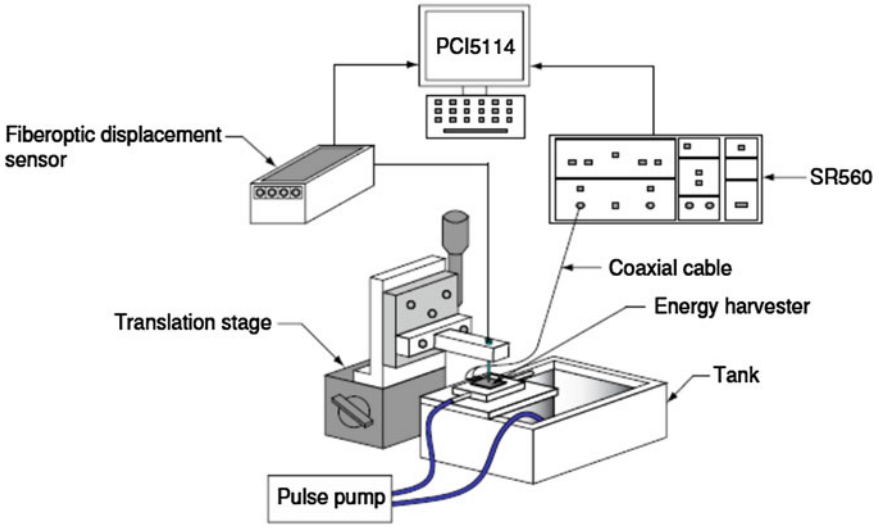

Fig. 2.74 Schematic of the experimental apparatus for the characterization of the energy harvester. Courtesy of Dr. D. A. Wang, National Chung Hsing University, Taiwan. Reproduced with permission from [108]. Copyright @ 2010, IoP Publishing

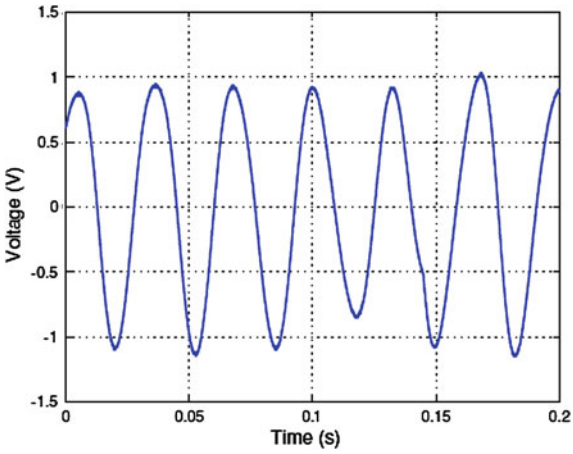

Fig. 2.75 Output voltage of the PVDF film. Courtesy of Dr. D. A. Wang, National Chung Hsing University, Taiwan. Reproduced with permission from [108]. Copyright @ 2010, IoP Publishing

linear relationship with the pressure difference and is in good agreement with the result based on the finite element model, except the point of 2.392 kPa. The slightly lower output voltage at the pressure difference of 2.392 kPa could be attributed to the aging of the PDMS. The piezoelectric energy harvester has been operated continuously for 4 h, at a rate of 93,600 cycles per hour, with an oscillation amplitude of 1.196 kPa and an excitation frequency of 26 Hz of the pressure in the pressure chamber. The device is run for a total of 152 h without failure,

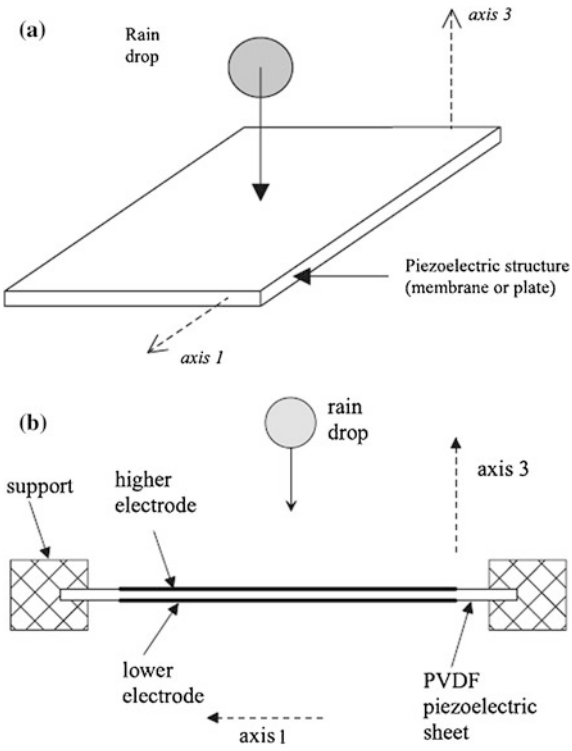

Fig. 2.76 Principle and system for raindrop energy harvesting: **a** 3D-view and **b** side-view. Reproduced with permission from [111, 112]. Copyright @ 2008, IoP Publishing

accumulating a total of 14 million cycles. The resonant frequency of the harvester is 26 Hz, which has been used to throughout the experiments.

2.6.4 Energy from Rain

Rain is liquid water in the form of droplets that have condensed from atmospheric water vapor and then precipitated, when they are heavy enough to fall under gravity. Piezoelectric effect has been proposed to collect the kinetic energy caused by rain drops. This idea has been explored theoretically, which is then validated experimentally [111, 112]. Figure 2.76 shows diagram of principle and system for energy harvesting from rain drops. In this case, PVDF should be selected as the piezoelectric component, due to the most important requirement of flexibility. Theoretical simulation results indicate that a 25 μm thick mono-stretched PVDF sheet with a piezoelectric strain coefficient $d_{31} = 2$ pJ N^{-1} is more effective than a 9 μm thick bi-stretched one with a piezoelectric coefficient of $d_{31} = 5$ pJ N^{-1} [111].

The experimental measurements conducted in various impact situations, such as different drop heights and drop sizes, have shown that the energy harvesting efficiency of the harvester is close to theoretical prediction, i.e., electrical energy of 1 nJ and instantaneous power of 1 μW collected from raindrops. If the harvester

is used to harvest energy from downpour rain drops, the energy and power could be as high as 25 μJ and 12 mW, respectively. Therefore, this is a promising approach of piezoelectric mechanical energy harvesting.

2.7 Strategies to Enhance Energy Harvesting Efficiency

2.7.1 Brief Introduction

Most piezoelectric energy harvesters discussed above are based on vibration, which generate maximum power when the resonant frequencies of the generators are matched with the frequency of the vibrational sources. A slight deviation will result in a significant decrease in power generation efficiency. The resonant frequency of a harvester is fixed after its fabrication, while the energy sources could be different from one another. Therefore, mismatching between the resonant frequency of a harvester and the vibrational frequency of an energy source is easily encountered. Various strategies have been developed to address this problem, among which two main approaches have been widely adopted: frequency tuning and bandwidth widening. While these strategies have been well documented, a brief introduction will be given in this subsection [113].

2.7.2 Frequency Tuning

The power generation of a piezoelectric harvester has been given in Eq. (2.5) [6, 113]. The maximum power is generated when the resonant frequency of the harvester matches the frequency of the vibrational source. Therefore, a given harvester is only able to harvest energy from specific sources with vibrational frequencies matching with or close to its resonant frequency. If the resonant frequency can be tuned to match with the vibrational frequencies of different sources, the application range of a harvester will be widened.

The tuning of resonant frequency of harvester can be realized by changing the mechanical characteristics of the structure of or electrical loading on the generator [113]. There are two types of tuning through changing the mechanical characteristics of a harvester: passive tuning and active tuning. Passive tuning is a periodical tuning and thus only consumes power during the tuning until the frequency matching is achieved. In contrast, active tuning is a continuous tuning even though the frequencies are already matched. Because actually both approaches have active characteristics, they are called intermittent (passive) and continuous (active) tunings. Comparatively, intermittent tuning is advantageous over the continuous tuning, because the tuning is stopped once the frequency matching is achieved, so as to minimize the system energy consumption.

Several considerations should be taken into account when evaluating a tuning approach. The energy consumption should be as low as possible and should not

exceed the energy produced by the harvester. The tunable frequency range should be sufficiently wide and the frequency resolution should meet the requirement for the give applications. The tuning should not increase the damping of the system, so as to maintain a high Q-factor for high power generation efficiency.

The resonant frequency of a generator can be tuned either mechanically or electrically. Mechanical tuning shifts the resonant frequency by changing mechanical properties of the whole structure. Electrical tuning is realized by adjusting the electrical loading.

2.7.3 Mechanical Tuning

For a cantilever with a mass at the free end, the resonant frequency is given by [113]:

$$f_r = \frac{1}{2\pi}\sqrt{\frac{Y\mathrm{wh}^3}{4l^3(m+0.24m_c)}}, \tag{2.58}$$

where similarly Y is Young's modulus of the cantilever material; w, h and l are the width, thickness and length of the cantilever, respectively, and m_c is the mass of the cantilever. Theoretically, the resonant frequency can be tuned by adjusting all these parameters. Therefore, for cantilever harvesters, mechanical tuning methods include: (i) changing dimension, (ii) shifting the center of gravity of the proof mass, (iii) varying the spring stiffness, and (iv) applying strain to the structure.

2.7.3.1 Changing Dimension

It is possible to change the length of a cantilever, while it is difficult to change its width and thickness. Furthermore, modifying length is suitable for intermittent tuning. The approach is just to change the clamping position of the cantilever, so as to adjust the effective length. Such an operation has no energy consumption. Moreover, as the resonant frequency is inversely proportional to $l^{3/2}$, a small adjustment in l can significantly change the resonant frequency f_r.

If l is the original length of the cantilever and l' is the newly adjusted length, there is $l' = l + \Delta$, where Δ is the difference between them. The mass of a cantilever is then changed to $m_c{}' = \mathrm{wh}l'\rho$, where ρ is the density of the material of the cantilever, while the original mass of a cantilever is $m_c = \mathrm{wh}l\rho$. Then the new resonant frequency becomes:

$$f_r^{'} = \frac{1}{2\pi}\sqrt{\frac{Y\mathrm{wh}^3}{4l'^3\left(m+0.24m_c^{'}\right)}} = \sqrt{\frac{Y\mathrm{wh}^3}{4(l+\Delta)^3\{m+0.24[\mathrm{wh}(l+\Delta)\rho]\}}}. \tag{2.59}$$

And the ratio of the frequency after tuning to the original frequency, which is called the normalized resonant frequency, is given by:

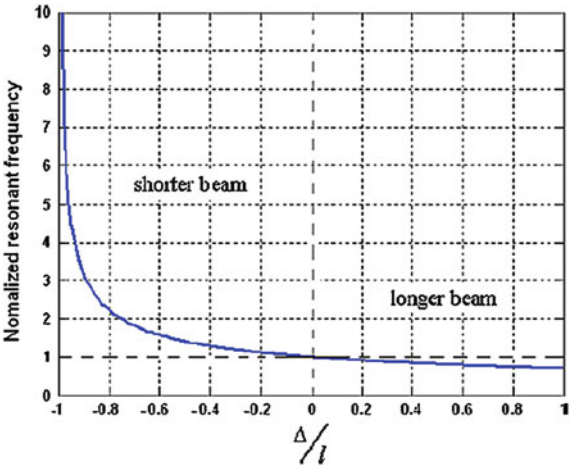

Fig. 2.77 Normalized resonant frequency as a function of the change in the length of the cantilever. Reproduced with permission from [113]. Copyright @ 2010, IoP Publishing

$$\frac{f_r^{'}}{f_r} = \sqrt{\frac{l^3(m+0.24m_c)}{l'^3\left(m+0.24m_c^{'}\right)}} = \sqrt{\frac{l^3(m+0.24\mathrm{wh}l\rho)}{(l+\Delta)^3\{m+0.24[\mathrm{wh}(l+\Delta)\rho]\}}}. \tag{2.60}$$

Figure 2.77 shows the normalized resonant frequency as a function of the change in length of the cantilever. A negative Δ/l means that the new cantilever beam is shorter than its original length and thus has a higher resonant frequency, whereas a positive Δ/l means that the cantilever beam has been lengthened, thus giving a lower resonant frequency. It is found that shortening is more efficient than lengthening to tune the resonant frequency of the cantilever.

2.7.3.2 Shifting Gravity Center of the Proof Mass

It is difficult to add or reduce the mass once a generator is fabricated. However, the gravity center of the mass can be shifted to adjust the resonant frequency of the cantilever structure. The length of the cantilever without the mass is l and the proof mass on its free end is m. The gravity center of the proof mass is located at a position, with a distance to the end of the cantilever to be x. The tuned resonant frequency of this structure can be expressed as [113, 114]:

$$f_r^{'} = \frac{1}{2\pi}\sqrt{\frac{Y\mathrm{wh}^3}{12ml^3}\cdot\frac{r^2+6r+2}{8r^4+24r^3+\frac{21}{2}r^2+4r+\frac{2}{3}}}, \tag{2.61}$$

where w and h are the width and thickness of the cantilever, respectively, and $r = x/l$. If the mass of the cantilever beam is negligible as compared with the proof mass, the resonant frequency of a cantilever-based generator, given by Eq. (2.58), can be simplified as:

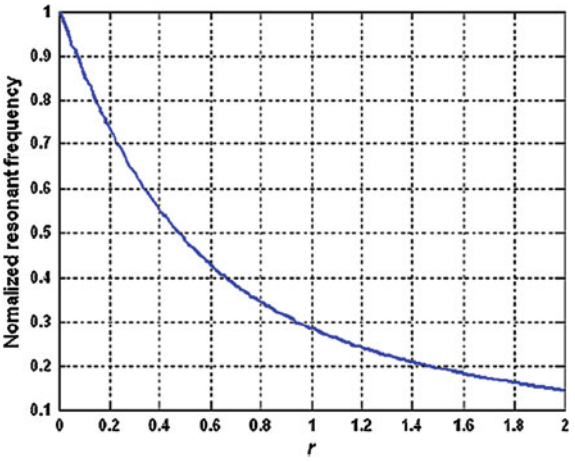

Fig. 2.78 Normalized resonant frequency as a function of the position of the gravity center of the proof mass. Reproduced with permission from [113]. Copyright @ 2010, IoP Publishing

$$f_r = \frac{1}{2\pi}\sqrt{\frac{Y\mathrm{wh}^3}{4l^3 m}}. \tag{2.62}$$

As a result, the ratio of the frequency after tuning to the original frequency is approximately given by:

$$\frac{f_r^{'}}{f_r} = \sqrt{\frac{1}{3}\cdot\frac{r^2+6r+2}{8r^4+24r^3+\frac{21}{2}r^2+4r+\frac{2}{3}}}. \tag{2.63}$$

Figure 2.78 shows the normalized resonant frequency as a function of the position of the gravity center of the proof mass. The resonant frequency almost exponentially decreases with increasing distance between the gravity center of the proof mass and the end of the cantilever.

2.7.3.3 Varying Spring Stiffness

Softening spring stiffness is an effective method that has been widely used to tune the resonant frequency of cantilever harvesters. The principle is to apply a 'negative' spring in parallel to the mechanical spring. As a result, the system has a new spring constant, effective spring constant, k_{eff}, which is given by:

$$k_{\mathrm{eff}} = k_m + k_a, \tag{2.64}$$

where k_m is the mechanical spring constant and k_a is the additional 'negative' spring stiffness. Therefore, the resonant frequency of the cantilever becomes:

$$f_r = \frac{1}{2\pi}\sqrt{\frac{k_{\mathrm{eff}}}{m}} = \sqrt{\frac{k_m + k_a}{m}}. \tag{2.65}$$

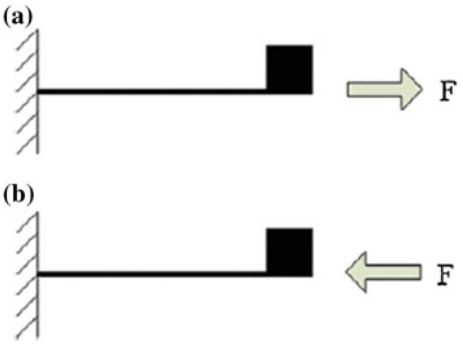

Fig. 2.79 Axial tensile (**a**) and compressive (**b**) load on a clamped-free cantilever. Reproduced with permission from [113]. Copyright @ 2010, IoP Publishing

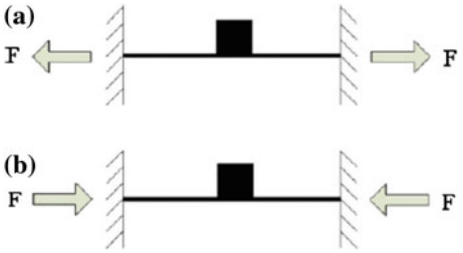

Fig. 2.80 Axial tensile (**a**) and compressive (**b**) load on a clamped–clamped cantilever. Reproduced with permission from [113]. Copyright @ 2010, IoP Publishing

The negative spring k_a can be applied electrostatically, piezoelectrically, magnetically or thermally.

2.7.3.4 Applying Straining

The effective stiffness of the structure can be varied by applying a stress to make it under certain degrees of strain. The resonant frequency of a cantilever structure can be tuned by applying an axial load. Examples of clamped-free and clamped–clamped cantilevers are shown in Figs. 2.79 and 2.80, respectively. An axial tensile load applied to the cantilevers (Figs. 2.79a and 2.80a) increases their resonant frequency, while an axial compressive load applied to the cantilevers (Figs 2.79b and 2.80b) decreases their resonant frequency.

An approximate formula for the resonant frequency of a uniform cantilever in mode i with an axial load, f_{ri}', is given by [113]:

$$f_{ri}^{'} = f_{ri} \cdot \sqrt{1 + \frac{F}{F_b} \cdot \frac{\lambda_1^2}{\lambda_i^2}}, \tag{2.66}$$

where f_r is the resonant frequency in mode i without load, F is the axial load and F_b is the axial load required to buckle the beam, i.e., to make the fundamental

resonant frequency to be zero. F is positive for a tensile load and negative for a compressive load. Variable λ_i is a dimensionless load parameter, which is a function of the beam boundary conditions applied to the cantilever for the ith mode of the beam. It is given by the ith positive solution of Eq. (2.67) for a cantilever and of Eq. (2.68) for a clamped–clamped beam:

$$\cos\lambda \cdot \cosh\lambda + 1 = 0, \tag{2.67}$$

$$\cos\lambda \cdot \cosh\lambda - 1 = 0. \tag{2.68}$$

The majority of cantilever-based piezoelectric energy harvesters work in the fundamental flexural mode (mode 1). The resonant frequency of a uniform cantilever in mode 1, with an axial load, $f_{r1}{}'$, is given by:

$$f_{r1}^{'} = f_{r1} \cdot \sqrt{1 + \frac{F}{F_b}}. \tag{2.69}$$

The ratio of the frequency after tuning to the original frequency is:

$$\frac{f_r^{'}}{f_r} = \sqrt{1 + \frac{F}{F_b}}. \tag{2.70}$$

The buckling load F_b of a cantilever and a clamped–clamped beam is given by Eqs. (2.71) and (2.72), respectively:

$$F_b = \frac{\pi^2 \cdot Y \cdot w \cdot h^3}{48 \cdot l^2}, \tag{2.71}$$

$$F_b = \frac{\pi^2 \cdot Y \cdot w \cdot h^3}{3 \cdot l^2}, \tag{2.72}$$

where Y is Young's modulus of the material of the cantilever and w, h and l are the width, thickness and length of the cantilever, respectively.

Figure 2.81 shows the resonant frequency of a cantilever as a function of the axial load [113]. It is demonstrated that a compressive load is more efficient in tuning the resonant frequency than a tensile load. If the compressive force is larger than the buckling load, the cantilever beam will buckle and no longer oscillate in mode 1. If a very large tensile force is axially applied to the cantilever, i.e., much greater than the buckling load, the resonant frequency will approach that of a straight tensioned cable as the force associated with the tension in the cantilever becomes much greater than the beam stiffness [113].

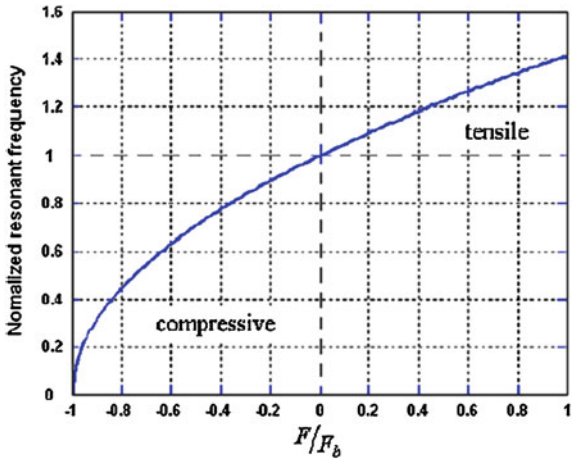

Fig. 2.81 Normalized resonant frequency as a function of the axial loads. Reproduced with permission from [113]. Copyright @ 2010, IoP Publishing

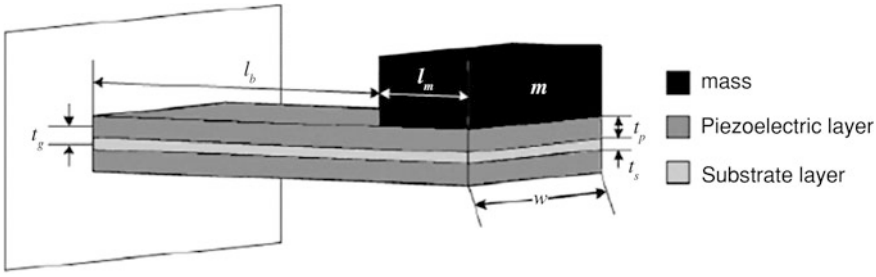

Fig. 2.82 Piezoelectric bimorph cantilever energy harvester. Reproduced with permission from [113]. Copyright @ 2010, IoP Publishing

2.7.4 Electrical Tuning

Besides mechanical methods, the resonant frequency of a cantilever can also be tuned by using electrical tuning methods. The basic principle of electrical tuning is to change the electrical damping of the cantilever by adjusting the load, so as to shift the power spectrum of the harvester. Electrical tuning is especially effective to piezoelectric harvesters. Because resistive loads usually reduce the efficiency of power transfer and it is difficult to vary the load inductances, electrical tuning is generally achieved through adjusting capacitive loads.

Figure 2.82 shows a schematic diagram of a bimorph piezoelectric generator with a mass, m, on the tip. l_b and l_m are the effective length of the cantilever and mass, respectively. w is the width of the cantilever. t_p and t_s are the thickness of the piezoelectric layer and substrate layer, respectively, and t_g is the distance from the

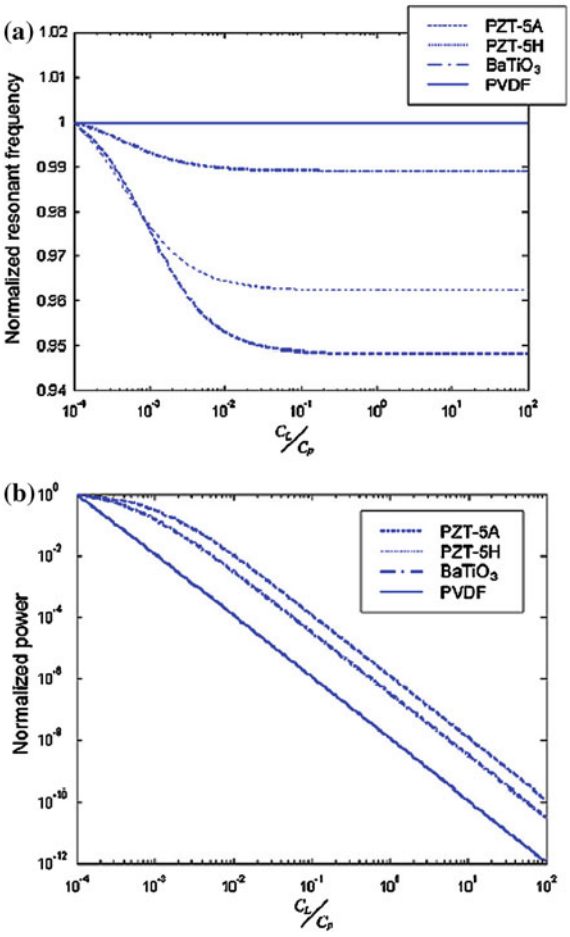

Fig. 2.83 Tuning effects on performances of the piezoelectric bimorph cantilever harvester: **a** normalized resonant frequency and **b** normalized output power. Reproduced with permission from [113]. Copyright @ 2010, IoP Publishing

center of the substrate layer to the center of the piezoelectric layer. Electrodes of the generator have been omitted in the figure. The resonant frequency of the harvester can be tuned by varying the capacitive load [113].

Figure 2.83 shows normalized resonant frequency and normalized output power of the piezoelectric harvesters, made with different piezoelectric materials, as a function of load capacitances, illustrating the effects of electrical tuning. Both the resonant frequency and the output power are decreased with increasing load capacitance. It is observed that PZT-5 H is the best among the four piezoelectric materials as an electrically tunable piezoelectric harvester.

Important aspects regarding the tunability of piezoelectric energy harvesters have been summarized [113]. The materials of the substrate layer and mass should have no effect on the tenability of the piezoelectric layer. A piezoelectric material with higher Young's modulus, strain coefficient and smaller permittivity has a

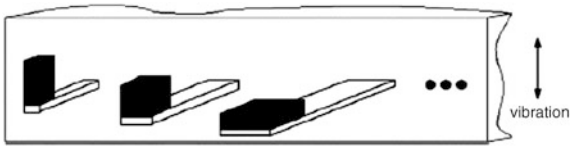

Fig. 2.84 A mechanical band-pass filter with a number of cantilever beams. Reproduced with permission from [113]. Copyright @ 2010, IoP Publishing

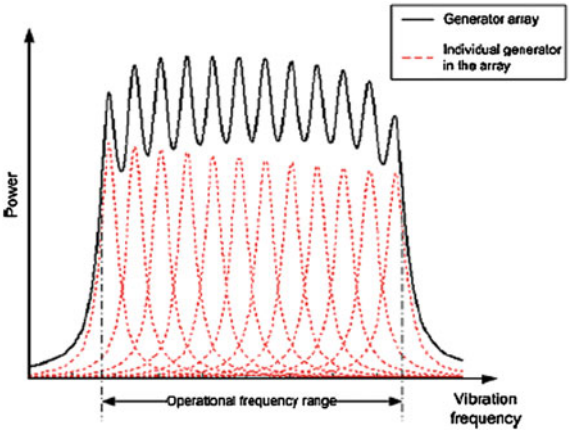

Fig. 2.85 Power spectrum of a generator array with resonant frequencies over a sufficiently wide range. Reproduced with permission from [113]. Copyright @ 2010, IoP Publishing

wider range of tunability. The ratio of the thickness of the piezoelectric layer to the thickness of the substrate layer should be small to have a wide range tuning. The capacitance of the piezoelectric layer should be minimized. If both piezoelectric layers are used for tuning, connection of these two layers in parallel will lead to a wider tuning range than connection in series. The total damping should be kept as low as possible.

2.7.5 Bandwidth Widening

The other widely adopted approach to increase the operational frequency range of a vibration energy harvester is to widen its bandwidth [113]. Various strategies have been effectively to widen the bandwidth of piezoelectric harvesters, include (i) using a harvester array consisting of numerous small generators with different resonant frequencies, (ii) introducing an amplitude limiter to the device, (iii) using coupled oscillators, (iv) employing nonlinear and bi-stable structures, and (v) designing a large generator with a large inertial mass and high degree of damping.

The effectiveness of this approach is demonstrated by the use of harvester arrays. A harvester array consists of numerous cantilever beams that are designed with different resonant frequencies. An example is shown in Fig. 2.84 [113]. Thus, the harvester has a wide operational frequency range, whereas the Q factor is not

decreased. Figure 2.85 shows the power spectrum of the generator array which is a summation of the power spectra of all the small harvesters. The frequency band of the generator is obviously widened. The problem of this approach is the complexity of fabricating the arrays and the potentially large total volume of the device.

2.8 Summary and Perspectives

Small-scale mechanical energy harvesting has been studied intensively and extensively for more than a decade, with a number of potential applications in wireless sensors and electronic devices. Large-scale harvesting at 1 W–100 kW or even higher could lead to meaningful solution to the energy crisis. It can also find important applications in self-power active or semi-active vibration controls. Relatively, more challenges have been encountered in large-scale mechanical energy harvesting technology, with many questions to be answered. Although various sources of mechanical waste energy have been identified and studied for potential energy harvesting, it is important to further explore such sources.

For practical applications, efficiency of vibrational piezoelectric energy harvesting has become a concern. Addressing this problem requires more and higher efficient transducers, understanding of motion mechanisms and sophisticated power electronic circuits. While waiting for the emergence of new piezoelectric materials with higher performances might be unrealistic at the moment, it is highly potential to develop novel physical or geometrical configurations with the materials that are currently available.

For example, the optimization of electromagnetic motor should be paid more attention. If the back electromotive force coefficient k_e is increased, the efficiency can be significantly enhanced. Motion mechanism is also a very important factor to improve the efficiency. It is understood that partial energy is lost when the kinetic energy is transformed into electric energy, such as eddy current and friction. In addition, parasitic voltage drops, the inherent resistances of the electronic components and the power consumption by the controller, are also responsible for power loss. Strategies to reduce such voltage drops and the parasitic power consumption should be further studied. Furthermore, large-scale vibrations are usually in irregular ways at time-varying frequencies and in most cases at low velocities, which all make it difficult to harvest them at acceptably high efficiencies. Therefore, it still cannot be an option for efficient power takeoff technology. In this respect, the development of novel mechanical motion rectifiers that can convert irregular oscillatory vibrations into regular unidirectional rotations is of specific significance, which should be a direction of the future research in this area.

Vibration control is another specific challenge closely associated with the efficiency of mechanical energy harvesting, especially for large-scale applications. For small-scale energy harvesting, the vibration of the host structure is not a concern. However, when a vibration energy harvesting is at a large-scale, it is

necessary to consider various issues, for instance, the protection of the mechanical systems, the human occupants and passengers during the vibration. As a result, many techniques for small-scale energy harvesting may not be applicable to the large-scale harvesting. For example, mechanic resonance can be used to magnify the vibration and thus improve the output power of the harvester in small-scale harvesting. In contrast, it becomes much difficult in large-scale applications, e.g., regenerative vehicle suspensions. Therefore, the ability of simultaneous vibration control and energy harvesting should be considered for each component and advanced control algorithms are required.

In addition, the motion mechanism should be efficient in driving and driven modes, the power electronics should be able to withdraw energy from the mechanical systems and also to inject energy into them if necessary, and the control algorithms should be able to regulate the electrical output voltages and control the regenerated electrical currents or voltages simultaneously. Because large-scale mechanical energy harvesting is not just a problem of design, it is multiple disciplinary problem and thus requires system level approaches, which involves structure dynamics and vibration, mechanical structures and design, power electronics, materials development and system controlling. Nevertheless, waste mechanical energy harvesting will be one of the most important energy technologies in the near future.

References

1. S. Roundy, R.K. Wright, J. Rabaey, A study of low level vibrations as a power source for wireless sensor nodes. Comput. Commun. **26**, 1131–1144 (2003)
2. S.P. Beeby, M.J. Tudor, N.M. White, Energy harvesting vibration sources for microsystems applications. Measur. Sci. Technol. **17**, R175–R195 (2006)
3. K.A. Cook-Chennault, N.Thambi, A.M. Sastry, Powering MEMS portable devices—a review of non-regenerative and regenerative power supply systems with emphasis on piezoelectric energy harvesting systems. Smart Mater. Struct. **17**, 043001 (2008)
4. S.R. Anton, H.A. Sodano, A review of power harvesting using piezoelectric materials (2003–2006). Smart Mater. Struct. **16**, R1–R21 (2007)
5. S. Priya, Advances in energy harvesting using low profile piezoelectric transducers. J.Electroceram. **19**, 167–184 (2007)
6. C.B. Williams, R.B. Yates, Analysis of a micro-electric generator for microsystems. Sens. Actuators A **52**, 8–11 (1996)
7. P. Glynne-Jones, M.J. Tudor, S.P. Beeby, N.M. White, An electromagnetic, vibration-powered generator for intelligent sensor systems. Sens. Actuators A **110**, 344–349 (2004)
8. D. Arnold, Review of microscale magnetic power generation. IEEE Trans. Magn. **43**, 3940–3951 (2007)
9. P. Mitcheson, P. Miao, B. Start, E. Yeatman, A. Holmes, T. Green, MEMS electrostatic micropower generator for low frequency operation. Sens. Actuators A **115**, 523–529 (2004)
10. Y.B. Jeon, R. Sood, J.H. Jeongand, S. Kim, MEMS power generator with transverse mode thin film PZT. Sens. Actuators A **122**, 16–22 (2005)
11. L. Wang, F.G. Yuan, Vibration energy harvesting by magnetostrictive material. Smart Mater. Struct. **17**, 045009 (2008)

12. W.J. Choi, Y. Jeon, J.H. Jeong, R. Sood, S.G. Kim, Energy harvesting MEMS device based on thin film piezoelectric cantilevers. J. Electroceram. **17**, 543–548 (2006)
13. G.H. Haertling, Ferroelectric ceramics: history and technology. J. Am. Ceram. Soc. **82**(4), 797–818 (1999)
14. D. Damjanovic, Ferroelectric, dielectric and piezoelectric properties of ferroelectric thin films and ceramics. Rep. Prog. Phys. **61**, 1267–1324 (1998)
15. L.B. Kong, J. Ma, H.T. Huang, W. Zhu, O.K. Tan, Lead zirconate titanate ceramics derived from oxide mixture treated by a high-energy ball milling process. Mater. Lett. **50**, 129–133 (2001)
16. L.B. Kong, T.S. Zhang, J. Ma, Y.C.F. Boey, Progress in synthesis of ferroelectric ceramic materials via high-energy mechanochemical techniques. Prog. Mater. Sci. **53**(2), 207–322 (2008)
17. L.E. Cross, R.E. Newnham, in *History of ferroelectrics*, *Ceramics and Civilization*, vol 3, ed. by W.D. Kingery. High-Technology Ceramics—Past, Present and Future (American Ceramic Society, Westerville, 1987), pp. 289–305
18. Y. Saito, H. Takao, T. Tani, T. Nonoyama, K. Takatori, T. Homma, T. Nagaya, M. Nakamura, Lead-free piezoceramics. Nature **432**, 84–87 (2004)
19. J. Rodel, W. Jo, K.T.P. Seifert, E.-M. Anton, T. Granzow, Perspective on the development of lead-free piezoceramics. J. Am. Ceram. Soc. **92**(6), 1153–1177 (2009)
20. G. Arlt, The influence of microstructure on the properties of ferroelectric ceramics. Ferroelectrics **104**, 217–227 (1990)
21. A.D. Polli, F.F. Lange, C.G. Levi, C G. Metastability of the fluorite, pyrochlore, and perovskite structures in the PbO-ZrO_2-TiO_2 system. J. Am. Ceram. Soc. **83**(4), 873–881 (2000)
22. C.A. Randall, N. Kim, J.P. Kucera, W. Cao, T.R. Shrout, Intrinsic and extrinsic size effects in fine-grained morphotropic-phase-boundary lead zirconate titanate ceramics. J. Am. Ceram. Soc. **81**(3), 677–688 (1998)
23. B. Jaffe, W.R. Cook, H. Jaffe, *Piezoelectric Ceramics* (Academic Press Limited, London, 1971)
24. I.N. Andryushinan, L.A. Reznichenko, V.A. Alyoshin, L.A. Shilkina, S.V. Titov, V.V. Titov, K.P. Andryushin, S.I. Dudkina, The PZT system ($PbZr_{1-x}Ti_xO_3$, $0.0 \leq x \leq 1.0$): specific features of recrystallization sintering and microstructures of solid solutions (part 1). Ceram. Int. **39**, 753–761 (2013)
25. B.W. Lee, Synthesis and characterization of compositionally modified PZT by wet chemical preparation from aqueous solution. J. Eur. Ceram. Soc. **24**, 925–929 (2004)
26. S.R. Shannigrahi, F.E.H. Tay, K. Yao, R.N.P. Choudhary, Effect of rare earth (La, Nd, Sm, Eu, Gd, Dy, Er and Yb) ion substitutions on the microstructural and electrical properties of sol-gel grown PZT ceramics. J. Eur. Ceram. Soc. **24**, 163–170 (2004)
27. L.B. Kong, J. Ma, T.S. Zhang, W. Zhu, O.K. Tan, $Pb(Zr_xTi_{1-x})O_3$ ceramics via reactive sintering of partially reacted mixture produced by a high-energy ball milling process. J. Mater. Res. **16**(6), 1636–1643 (2001)
28. N. Izyumskaya, Y.I. Alivov, S.J. Cho, H. Morkoc, H. Lee, Y.S. Kang, Processing, structure, properties, and applications of PZT thin films. Crit. Rev. Solid State Mater. Sci. **32**, 111–202 (2007)
29. L.B. Kong, A new solution method to deposit thick PZT films, unpublished works
30. B.M. Xu, Y.H. Ye, L.E. Cross, Dielectric properties and field-induced phase switching of lead zirconate titanate stannate antiferroelectric thick films on silicon substrates. J. Appl. Phys. **87**, 2507–2515 (2000)
31. B.M. Xu, L.E. Cross, D. Ravichandran, Synthesis of lead zirconate titanate stannate antiferroelectric thick films by sol-gel processing. J. Am. Ceram. Soc. **82**(2), 306–332 (1999)
32. B.M. Xu, Y.H. Ye, Q.M. Wang, N.G. Pai, L.E. Cross, Effect of compositional variations on electrical properties in phase switching (Pb, La)(Zr, Ti, Sn)O3 thin and thick films. J. Mater. Sci. **35**, 6027–6033 (2000)

33. Z.H. Wang, C.L. Zhao, W.G. Zhu, O.K. Tan, W. Liu, X. Yao, Processing and characterization of Pb(Zr, Ti)O3 thick films on platinum-coated silicon substrate derived from sol-gel deposition. Mater. Chem. Phys. **75**, 71–75 (2002)
34. W.G. Zhu, Z.H. Wang, C.L. Zhao, O.K. Tan, H.H. Hng, Low temperature processing of nanocrystalline lead zirconate titanate (PZT) thick films and ceramics by a modified solgel route. Jpn. J. Appl. Phys. **41**, 6969–6975 (2002)
35. Z.H. Wang, W.G. Zhu, C.L. Zhao, O.K. Tan, Dense PZT thick films derived from sol-gel based nanocomposite process. Mater. Sci. Eng., B **99**, 56–62 (2003)
36. C.L. Zhao, Z. Wang, W.G. Zhu, O.K. Tan, H.H. Hng, Microstructure and properties of PZT53/47 thick films derived from sols with submicron-sized PZT particle. Ceram. Int. **30**, 1925–1927 (2004)
37. Z.H. Wang, W.G. Zhu, C.L. Chao, X.F. Chen, Characterization of composite piezoelectric thick film for MEMS application. Surf. Coat. Technol. **198**, 384–388 (2005)
38. R.G. Kepler, R.A. Anderson, Ferroelectric polymers. Adv. Phys. **41**(1), 1–57 (1992)
39. V.V. Kochervinskii, Piezoelectricity in crystallizing ferroelectric polymers: poly(vinylidene fluoride) and its copolymers (a review). Crystallogr. Rep. **48**(4), 649–675 (2003)
40. T. Furukawa, Piezoelectricity and pyroelectricity in polymers. IEEE Trans. Electr. Insul. **24**, 375–394 (1989)
41. J.F. Tressler, S. Alkoy, A. Dogan, R.E. Newnham, Functional composites for sensors, actuators and transducers. Compos. Part A **30**, 477–482 (1999)
42. B. Hilczer, J. Kulek, E. Markiewicz, M. Kosec, B. Malic, Dielectric relaxation in ferroelectric PZT-PVDF nanocomposites. J. Non-Cryst. Solids **305**, 167–173 (2002)
43. K.A. Cook-Chennault, N. Thambi, A.M. Sastry, Powering MEMS portable devices-a review of non-regenerative and regenerative power supply systems with special emphasis on piezoelectric energy, harvesting systems. Smart Mater. Struct. **17**, 043001 (2008)
44. S.P. Beeby, M.J. Tudor, N.M. White, Energy harvesting vibration sources for microsystems applications. Meas. Sci. Technol. **17**, R175–R195 (2006)
45. Standards Committee of the IEEE Ultrasonics Ferroelectrics, and Frequency Control Society, *IEEE Standard on Piezoelectricity* (IEEE, New York, 1987)
46. A. Erturk, D.J. Inman, *Piezoelectric Energy Harvesting*, 1st edn. (Wiley, Chichester, 2011)
47. D. Zhu, in Vibration Energy Harvesting: Machinery Vibration, Human Movement and Flow Induced Vibration, Chapter 2, ed. by Y. K. Tan. *Sustainable Energy Harvesting Technologies—Past*, *Present and Future* (Intech, Rijeka, 2011)
48. H.A. Sodano, G. Park, D.J. Inman, Estimation of electric charge output for piezoelectric energy harvesting. Strain **40**, 49–58 (2004)
49. S.N. Chen, G.J. Wang, M.C. Chien, Analytical modeling of piezoelectric vibration-induced micro power generator. Mechatronics **16**, 387–397 (2006)
50. J. Ajitsaria, S.Y. Choe, D. Shen, D.J. Kim, Modeling and analysis of a bimorph piezoelectric cantilever beam for voltage generation. Smart Mater. Struct. **16**, 447–454 (2007)
51. G.K. Ottman, H.F. Hofmann, G.A. Lesieutre, Optimized piezoelectric energy harvesting circuit using step-down converter in discontinuous conduction mode. IEEE Trans. Power Electron. **18**, 696–703 (2003)
52. D. Guyomar, A. Badel, E. Lefeuvre, C. Richard, Toward energy harvesting using active materials and conversion improvement by nonlinear processing. IEEE Trans. Ultrason. Ferroelect. Freq. Control **52**, 584–595 (2005)
53. N. Kong, D.S. Ha, A. Erturk, D.J. Inman, Resistive impedance matching circuit for piezoelectric energy harvesting. J. Intell. Mater. Syst. Struct. **21**, 1293–1302 (2010)
54. S. Roundy, P.K. Wright, A piezoelectric vibration based generator for wireless electronics. Smart Mater. Struct. **13**, 1131–1144 (2004)
55. N.E. DuToit, B.L. Wardle, S. Kim, Design considerations for MEMS-scale piezoelectric mechanical vibration energy harvesters. Integr. Ferroelectr. **71**, 121–160 (2005)
56. L. Meirovitch, *Fundamentals of Vibrations* (McGraw-Hill, New York, 2001)
57. D.J. Inman, *Engineering Vibration* (Prentice Hall, Englewood Cliffs, 2007)

58. N.G. Stephen, On energy harvesting from ambient vibration. J. Sound Vib. **293**, 409–425 (2006)
59. A. Erturk, D.J. Inman, On mechanical modeling of cantilevered piezoelectric vibration energy harvesters. J. Intell. Mater. Syst. Struct. **19**, 1311–1325 (2008)
60. H.A. Sodano, G. Park, D.J. Inman, Estimation of electric charge output for piezoelectric energy harvesting. Strain **40**, 49–58 (2004)
61. N.E. duToit, B.L. Wardle, Experimental verification of models for microfabricated piezoelectric vibration energy harvesters. AIAA J. **45**, 1126–1137 (2007)
62. F. Lu, H.P. Lee, S.P. Lim, Modeling and analysis of micro piezoelectric power generators for micro-electromechanical-systems applications. Smart Mater. Struct. **13**, 57–63 (2004)
63. S.N. Chen, G.J. Wang, M.C. Chien, Analytical modeling of piezoelectric vibration-induced micro power generator. Mechatronics **16**, 387–397 (2006)
64. J.H. Lin, X.M. Wu, T.L. Ren, L.T. Liu, Modeling and simulation of piezoelectric MEMS energy harvesting device. Integr. Ferroelectr. **95**, 128–141 (2007)
65. A. Erturk, D.J. Inman, Issues in mathematical modeling of piezoelectric energy harvesters. Smart Mater. Struct. **17**, 065016 (2008)
66. A. Erturk, D.J. Inman, A distributed parameter electromechanical model for cantilevered piezoelectric energy harvesters. ASME J. Vib. Acoust. **130**, 041002 (2008)
67. A. Erturk, D.J. Inman, An experimentally validated bimorph cantilever model for piezoelectric energy harvesting from base excitations. Smart Mater. Struct. **18**, 025009 (2009)
68. C.J. Rupp, A. Evgrafov, K. Maute, M.L. Dunn, Design of piezoelectric energy harvesting systems: a topology optimization approach based on multilayer plates and shells. J. Intell. Mater. Syst. Struct. **20**, 1923–1939 (2009)
69. C. Jr De Marqui, A. Erturk, D.J. Inman, An electromechanical finite element model for piezoelectric energy harvester plates. J. Sound Vib. **327**, 9–25 (2009)
70. N.G. Elvin, A.A. Elvin, A coupled finite element—circuit simulation model for analyzing piezoelectric energy generators. J. Intell. Mater. Syst. Struct. **20**, 587–595 (2009)
71. Y. Yang, T. Tang, Equivalent circuit modeling of piezoelectric energy harvesters. J. Intell. Mater. Syst. Struct. **20**, 2223–2235 (2009)
72. A. Erturk, J. Hoffmann, D.J. Inman, A piezomagnetoelastic structure for broadband vibration energy harvesting. Appl. Phys. Lett. **94**, 254102 (2009)
73. S.C. Stanton, C.C. McGehee, B.P. Mann, Reversible hysteresis for broadband magnetopiezoelastic energy harvesting. Appl. Phys. Lett. **96**, 174103 (2009)
74. S.C. Stanton, C.C. McGehee, B.P. Mann, Nonlinear dynamics for broadband energy harvesting: investigation of a bistable inertial generator. Physica D **239**, 640–653 (2010)
75. S. Adhikari, M.I. Friswell, D.J. Inman, Piezoelectric energy harvesting from broadband random vibrations. Smart Mater. Struct. **18**, 115005 (2009)
76. N.S. Shenck, J.A. Paradiso, Energy scavenging with shoe-mounted piezoelectrics. IEEE Micro **21**, 30–42 (2001)
77. D. Fourie, Shoe-mounted PVDF piezoelectric transducer for energy harvesting (online version). http://web.vtc.edu/courses/el/elt2720/studentwork2012/KatieCloutier/index_files/shoe_mounted_piezo.pdf
78. J.G. Rocha, L.M. Goncalves, P.F. Rocha, M.P. Silva, S. Lanceros-Mendez, Energy harvesting from piezoelectric materials fully integrated in footwear. IEEE Trans Industr. Electron. **57**, 813–820 (2010)
79. L. Moro, D. Benasciutti, Harvested power and sensitivity analysis of vibrating shoe-mounted piezoelectric cantilevers. Smart Mater. Struct. **19**, 115011 (2010)
80. D. Benasciutti, L. Moro, Energy Harvesting with Vibrating Shoe-Mounted Piezoelectric Cantilevers (Chapter 6), in *Advances in Energy Harvesting Methods*, ed. by N. Elvin, A. Erturk (Springer Science+Business Media, New York, 2013)
81. W.R. Ledoux, H.J. Hillstrom, Acceleration of the calcaneus at heel strike in neutrally aligned and pes planus feet. Clin. Biomech. **16**, 608–613 (2001)

82. L. Mateu, F. Moll, Appropriate charge control of the storage capacitor in a piezoelectric energy harvesting device for discontinuous load operation. Sens. Actuators A **132**, 302–310 (2006)
83. W.M. Whittle, *Gait analysis, An Introduction*, 4th edn. (Elsevier, Philadelphia, 2007)
84. J. Perry, *Gait Analysis: Normal and Pathological Function* (SLACK Incorporated, Thorofare, 1992)
85. D.A. Winter, Foot trajectory in human gait: a precise and multifactorial motor control task. Phys. Ther. **72**, 45–53 (1992)
86. V.L. Giddings, G.S. Beaupre, R.T. Whalen, D.R. Carter, Calcaneal loading during walking and running. Med. Sci. Sports Exerc. **32**, 627–634 (2000)
87. B.K. Tripathy, A study on step distance and its relation with some morphometric features in adult male. Anthropologist **6**, 137–139 (2004)
88. P. Pillatsch, E.M. Yeatman, A.S. Holmes, A scalable piezoelectric impulse-excited energy harvester for human body excitation. Smart Mater. Struct. **21**, 115018 (2012)
89. M. Renaud, P. Fiorini, R. van Schaijkand, C. Van Hoof, Harvesting energy from the motion of human limbs: the design and analysis of an impact-based piezoelectric generator. Smart Mater. Struct. **18**, 035001 (2009)
90. S. Wei, H. Hu, S. He, Modeling and experimental investigation of an impact-driven piezoelectric energy harvester from human motion. Smart Mater. Struct. **22**, 105020 (2013)
91. M. Pozzi, M. Zhu, Plucked piezoelectric bimorphs for knee-joint energy harvesting: modeling and experimental validation. Smart Mater. Struct. **20**, 055007 (2011)
92. M. Pozzi, M. Zhu, Characterization of a rotary piezoelectric energy harvester based on plucking excitation for knee-joint wearable applications. Smart Mater. Struct. **21**, 055004 (2012)
93. M. Pozzi1, M.S.H. Aung, M. Zhu, R.K Jones, J.Y Goulermas, The pizzicato knee-joint energy harvester: characterization with biomechanical data and the effect of backpack load. Smart Mater. Struct. **21**, 075023 (2012)
94. B. Yang, K.S. Yun, Piezoelectric shell structures as wearable energy harvesters for effective power generation at low-frequency movement. Sens. Actuators. A **188**, 427–433 (2012)
95. E. Kebadze, S.D. Guest, S. Pellegrino, Bistable prestressed shell structures. Int. J. Solids Struct. **41**(2004), 2801–2820 (2004)
96. S.J. Kim, J.S. Hwang, J. Mok, Sensor/actuator optimal design for active vibration control of shell structure. J. Intell. Mater. Syst. Struct. **11**, 848–856 (2000)
97. S. Daynes, K.D. Potter, P.M. Weaver, Bistable prestressed buckled laminates. Compos. Sci. Technol. **68**, 3431–3437 (2008)
98. L. Gu, C. Livermore, Compact passively self-tuning energy harvesting for rotating applications. Smart Mater. Struct. **21**, 015002 (2012)
99. M. Umeda, K. Nakamura, S. Ueha, Analysis of transformation of mechanical impact energy to electrical energy using a piezoelectric vibrator. Jpn. J. Appl. Phys. **35**, 3267–3273 (1996)
100. S.H. Kim, J.H. Ahn, H.M. Chung, H.W. Kang, Analysis of piezoelectric effects on various loading conditions for energy harvesting in a bridge system. Sens. Actuators. A **167**, 468–483 (2011)
101. M. Peigney, D. Siegert, Piezoelectric energy harvesting from traffic-induced bridge vibrations. Smart Mater. Struct. **22**, 095019 (2013)
102. V.J. Ovejas, A. Cuadras, Multimodal piezoelectric wind energy harvesters. Smart Mater. Struct. **20**, 085030 (2011)
103. J.J. Allen, A.J. Smits, Energy harvesting eel. J. Fluids Struct. **15**, 629–640 (2001)
104. P. Rakbamrung, M. Lallart, D. Guyomar, N. Muensit, C. Thanachayanont, C. Lucat, B. Guiffard, L. Petit, P. Sukwisut, Performance comparison of PZT and PMN-PT piezoceramics for vibration energy harvesting using standard or nonlinear approach. Sens. Actuators A **163**, 493–500 (2011)
105. W.B. Hobbs, D.L. Hu, Tree-inspired piezoelectric energy harvesting. J. Fluids Struct. **28**, 103–114 (2012)

106. C. Van Eysden, J. Sader, Resonant frequencies of a rectangular cantilever beam immersed in a fluid. J. Appl. Phys. **100**, 114916 (2009)
107. L. Ristroph, J. Zhang, Anomalous hydrodynamic drafting of interacting flapping flags. Phys. Rev. Lett. **101**, 194502 (2008)
108. D.A. Wang, H.H. Ko, Piezoelectric energy harvesting from flow-induced vibration. J. Micromech. Microeng. **20**, 025019 (2010)
109. D.A. Wang, N.Z. Liu, A shear mode piezoelectric energy harvester based on a pressurized water flow. Sens. Actuators A **167**, 449–458 (2011)
110. A. Erturk, G. Delporte, Underwater thrust and power generation using flexible piezoelectric composites: an experimental investigation toward self-powered swimmer-sensor platforms. Smart Mater. Struct. **20**, 125013 (2011)
111. R. Guigon, J.J. Chaillout, T. Jager, G. Despesse, Harvesting raindrop energy: theory. Smart Mater. Struct. **17**, 015038 (2008)
112. R. Guigon, J.J. Chaillout, T. Jager, G. Despesse, Harvesting raindrop energy: experimental study. Smart Mater. Struct. **17**, 015039 (2008)
113. D. Zhu, M.J. Tudor, S.P. Beeby, Strategies for increasing the operating frequency range of vibration energy harvesters: a review. Meas. Sci. Technol. **21**, 022002 (2010)
114. L. Roylance, J.B. Angell, A batch fabricated silicon accelerometer. IEEE Trans. Electron Devices **26**, 1911–1917 (1979)

http://www.springer.com/978-3-642-54633-4

Waste Energy Harvesting
Mechanical and Thermal Energies
Kong, L.B.; Li, T.; Hng, H.H.; Boey, F.; Zhang, T.; Li, S.
2014, XII, 592 p. 331 illus., 64 illus. in color., Hardcover
ISBN: 978-3-642-54633-4